INVESTIGATING DENDRITIC GROWTH IN SYMMETRICAL LITHIUM CELLS THROUGH MRI AND SIMULATION

Rok Peklar

Doctorate Thesis
Jožef Stefan International Postgraduate School
Ljubljana, Slovenia

Supervisor: Prof. Dr. Igor Serša, Jožef Stefan Institute, Ljubljana, Slovenia

Evaluation Board:
Prof. Dr. Tomaž Apih, Chair, Jožef Stefan International Postgraduate School and Jožef Stefan Institute, Ljubljana, Slovenia
Prof. Dr. Boštjan Zalar, Member, Jožef Stefan International Postgraduate School and Jožef Stefan Institute, Ljubljana, Slovenia
Prof. Dr. Siegfried Stapf, Member, Technical University of Ilmenau, Ilmenau, Germany

MEDNARODNA PODIPLOMSKA ŠOLA JOŽEFA STEFANA
JOŽEF STEFAN INTERNATIONAL POSTGRADUATE SCHOOL



Rok Peklar

INVESTIGATING DENDRITIC GROWTH IN SYMMETRICAL LITHIUM CELLS THROUGH MRI AND SIMULATION

Doctorate Thesis

RAZISKOVANJE RASTI DENDRITOV V SIMETRIČNIH LITIJEVIH CELICAH Z UPORABO MRI IN SIMULACIJ

Doktorsko delo

Supervisor: Prof. Dr. Igor Serša

Ljubljana, Slovenia, September 2025

To my dear Eva, my family, and friends – thank you for everything.

Acknowledgments

My warmest thanks go to Igor Serša and Urša Mikac, for their guidance, encouragement, and for granting me the freedom to explore this project in my way. I am deeply grateful for their patience and understanding during the more challenging periods of this journey and for introducing me to the spirit and practice of scientific research.

Sincere thanks also go to our technician, Ana Sepe, whose reliability ensured that I could always rely on the equipment functioning as needed.

Many thanks to the colleagues I now consider friends. Coffee breaks and foosball sessions in your company made coming to work a daily joy.

I am grateful to the Jožef Stefan Institute and the Jožef Stefan International Postgraduate School, as well as to all the supporting staff who helped make both the research and study processes run smoothly.

I also acknowledge the Slovenian research agency for providing funding for this work.

Heartfelt thanks to my friends for providing perspective, good humour and much-needed distractions at just the right moments.

I am forever grateful to my family for their love, encouragement, and support. This journey began long before my doctoral studies, and I am deeply grateful to have had the means and opportunity to pursue it.

Above all, I am most grateful to my dear Eva; for your love, support, and understanding. Your companionship means more than words can express.

Abstract

Lithium metal batteries (LMBs) represent a highly promising technology for the future generation of energy storage, due to their very high theoretical energy density. However, their implementation is hindered by the growth of dendrites; needle-like structures, that pose a safety concern and degrade the performance and lifespan of the battery. This thesis covers the fundamentals of dendrite growth and explores new dendrite prevention strategies by merging experimental methods with computational modelling.

The main goal of this thesis was to study the dendrite growth process and to find potential mitigation approaches. This was attempted by combining magnetic resonance imaging (MRI) and diffusion-limited aggregation algorithm (DLA) based computational modelling. MRI is a technique for non-invasive operando imaging of the electrodeposition process, while the DLA-based model is suitable for capturing the random nature of the dendrite growth process.

MRI provided a way to noninvasively monitor the electrodeposition/dendrite growth in symmetric lithium-electrolyte-lithium cells. The acquired images showed complex structures with different morphologies, depending on the operating conditions of the cell. Comparative experiments on simple, parallel and series electrode topologies showed that parallel promote runaway filament growth, whereas series configuration imposes uniform planar deposition. Additionally, electrolyte-depletion fronts and the accumulation of passivated "dead" lithium was monitored. MRI enabled not only the imaging of dendrites (via signal voids), but also gas formation and formation of "dead lithium", which, when combined, provides a comprehensive view of the nucleation and growth process of lithium dendrites.

To complement MRI observations, a field-biased 3D diffusion-limited aggregation (DLA) algorithm, coupled with a Laplace solver for the electric potential, reproduced deposition patterns and showed that ohmic drop is the primary selector of deposition sites. A two-dimensional multibody DLA (MBDLA) model extended the analysis to include the electrolyte ion concentration and interfacial kinetics, generating a morphological phase diagram that maps transitions from sparse fractals to dense deposits.

This research aligns well with the current electrochemomechanical knowledge on electrodeposition; dendrite morphology is governed by a complex interaction of electrolyte concentration gradients, local current-density heterogeneities as well as multitude of chemical and mechanical interfacial phenomena. Based on the insights of our studies, the thesis proposes mitigation approaches that focus on current distribution homogenization, high concentration, high diffusion electrolytes and engineered interphases that regulate interfacial kinetics.

The developed methodologies, presented in this work, offer robust tools for predicting dendritic behaviours and designing safer and more efficient LMBs. Future research directions include expanding the use of MRI as a non-destructive analysis method for battery research, as well as ion-transport based dendrite mitigation methods.

Povzetek

Litij-kovinske baterije (LMB) predstavljajo izjemno obetavno tehnologijo prihodnje generacije shranjevanja energije, saj dosegajo izjemno visoko teoretično energijsko gostoto. Njihovo praktično uporabo pa omejuje rast dendritov; igličastih struktur, ki ogrožajo varnost ter zmanjšujejo zmogljivost in življenjsko dobo baterije. Ta disertacija obravnava temeljne mehanizme nastanka dendritov ter raziskuje nove strategije njihovega preprečevanja z združitvijo eksperimentalnih metod in računalniškega modeliranja.

Glavni cilj raziskave je bil podrobno preučiti proces rasti dendritov in razviti učinkovite pristope za njihovo omilitev z združevanjem slikanja z magnetno resonanco (MRI) za *operando*, neinvazivno spremljanje elektrodepozicije, ter računalniško simulacijo na osnovi algoritma agregacije, omejene z difuzijo (DLA), ki zanesljivo opisuje naključno naravo rasti dendritov.

MRI je omogočil neinvazivno spremljanje elektrodepozicije in rasti dendritov v simetričnih celicah litij–elektrolit–litij. Posnetki so razkrili kompleksne strukture z različnimi morfologijami, odvisnimi od obratovalnih pogojev. Primerjalni poskusi s preprostimi, paralelnimi in serijskimi topologijami elektrod so pokazali, da paralelna povezava spodbuja nenadzorovano rast filamentov, medtem ko serijska konfiguracija zagotavlja enakomerno ploskovno odlaganje. MRI je obenem sledil frontam izčrpavanja elektrolita ter kopičenju pasiviranega »mrtvega« litija ter zaznal nastajanje plina, kar omogoča celovit vpogled v nukleacijo in rast litijevih dendritov.

Za nadgradnjo MRI-opazovanj je bil razvit razširjeni tridimenzionalni DLA-algoritem, sklopljen z reševanjem Laplaceove enačbe električnega potenciala, ki je reproduciral vzorce odlaganja in pokazal, da je ohmski padec napetosti glavni selektor mest odlaganja. Dvodimenzionalni večdelčni DLA-model (MBDLA) je razširil analizo z upoštevanjem koncentracije ionskega elektrolita in površinske kinetike ter oblikoval morfološki fazni diagram, ki ponazarja prehode od redkih fraktalov do gostih oblog.

Ugotovitve potrjujejo sodobno elektrokemomehansko razumevanje elektrodepozicije; morfologijo dendritov določajo gradienti koncentracije elektrolita, lokalne heterogenosti gostote toka ter številni kemični in mehanski pojavi na medfazni površini. Na podlagi teh spoznanj disertacija predlaga strategije za omilitev dendritov, ki vključujejo homogenizacijo porazdelitve toka, elektrolite z visoko koncentracijo in difuzivnostjo ter inženirske medfazne plasti za regulacijo površinske kinetike.

Razvite metodologije ponujajo zanesljiva orodja za napovedovanje vedenja dendritov in načrtovanje varnejših ter učinkovitejših LMB. Prihodnje raziskave bodo usmerjene v širitev uporabe MRI kot neporušne analitske metode v baterijski znanosti ter v razvoj pristopov za preprečevanje dendritov na osnovi nadzora ionskega transporta.

Contents

List of Figures **xv**

List of Tables **xvii**

Abbreviations **xix**

1 Introduction **1**
1.1 Problem Definition ... 1
1.2 Aims and Goals of the Thesis ... 5
1.3 Hypothesis ... 6
1.4 Content ... 7

2 Lithium Dendrites **9**
2.1 Fundamental Mechanisms of Dendrite Formation ... 9
2.1.1 Ionic Transport ... 10
2.1.2 Electrode Surface Roughness ... 11
2.1.3 Stress Evolution and Mechanical Deformation ... 11
2.1.4 Electrochemical Kinetics ... 12
2.1.5 Thermal Effects ... 13
2.1.6 The Role of SEI ... 14
2.1.7 Conclusion ... 15
2.2 Mathematical Models of Dendrite Formation ... 15
2.2.1 Continuum Models ... 15
2.2.2 Molecular Dynamics Simulations ... 19
2.2.3 Discrete Stochastic Models ... 21
2.3 NMR and MRI in Electrodeposition Research ... 26
2.3.1 Nuclear Magnetic Resonance (NMR) Spectroscopy ... 26
2.3.2 Magnetic Resonance Imaging (MRI) ... 30
2.3.3 Conclusion ... 34
2.4 Dendrite Prevention ... 34
2.4.1 Electrolyte Engineering ... 35
2.4.2 Anode Surface Modification ... 36
2.4.3 SEI Engineering ... 37
2.4.4 Other Methods ... 38

3 MR Imaging of Lithium Dendrite Growth **41**
3.1 Introduction ... 41
3.2 Materials and Methods ... 42
3.2.1 MRI Instrumentation ... 42
3.2.2 Pulse Sequence ... 43
3.2.3 Electric Current Source ... 44
3.2.4 Electrolyte Characterization ... 44

3.2.5 Housing Manufacturing 45
3.2.6 Development of the Imaging Cell 46
3.2.7 Studies 50
3.2.8 Image Processing Methods 51
3.3 Results52
3.3.1 Cell Configuration Study 52
3.3.2 Polarity Reversal Study 58
3.4 Discussion 63
3.4.1 Cell Configuration Study 63
3.4.2 Polarity Reversal Study 66
3.5 Conclusion 69

4 Electrodeposition Modelling **71**
4.1 Introduction 71
4.2 Simple Deposition Prediction Model 72
4.2.1 Materials and Methods 72
4.2.2 Results 74
4.2.3 Discussion 78
4.3 2D MBDLA Model 80
4.3.1 Materials and Methods 80
4.3.2 Results 83
4.3.3 Discussion 89
4.4 Conclusion 92

5 Conclusions **95**
5.1 Experimental and Modelling Results 95
5.2 Implications for Battery Design and Operation 96
5.3 Limitations 97
5.4 Future Directions 97
5.5 Final Thoughts 97

References **99**

Bibliography **111**
Publications Related to the Thesis 111
Journal Articles 111

Biography **113**

List of Figures

Figure 1: Images of lithium dendrites 2
Figure 2: Schematic representation of various battery types 3
Figure 3: Schematic illustrating (A, B) Li plating at the anode 14
Figure 4: Phase-field simulation of Li dendrite growth 18
Figure 5: A molecular dynamics simulation of lithium dendrite growth 20
Figure 6: DLA-based simulation results of 3D manganese dendrites [59]. 23
Figure 7: Schematic representation of Li NMR signal 30
Figure 8: 3D MRI images of Li-metal cells 32
Figure 9: Experimental equipment 42
Figure 10: First cell design for early imaging experiments (A) and later design 48
Figure 11: First cup-type cell design (A) and a later evolution of the cell (B). 49
Figure 12: Latest development of the imaging cell 49
Figure 13: Cell assemblies for the cell configuration study 50
Figure 14: Dendritic growth imaging and segmentation 53
Figure 15: Temporal histogram analysis for threshold determination 54
Figure 16: Apparent dendrite volume vs. time 55
Figure 17: Time-Lapse of anode plating (single-cell experiment) 56
Figure 18: Calibrated Dendrite Volume (Corrected for Filling Fraction). 57
Figure 19: Relationship Between Voxel Filling Factor and MR Signal 58
Figure 20: Time-lapse of xz MRI slices 59
Figure 21: Voxel intensity differences between each sequential image 60
Figure 22: Volumes of the binary masks of the anodes 61
Figure 23: yz projections of growth rates of the growing deposits 62
Figure 24: Comparison of fractal dimensions from MRI (blue) and simulations (red) 74
Figure 25: Consecutive 2D slices and 3D reconstructions of dendrite growth 75
Figure 26: Colour maps of electric potential and current-density 75
Figure 27: Bar charts summarise 50 simulation runs per time interval 76
Figure 28: Validation of the biased-DLA model against MRI 77
Figure 29: Fractal dimension (df) of measured and simulated dendrites over time 78
Figure 30: A schematic showing the algorithm composing the MBDLA model 83
Figure 31: Phase diagrams of deposit characteristics 84
Figure 32: Representative deposit morphologies at phase-diagram extremes 85
Figure 33: Profiles of the free-ion concentration 86
Figure 34: Effect of electric field bias bE on deposit morphology 87
Figure 35: Effect of reaction rate parameter kr on deposit morphology 89

List of Tables

Table 1: Typical energy density ranges of various battery types.....1
Table 2: Properties of 1 M solution of $LiPF_6$ in EC:DMC 1:1 (v:v) [30], [114].....45
Table 3: Material properties, as listed in the respective technical data sheets. 45
Table 4: Printing parameters.....46

Abbreviations

CA	...	Cellular Automata
CC	...	Constant Current
DLA	...	Diffusion-Limited Aggregation
DMC	...	Dimethyl Carbonate
DME	...	1,2-Dimethoxyethane
EC	...	Ethylene Carbonate
FOV	...	Field of View
IDE	...	Integrated Development Environment
kMC	...	Kinetic Monte Carlo
LIB	...	Lithium-Ion Battery
$LiPF_6$	...	Lithium Hexafluorophosphate
LiTFSI	...	Lithium Bis(trifluoromethanesulfonyl)imide
LMB	...	Lithium Metal Battery
MBDLA	...	Multi-Particle Biased Diffusion-Limited Aggregation
MD	...	Molecular Dynamics
MRI	...	Magnetic Resonance Imaging
NMR	...	Nuclear Magnetic Resonance
ppm	...	Parts Per Million
PSF	...	Point Spread Function
RF	...	Radio Frequency
SEI	...	Solid Electrolyte Interphase
SNR	...	Signal-to-Noise Ratio

Chapter 1

Introduction

1.1 Problem Definition

Lithium metal batteries (LMBs) have long attracted attention for their impressive potential in energy storage applications. With lithium being the lightest and the most electronegative material, they offer an exceptionally high theoretical energy density (Table 1) and a low electrochemical potential, which together promise a much greater energy density compared to conventional lithium-ion batteries (LIBs) [1]. Instead of relying on intercalation compounds with limited capacity, LMBs use lithium metal directly. However, there is one significant hurdle; the formation of lithium dendrites. These branching, needle-like structures can, with cycling, decrease battery performance and pose significant safety risks, including dangerous short circuits and thermal runaway.

Lithium metal was in fact used in some of the earliest rechargeable battery designs. One of the earliest rechargeable lithium batteries was developed by NASA in 1965, with the cell using CuF_2 as the cathode material [2]. It took a few iterations of testing cathode materials, to get to the first commercial Li-ion battery. Lithium cobalt oxide ($LiCoO_2$) was used to form the first reliable rechargeable Lithium battery. However, during the search for the optimal cathode material, the anode remained lithium metal. Safety concerns due to the formation of highly irregular branched lithium structures (dendrites) pushed for the research of intercalation type anode materials. In 1987, the father of the commercial lithium-ion battery, Akira Yoshino, patented the first safe rechargeable lithium battery using petroleum coke; a carbon rich oil-refinery derivate, as anode material [2]. This discovery gained him the Nobel Prize in Chemistry (2019), which he shared with Stanley Whittingham, for the discovery of intercalation electrodes and John B. Goodenough, for identifying the first stable cathode material. In recent years, the growing demand for high-energy storage systems for applications such as electric vehicles, portable electronics, and grid-scale energy storage, sparked new interest in the research of the lithium metal batteries [1]. Lighter, higher-capacity batteries, capable of powering the next generation of devices and transportation, would present significant global economic changes.

Table 1: Typical gravimetric and volumetric energy density ranges of various battery types.

Battery Technology	**Type**	**Gravimetric Energy Density (Wh/kg)**	**Volumetric Energy Density (Wh/L)**
Zinc-Carbon	Primary	50-150	50-150
Alkaline	Primary	200-400	200-400
Lithium metal (Li-$SOCl_2$)	Primary	300-500	500-800

Lead-Acid	Secondary	30-40	60-110
Nickel-Cadmium (NiCd)	Secondary	40-60	80-150
Nickel-Metal Hydride (NiMH)	Secondary	60-120	150-130
Lithium-ion ($LiCoO_2$)	Secondary	150-200	250-700
Zinc-Air	Secondary	100-160	300-600
Lithium-Sulfur	Secondary	200-400	300-600
Lithium-Air	Secondary	500-1000	Theoretical 1000-2000

Lithium dendrites are needle-like deposits that form on the surface of the lithium metal anode during repeated charge–discharge cycles due to uneven electrodeposition (Figure 1). During charging, lithium ions migrate to the anode and deposit there, but this typically doesn't happen uniformly. Surface imperfections, fluctuating current densities, or chemical inconsistencies can create "hot spots" that initiate dendrite growth. Once even a small protrusion forms, the local electric field around its tip intensifies, causing more lithium to accumulate in that specific region and encouraging further outgrowth in a self-accelerating process [3]. Lithium-ion batteries avoid this issue, by relying on the intercalation of lithium ions in between graphite structures (Figure 2).

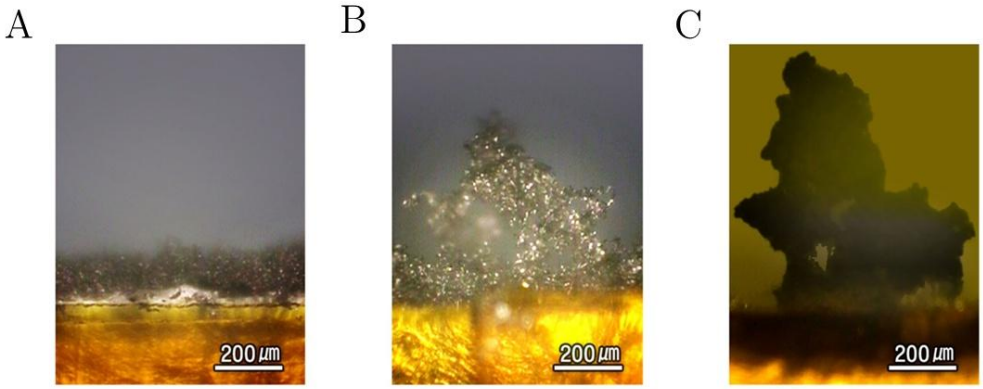


Figure 1: Images of lithium dendrites taken by a microscope during the in-situ observation of lithium deposition in various 1 M solutions: (A) LiTFSI in DME, (B) LiTFSI in tetraglyme and (C) LiI in tetraglyme [4].

The nucleation of lithium dendrites is heavily influenced by the overpotential applied during charging. Higher overpotentials lower the energy barrier for nucleation, leading to the rapid formation of numerous small lithium nuclei rather than fewer, larger deposits. While a high nucleation density might seem beneficial for uniform coverage, it paradoxically increases the likelihood that some nuclei will grow uncontrollably into dendrites [5]. Furthermore, high current densities cause the distribution of lithium ions in the electrolyte to be uneven, resulting in steep concentration gradients. These gradients promote localized deposition at points where the lithium ion concentration is highest (at the tallest dendrites), further contributing to the non-uniform growth of the electrodeposited lithium.

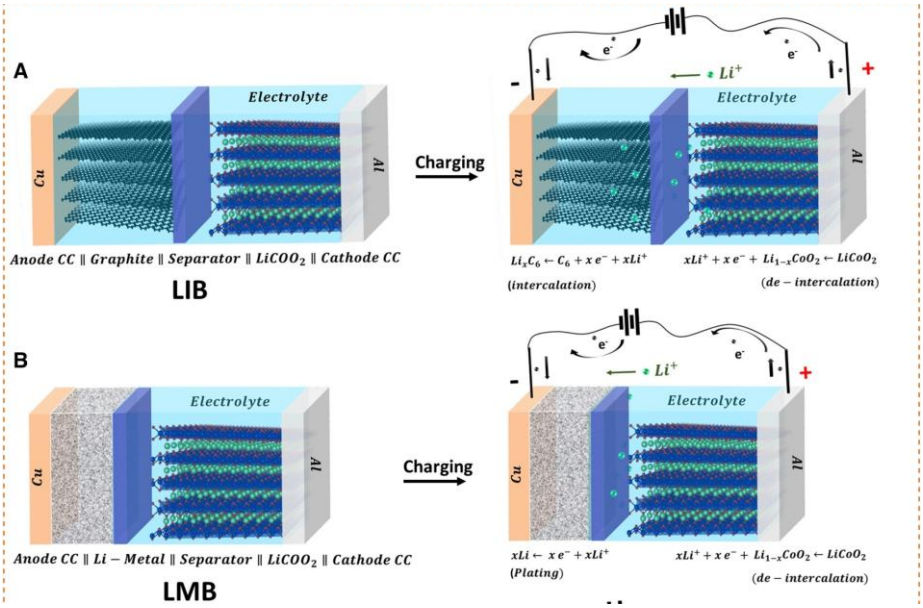


Figure 2: Schematic representation of battery types: (A) Li-ion battery (LIB), (B) Li-metal battery (LMB) [6].

In batteries, electrochemical processes are the main drivers of dendrite growth. The electrodeposition kinetics are influenced by both the applied current density and the inherent properties of the electrolyte. Electrolytes with high ionic conductivity tend to distribute lithium ions more uniformly across the anode surface, thereby reducing the formation of localized high-current "hot spots." In contrast, electrolytes that suffer from low ionic mobility or contain impurities are more likely to lead to regions of lithium ion depletion. This non-uniform ion distribution creates localized areas where the overpotential is higher, triggering preferential lithium deposition and the subsequent growth of dendritic structures [7].

Besides electrochemistry, mechanical stresses also influence the formation and evolution of dendrites. As lithium metal is deposited, the anode experiences significant volumetric changes, leading to strains in the material. Under certain conditions, compressive stress may actually hinder dendrite growth by lowering the effective exchange current density at the dendrite tip. In contrast, tensile stresses, often caused by repeated electrode expansion and contraction during battery cycling, tend to accelerate dendrite growth [5]. The effects of chemistry and mechanical stresses are not independent. The surface is covered with a mechanically fragile, complex mixture of compounds, which results from the chemical processes occurring when lithium metal is exposed to solvents in the electrolyte, called the solid electrolyte interphase (SEI). The changes in the strain of the lithium metal surface can damage this protective layer. On one hand, a stable SEI can help to moderate lithium deposition and reduce dendrite growth. But if the SEI is uneven or unstable, it fails to protect the underlying lithium and can create additional pathways for dendritic nucleation [8].

One of the less catastrophic consequences of lithium dendrite formation is performance (capacity) degradation. As dendrites grow, they increase the effective surface area of the lithium metal, which in turn accommodates more unwanted side reactions with the electrolyte. These side reactions consume active lithium and electrolyte components, gradually depleting the battery's capacity. Moreover, the continuous formation and degradation of dendrites contribute to a non-uniform current distribution across the electrode, further accelerating the decline of the battery's efficiency and cycle life [3].

A more critical consequence is the safety risk associated with prolonged dendrite growth. If these needle-like structures extend far enough, they can pierce the battery's separator, which keeps the anode and cathode apart. This allows for a direct electrical path between electrodes, leading to an internal short circuit. The sudden surge in current generates excessive heat, which can trigger thermal runaway. This extreme reaction poses a serious fire and explosion hazard, making dendrite suppression a top priority for commercial lithium metal batteries (LMBs).

One of the most challenging aspects of properly understanding dendrite growth is its dynamic and multiscale nature. Dendritic structures are not static; they evolve continuously during battery operation under the influence of varying electrochemical and mechanical conditions. Their morphology is fractal-like, characterized by branching patterns that emerge over a wide range of length scales. This complex morphology makes it difficult to predict and control dendrite formation using conventional modelling approaches. Even advanced computational models, such as phase-field methods and quantum atomistic-scale simulations, struggle to capture the highly nonlinear behaviour of the system [7].

The field of dendrite mitigation, specifically for lithium metal batteries, has been heavily studied, especially recently. Numerous strategies have been proposed, most of them mainly based on either electrolyte additives, the design of novel anode architectures, and the introduction of protective interlayers. Many techniques rely on achieving uniform nucleation via engineering a more stable SEI layer. Some additives, such as lithium nitrate, have been shown to modify the composition and stability of the SEI. Another promising technology are solid-state electrolytes, which may provide a physical barrier against dendrite penetration, to some extent [9]. Additionally, structural modifications such as three-dimensional current collectors and nanostructured anode hosts have been explored to promote uniform lithium deposition [7]. Despite these efforts, none of the strategies thus far have fully solved the dendrite problem in a way that is (yet) economically scalable for commercial applications. Each mitigation strategy has its downsides. Solid-state electrolytes are known for struggling to achieve high current densities, thus making them unsuitable for high-power applications. Protective interlayers face uncertainty in terms of long-term stability. These limitations underscore the complexity of the dendrite problem and emphasize the need for a deeper understanding of the fundamental mechanisms that drive it.

Accurate characterization of lithium dendrites is crucial for unravelling the complex processes that drive their formation and growth. Conventional imaging methods like scanning electron microscopy (SEM) and transmission electron microscopy (TEM) provide valuable snapshots, yet they often fail to capture the dynamic, three-dimensional evolution of dendrites under real operating conditions. To fully understand the interaction between electrochemical and mechanical factors, new and improved operando techniques are needed. These approaches, ranging from advanced in-situ microscopy to non-invasive imaging methods, allow us to observe dendrite growth in real time and correlate structural changes with electrochemomechanical factors. By enhancing our ability to visualize and quantify these phenomena, the next-generation characterization tools should help in discovering more effective mitigation strategies for safe, long-lasting, rechargeable lithium metal batteries.

In summary, dendrite formation remains the central hurdle preventing the widespread commercialization of high-energy-density lithium metal batteries. Driven by a combination of electrochemical instabilities, localized ion depletion, and mechanical stresses, dendrites rapidly diminish capacity, trigger harmful side reactions, and pose significant safety risks. Their inherently dynamic, multiscale growth further complicates predictive modelling and control. While numerous mitigation strategies have been studied, none has fully solved the

dendrite issue in a scalable manner. Advanced imaging methods like MRI offer promising insights into dendrite dynamics, but additional refinement is needed [10], [11], [12]. Ultimately, overcoming the dendrite challenge will require collaborative breakthroughs in electrochemistry, materials science, and diagnostic techniques, paving the way for safer and more efficient energy storage systems.

1.2 Aims and Goals of the Thesis

This thesis addresses critical challenges in the development of rechargeable lithium metal batteries by focusing on two interconnected areas: non-invasive, in-situ dendrite characterization using Magnetic Resonance Imaging (MRI) and the numerical simulation of the electrodeposition process. Dendritic growth—a key issue in lithium metal batteries—poses significant risks to safety and performance. By advancing our understanding of dendrite formation and behaviour through both experimental imaging and computational modelling, this work aims to bring us closer to more reliable and efficient energy storage solutions.

The motivation for this study stems from the urgent need to improve scientific coverage and understanding of growth of dendritic structures in lithium metal batteries. Current challenges in battery performance and safety are largely attributed to uncontrolled dendritic growth during battery charge and discharge cycles. A better grasp of these processes will not only contribute to the scientific literature but also hold the promise of significantly improving battery design and functionality. This, in turn, could lead to breakthroughs in energy storage technologies, offering more efficient and safer solutions for commercial applications.

The broad purpose of this thesis is threefold. Experimentally, the work seeks to validate MRI as a viable method for capturing the dynamic process of dendritic growth in a symmetric lithium metal cell. Once the experimental protocol is established, one goal is to study the dependence of the electrodeposition process under various operating setups (charging in series vs parallel configurations). Simultaneously, the aim is to develop a computationally efficient mathematical model that predicts macroscopic dendritic growth during electrodeposition. This dual approach is designed to shed new light on the phenomenon by linking real-time experimental data with theoretical predictions.

The research is divided into specific objectives that address both experimental and computational components. The first objective is to design a cell that is fully compatible with MRI experiments. This involves creating a detailed 3D model of the cell, carefully selecting materials that do not interfere with MRI signals, as well as other materials, and establishing an assembly process that delivers a cell that is reliable enough to keep integrity during imaging. In addition, an appropriate imaging protocol must be developed along with sequences that can acquire high-resolution images of the growing dendrites. Equally important is the development of a process for extracting quantitative data from the raw MRI images, enabling the measurement of dendritic morphology and spatial distribution.

The second objective is to design an experiment, where three different cell configurations with the same total cell volume are tested. By dividing the cell volume into compartments, in both parallel and serial configurations, we study the dendritic growth during charging for both cases and compare with a single-compartment cell. This objective again requires careful consideration of the imaging setup and protocol, as well as 3D modelling of imaging cells.

The third objective covers the numerical simulation of dendritic growth. A basic three-dimensional model is constructed based on the deposition-limited aggregation (DLA) framework [13], enhanced by incorporating electric field biasing to predict the most likely

sites of lithium deposition within the cell. Complementing this, a two-dimensional model is developed to calculate key parameters of dendritic structures, including fractal dimension, density, degree of branching, and average height. These simulation outputs are critically validated against the experimental data obtained from the MRI studies, ensuring that the models accurately reproduce the observed phenomena.

The significance of this integrated approach lies in its potential to provide a comprehensive understanding of macroscale dendritic growth from both experimental and theoretical perspectives. By bridging the gap between in-situ imaging and computational prediction, as well as exploring alternative attempts at dendrite mitigation, the work is expected to deliver insights that are not only scientifically robust but also directly applicable to the design of safer and more efficient lithium metal batteries. The anticipated contributions include an enhanced methodological framework for dendrite analysis and the development of predictive tools that could inform future battery design and operation strategies.

In summary, this thesis presents a novel and comprehensive approach to addressing the challenges associated with dendritic growth in lithium metal batteries. By leveraging MRI for in-situ imaging and developing computational models to simulate dendritic behaviour, the research offers a dual strategy that enhances our understanding of electrodeposition processes. The combined experimental and computational efforts promise to deliver practical insights that could accelerate the development of next-generation energy storage systems, ultimately contributing to safer, more reliable battery technology.

1.3 Hypothesis

In this work, we aimed to confirm the following hypothesis:

Hypothesis 1:
MRI can effectively capture real-time images of large lithium dendrites forming inside a battery. It works by detecting changes in the NMR signal of the surrounding electrolyte, caused by the displacement of the electrolyte as well as interactions with the growing dendritic metal. While the experiment will due to the intrinsic nature of the imaging method not work with conventional battery cells, a special symmetric cell is constructed with suitable geometry and materials.

Hypothesis 2:
Charging configuration influences dendrite growth. For our experimental cells, the source of overpotential is mainly the resistivity of the electrolyte. Therefore, due to Kirchhoff's Circuit Laws, in a parallel configuration, the compartment with the highest initial rate of dendritic growth will experience a comparatively higher electric current, which starts a self-accelerating loop, causing a runaway compartment. On the other hand, the compartments connected in series should grow uniformly due to the same electric current across all compartments, thus exhibiting self-regulating properties.

Hypothesis 3:
A significant portion of dendritic deposits becomes electrically inactive. This should become evident after polarity reversal in a symmetric cell; the inactive material should not dissolve.

Hypothesis 4:

The 3D Diffusion-Limited Aggregation model is a suitable basis for building a simple, computationally non-demanding macroscale model that can reliably predict the most likely deposition sites based on any given cell geometry and state of deposition.

Hypothesis 5:
The 2D Multi-Body Diffusion-Limited Aggregation model is a suitable basis for building a model, that reflects the operating conditions, crucial to the electrodeposition process, such as current density, lithium ion concentration in the electrolyte, and the degree of surface diffusion in the simulated structures. A transition between various growth regimes can be identified based on different ranges of model input parameters.

1.4 Content

In chapter one the scope of this work is presented. The problem, or rather the gaps in the current state of research are defined and the aims and goals, as well as the hypotheses of this thesis, are presented.

The second chapter is dedicated to providing the reader with a comprehensive understanding of the current state of research regarding the electrodeposition process of lithium, and mitigation techniques. Firstly, there is a deeper dive into the fundamental mechanics of dendrite growth, and various mathematical models used to simulate this process at different size scales and degrees of simplicity. Secondly, the current state of research regarding the implementation and viability of NMR and MRI in dendrite research is presented. The last subchapter covers dendrite prevention strategies, divided into categories, based on the approach.

The third chapter is the first of two chapters dedicated to the original work for the purposes of this thesis. Chapter 3 presents the intricacies of MR imaging of the symmetric lithium cell under electrodeposition. First, the imaging of a simple cell is presented, followed by the design of the battery configuration part of the study. All results are presented, followed by a discussion.

Chapter 4 focuses on the computational modelling part of the thesis. Algorithms for both, the simple 3D model and the more advanced 2D model are presented. Again, followed by results and discussion.

Chapter 5 is dedicated to give a summary of the results and discussions from chapters 3 and 4, thus presenting an overview of the work as well as an overall conclusion to the thesis.

Chapter 2

Lithium Dendrites

Chapter 2 provides an in-depth examination of lithium dendrites, a persistent obstacle in the development of safe and high-capacity rechargeable lithium metal batteries. These needle-like deposits form due to various electrochemical and mechanical instabilities, compromising the battery's performance and raising serious safety concerns [2]. By exploring the fundamental mechanisms behind dendrite formation, current modelling approaches, advanced characterization methods, and prevention strategies, this chapter lays the groundwork for understanding how dendritic growth can be mitigated.

Section 2.1 presents the fundamental mechanisms of dendrite formation, highlighting the interaction between ion transport, electrode surface irregularities, stress evolution, and electrochemical reactions [14]. Special attention is given to the solid electrolyte interphase (SEI), whose composition and mechanical properties significantly influence dendrite nucleation and growth [15]. This section emphasizes that dendrite growth is a multifaceted phenomenon, necessitating a holistic approach for effective control.

Section 2.2 delves into the mathematical models used to describe and predict dendrite formation. Continuum models capture ionic transport and electrochemical kinetics on a macroscopic scale, while molecular dynamics simulations highlight the atomic-level interactions that guide initial nucleation [16]. Discrete stochastic methods, such as diffusion-limited aggregation (DLA), offer further insights by mimicking the random-walk processes driving fractal-like growth patterns [13]. These modelling approaches collectively illustrate the complexity and multiscale character of lithium dendrite formation.

Section 2.3 reviews the application of nuclear magnetic resonance (NMR) and magnetic resonance imaging (MRI) in studying electrodeposition phenomena. These non-invasive techniques enable real-time observation of lithium plating, revealing dynamic changes in electrolyte distribution and dendritic architectures [8], [10], [11], [17]. Recent advances in spatial resolution and imaging protocols underscore NMR/MRI's potential to study how surface chemistry, current density, and cell geometry influence dendritic growth.

Finally, Section 2.4 focuses on dendrite prevention strategies, ranging from electrolyte engineering and anode surface modifications to SEI design as well as other, less studied approaches. Although each approach has limitations, including scalability, longevity, or compatibility, these innovations represent concrete pathways toward achieving safer, longer-lasting lithium metal batteries [18].

2.1 Fundamental Mechanisms of Dendrite Formation

The first studies focusing on the dendrite growth were mainly based on the electrochemical processes such as ion transport, current densities and localized overpotentials. However, more recent research has also pointed out that mechanical forces, morphological instabilities, and thermal gradients are also involved in the process of dendrite nucleation

and growth. Hence, the term 'electrochemomechanics' has begun to be used to describe the coupled electrochemical and mechanical processes that control the dendritic behaviour in lithium metal batteries. The early studies of dendrite formation usually used simplified models of lithium plating. The initial analysis of ion depletion effect near the electrode under high current densities was made by Chazalviel [19] and this work helped to establish the basic concepts of concentration gradients in the anode region. Early models of this kind focused on the electrochemical aspects of mass transport and potential distribution, but it became apparent that the mechanism could not explain all the features of the in situ observed morphology. It was found that pressure, mechanical stress, and electrode surface topography influence significantly the pathway of lithium deposition. This subchapter will analyse the literature on electrochemomechanics of lithium dendrite growth, focusing on the important parameters of ionic transport, surface roughness, stress formation, reaction kinetics and thermal effects which influence the formation and growth of these undesirable structures.

2.1.1 Ionic Transport

As mentioned in the chapter introduction, the non-uniform distribution of ionic species that is observed during the electrodeposition process, was one of the earliest recognized reasons for dendrite growth. Traditional models include ion transport by diffusion, migration and convection. Under galvanostatic control, a high current density can quickly remove lithium ions from the vicinity of the anode interface, leading to a sharp gradient in concentration that increases local electric fields. This gradient favours the growth of protrusions. Chazalviel's work [19] is a cornerstone in modelling this concentration polarization effect. In his model, he concluded that the velocity of the growth front (v) is correlated to the anion mobility (μ_a) via:

$$v = -\mu_a E_0, \tag{2.1}$$

where E_0 is the electric field in the region of the electrolyte. He argued, that the growth is driven by the space charge that develops upon anion depletion near the cathode. In his model, if the anions are faster, they vacate the cathode region more quickly. This means that the anions do not contribute to neutralize the local positive charge left by the consumed cations. The resulting imbalance leads to a stronger local electric field which, in turn, accelerates the migration of remaining cations toward the cathode. This enhanced field drives a quicker advancement of the growth front. Later studies have expanded upon this work to include effects such as complex electrolyte compositions or solvent interactions, however, the basic principle that concentration depletion triggers instability remains valid.

Mathematically, conventional approaches to ion transport are based on the Nernst–Planck equation for a binary electrolyte. In a one-dimensional approximation for the region near the electrode, the concentration of ions $c(x,t)$ evolves according to

$$\frac{\partial c}{\partial t} = -\frac{\partial J}{\partial x} = D\frac{\partial^2 c}{\partial x^2} + \frac{z_+ F}{RT} D \frac{\partial}{\partial x}\left(c\frac{\partial \varphi}{\partial x}\right), \tag{2.2}$$

where D is the diffusivity, φ is the electric potential, z_+ is the ionic charge number (i.e., +1 for Li+), F is the Faraday constant, and R and T are the universal gas constant and absolute temperature, respectively.

Deviations from linearity when the plating happens at relatively high overpotentials or high currents. Modern models usually have more realistic boundary conditions at the electrode–electrolyte interface and often incorporate interfacial resistance terms that model

the presence of a solid electrolyte interphase (SEI) [20]. However, as increasingly sophisticated in situ measurements have corroborated, these concentration profiles are never uniform; they show up as 'hot spots' that act as nucleation sites. Consequently, any reasonable description of dendrite formation must consider how ionic transport is connected to the changes in the local electrode geometry.

2.1.2 Electrode Surface Roughness

Beyond concentration driven instabilities, electrode morphology is also found to play an important role in the initiation of dendritic growth. Small perturbations, which are due to manufacturing defects, natural surface inhomogeneities or even residual electrodeposition from the previous cycle, lead to regions of higher curvature. Some of these features may act as protrusions or sharp corners, through which the local current density may be higher than the average and lead to the selective plating of lithium in these regions [21]. This phenomenon is in agreement with classical electrochemical principles according to which the current density is assumed to depend on the local electric field, which is also enhanced at geometric protrusions.

Most of the literature reports that once a small bump is formed it can further grow and become a self-sustaining structure. Given that the overpotential in these regions becomes comparatively more negative, cations are attracted to these regions and the bump grows faster. The study by Bieker and co-workers [22] showed that even minor differences in the initial surface texture could significantly change the cycling behaviour, suggesting that simple measures for preventing dendrites might lie in more even initial surface quality. However, such strategies are not only based on the geometrical control of the substrate; mechanical and chemical changes at the electrode interface further influence these topographical effects.

The common representation of how surface irregularities evolve is based on the linear stability analysis. In a two-dimensional model, the electrode electrolyte interface can be perturbed by a small amplitude function $h(x)$. Solving the Poisson equation and relevant transport equations in the electrolyte reveals whether the perturbation grows over time. If a critical perturbation wavelength λ_c exists in which growth is favoured, the electrode is vulnerable to dendrite initiation. Initial models of this form did not include mechanical stress that arises due to irregularities. Subsequent frameworks incorporated electrochemomechanical coupling, and it was found that local stresses may act to enhance or reduce the growth of such perturbations [23].

2.1.3 Stress Evolution and Mechanical Deformation

Recently, mechanical factors have attracted growing research interest since lithium, when plating and stripping, undergoes significant volume change. Stress states can be both compressive and tensive and depend on the local geometry, adhesion properties and the confinement by the cell walls. Wood et al. [21] showed that even moderate mechanical constraints can change the direction of lithium growth and that stress fields are related to dendrite morphology in real-time experiments. They also found that compressive stress might slow down the propagation of dendrites in some regions while tensile stress may enhance the growth of protrusions in other regions.

To mathematically capture these effects, continuum mechanics approaches introduce stress–strain relationships for lithium, often through Hooke's law in the elastic regime:

$$\sigma_{ij} = C_{ijkl}\ \epsilon_{kl} \tag{2.3}$$

where σ_{ij} is the stress tensor, C_{ijkl} is the stiffness tensor, and ϵ_{kl} is the strain tensor. Being a linear mapping between two 3x3 tensors, the stiffness tensor is represented by a 3x3x3x3 matrix. Due to inherent symmetries in the material, the number of total elastic coefficients drops to 9 for an orthorhombic, 5 for hexagonal and 3 for cubic structures. These stresses can be coupled with the electrodeposition kinetics by introducing a stress-dependent term into the overpotential. The effective overpotential (η_{eff}) may then look like:

$$\eta_{eff} = \eta + \frac{\overline{\mathrm{V}}_{\mathrm{Li}}\sigma}{F}, \tag{2.4}$$

where η is the standard electrochemical overpotential, $\bar{V}_{Li}$ is the partial molar volume of lithium, σ represents the local mechanical stress (which can be compressive or tensile) and F is Faraday's constant. This modification means that compressive stress, which effectively increases the overpotential, can slow down deposition, whereas tensile stress can lower it, thereby enhancing local deposition rates.

However, lithium's mechanical behaviour is far from purely elastic. The analysis of Bower et al. shows that materials like lithium (or other high-capacity anode materials) do not behave as perfect elastic solids; instead, they undergo significant plastic (or viscoplastic) deformation even under moderate current densities. This means that, during cycling, lithium can dissipate energy through irreversible deformations rather than merely storing elastic energy. [24].

Yan et al. focused on how creep, the time-dependent deformation under stress, affects the electrode surface. Their work reveals that, during stripping, the removal of Li ions creates vacancies near the interface. Under certain conditions (e.g., when the vacancy generation rate exceeds the rate at which creep can transport them away), these vacancies accumulate to form voids. Such void nucleation leads to heterogeneous stress distributions: regions with voids experience altered local mechanical conditions that can, in turn, influence lithium deposition. In zones where creep effectively transports vacancies, stress concentrations are reduced and void formation is mitigated; in areas where this balance is not achieved, stress can concentrate and favour dendritic growth. This heterogeneous mechanical state, stemming from viscoplastic flow and void formation, can thus promote dendrite nucleation and growth in some regions while inhibiting it in others [25].

Coupling stress fields back to electrochemical reaction rates requires introducing the concept of stress-dependent chemical potential. If the local stress alters the chemical potential of Li, the flux of ions to that region can shift.

2.1.4 Electrochemical Kinetics

In a typical electrodeposition process, lithium ions migrate through the electrolyte to reach the electrode, where they undergo a reduction reaction [26]:

$$\mathrm{Li}^{+} + \mathrm{e}^{-} \rightarrow \mathrm{Li(s)} \tag{2.5}$$

The rate of this reaction depends on several factors. First, the exchange current density—a parameter that quantifies the intrinsic rate of the electrochemical reaction at equilibrium—is central to the kinetics. A higher exchange current density indicates that the electrode can sustain a larger reaction rate for a given overpotential [26]. This interface reaction rate is modelled using the Butler–Volmer equation:

$$j = j_0 \left[e^{\left(\frac{\alpha_a F \eta}{RT}\right)} - e^{\left(-\frac{\alpha_c F \eta}{RT}\right)} \right] \tag{2.6}$$

where j_0 is the exchange current density, α_a and α_c are anodic and cathodic transfer coefficients, η is the overpotential, and the other parameters carry their usual electrochemical meanings [27]. For lithium dendrite growth, the local overpotential η can vary significantly due to factors such as electrode curvature, contact resistance, and surface films. Consequently, the partial current density in protruding regions can become substantially higher than that in the bulk, accelerating dendritic growth [5].

These kinetics are heavily coupled with other effects. As mentioned in previous subchapters, the ionic mass transport in the electrolyte can play a critical role, by directly influencing the overpotential [27]. Another factor is mechanical stress. Additionally, the formation of a solid-electrolyte interphase (SEI) on the electrode surface can modify the reaction kinetics. The SEI can introduce additional resistive barriers and alter the effective overpotential required for lithium reduction [15].

Another phenomenon that can be classified under surface kinetics is surface diffusion. It refers to the motion of adsorbed lithium atoms (or ions after they're reduced) along the electrode surface. From a thermodynamic standpoint, the driving force for surface diffusion arises when there exists an imbalance in surface chemical potential. This process can significantly influence electrodeposition by smoothing out local concentration gradients, and promoting the growth of a continuous and compact film. It is usually described as an atom hopping process. Essentially, imagine an atom in a potential well, i.e. an adsorption site on a 2D lattice. The jump rate (Γ) to neighbouring adsorption sites depends on the magnitude of the potential energy barrier to diffusion (E_{diff}) and the thermal energy of the adatom. The thermal energy is reflected in the jump attempt frequency ν_{SD}. The equation below describes the relationship [28]:

$$\Gamma_{\mathrm{SD}} = \nu_{SD} e^{-E_{diff}/k_B T} \tag{2.7}$$

Overall, the electrochemical kinetics at the electrolyte–electrode interface during lithium electrodeposition is a complex, coupled process. It involves the interplay of electron transfer reactions, ion transport, interfacial phenomena like SEI formation, and even mechanical stresses; all of which determine the efficiency, morphology, and stability of the deposited lithium layer.

2.1.5 Thermal Effects

Although sometimes overlooked in theoretical models, thermal effects can be substantial during high-current charging or discharging, as joule heating and local interfacial heat generation may alter dendrite growth rates. Elevated temperatures typically increase ionic conductivity in the electrolyte and may also lower the yield stress of lithium, thus increasing the rate of dendrite growth [29].

In modelling such effects, the energy conservation equation can be appended to the system of surface kinetics, ion transport and mechanics equations, establishing a coupling between local temperature, diffusion coefficients, reaction rates, and mechanical properties. The result is a multiphysics description in which temperature, stress, and electrochemical reaction kinetics all feed back into one another. Although fully coupled thermal–electrochemomechanical models are less common in the literature, they serve as a logical next step toward more realistic simulation. High-fidelity experimental work featuring infrared imaging or embedded temperature sensors has begun to provide data for validating these thermally coupled models [9]. Nevertheless, the computational cost and complexity associated with solving such integrated problems remain non-trivial.

2.1.6 The Role of SEI

One important aspect of studying dendrite formation is understanding the role of the solid electrolyte interphase (SEl). When the reactive lithium metal comes into contact with the electrolyte, a thin protective layer is created spontaneously which stabilizes the interface between lithium and solvent components [15], [30]. Nevertheless, the fundamental characteristics of the SEl, such, as its composition, thickness, elasticity and ionic conductivity, can either suppress or worsen dendrite growth. In this way, the SEI connects electrochemical kinetics, mechanical stress, and morphological evolution, making it critical for a comprehensive understanding of lithium metal batteries.

The SEI forms due to the reduction of electrolyte components at potentials below the stability window of the solvent and salt. The SEI is a mixture of inorganic and organic species, as confirmed by X-ray photoelectron spectroscopy (XPS) and Fourier transform infrared (FTIR) spectroscopy [15], [30]. Moreover, the SEI is not a one-time formation; it evolves dynamically throughout cycling by repeatedly dissolving, repairing, and growing with each plating and stripping event [30], [31].

The SEI also functions as the barrier through which lithium ions must pass to reach the metal surface, so its ionic conductivity and thickness directly influence the charge-transfer resistance (Figure 3). Theoretical models often adjust the classical Butler–Volmer equation (Eq. (2.6) to account for an extra interfacial resistance or diffusion through the SEI [5]. If the film becomes too thick or its composition hinders lithium-ion transport, the overpotential at the electrode surface rises, which can lead to non-uniform plating and promote protrusion growth.

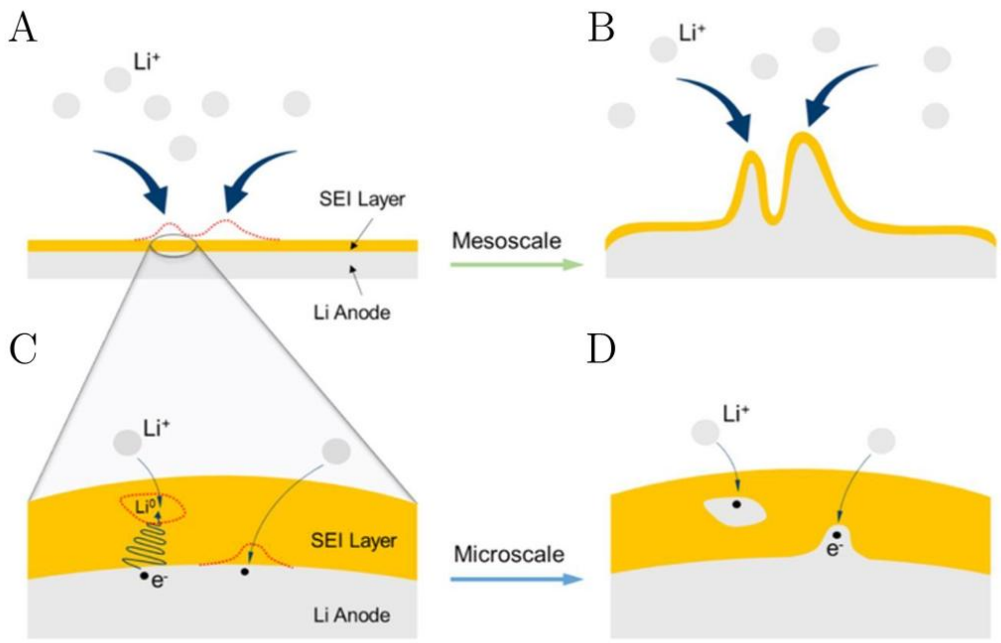


Figure 3: Schematic illustrating (A, B) Li plating at the anode during discharge cycles at macroscale and (C, D) Li dendrite nucleation and growth mechanisms at microscale [31].

Conversely, a well-engineered SEI supports homogeneous lithium-ion flux and promotes uniform deposition. Empirical studies have shown that SEI layers with higher elasticity, such as those made from lightly crosslinked polymeric species or ductile inorganic phases,

better accommodate the volumetric changes during cycling, thereby maintaining steady reaction kinetics across the electrode surface [31], [32]. In contrast, if the SEI lacks mechanical compliance, it may crack under stress, momentarily exposing fresh lithium to the electrolyte. These cracks then become nucleation sites for dendritic growth. Modelling studies often treat the SEI as a brittle film on an expanding substrate, where stress concentrations at weak points or at the interfaces between different phases can lead to crack formation [32]. Such cracks allow lithium to deposit directly against the bulk electrolyte, further encouraging dendrite formation.

Stress in the interface (SEl) may impact the electrochemical reactions as well. When the film undergoes plastic or viscoplastic deformation due to stress, it redistributes the plating currents. A famous idea put forth by Monroe and Newman is that a rigid or well matched SEl to lithium metal can hinder growth by controlling protrusion formation at the interface [5]. To achieve this practically it is essential to develop interphases, with properties and perhaps even self-repair capabilities.

Ultimately, the SEI controls what happens at the interface, between lithium and electrolyte; starting from how lithium ion's reduced to the stability of the deposited lithium itself. The SEIs formation and development dictate whether lithium deposits uniformly or forms dendrites. With advancements in modelling and diagnostic methods the relationship between SEI characteristics and dendrite growth is becoming increasingly clear.

2.1.7 Conclusion

In summary, the electrodeposition of lithium is governed not only by the migration of ions and the kinetics of charge transfer, but also by the evolution of local concentration gradients, surface roughness, and mechanical stress fields. Early models, such as Chazalviel's work on concentration polarization, laid the foundation by highlighting how non-uniform ion transport can create 'hot spots' that promote dendritic growth. Further research has shown that even minor imperfections in the electrode surface can amplify local electric fields, leading to preferential lithium deposition. Moreover, the addition of compressive and tensile stresses, coupled with the dynamic formation and degradation of the solid–electrolyte interphase (SEI), further modulates the deposition process, either suppressing or accelerating dendrite propagation. Thermal effects, though sometimes overlooked, also influence ionic conductivity and mechanical behaviour, contributing to the overall instability. Together, these phenomena show that dendrite formation is a complex problem requiring a holistic, coupled approach for proper understanding. Advancing our understanding of these interactions is critical for developing strategies to control dendrite growth.

2.2 Mathematical Models of Dendrite Formation

2.2.1 Continuum Models

Continuum models play a central role in understanding dendritic growth in lithium metal batteries by bridging fundamental mass transport, reaction kinetics, and mechanical stress phenomena. In this chapter, we review the evolution of continuum models—from early diffusion-controlled approaches, which rely on Fick's law to describe ion transport [33]—to more sophisticated sharp-interface models and phase-field methods. The sharp-interface models, exemplified by Monroe and Newman's work [5] explicitly track the moving boundary, incorporating reaction kinetics and curvature effects. Phase-field methods later emerged to overcome the limitations of explicit boundary tracking by introducing a

continuous order parameter that naturally captures complex interface dynamics. Their development marks a significant milestone in battery modelling.

2.2.1.1 Sharp-Interface Models

Sharp-interface models are essential for describing how dendritic structures evolve during processes like solidification and electrodeposition. In these early models, the boundary between two phases, such as a solid lithium dendrite and its surrounding electrolyte, is treated as a sharp discontinuity [34]. Due to the simpler treatment of the interface (compared to phase-field models) these were among the first approaches developed to study electrodeposition. While sharp-interface models are useful for giving qualitative understanding of mass transport, reaction kinetics, and the role of interfacial curvature, they are generally limited to idealized conditions.

Early work in electrodeposition modelling focused on the transport of ions. Diffusion-controlled models, as they are called, rely on Fick's second law to describe how lithium ions diffuse from the bulk electrolyte to the electrode surface [33]:

$$\frac{\partial c}{\partial t} = D\nabla^2 c. \tag{2.8}$$

In these models, the deposition rate is dictated by the local concentration gradient. When a protrusion forms, the steep gradient at its tip accelerates ion transport, reinforcing its growth relative to neighbouring areas. This basic framework explains how minor surface inhomogeneities can be amplified into dendritic structures. However, these models typically assume uniform reaction kinetics and neglect additional complexities such as mechanical stresses and interfacial curvature effects. In this context, Chazalviel's work [14] further emphasized that under high current conditions, ion depletion and space-charge formation play critical roles in triggering dendritic growth.

While diffusion-controlled models capture the essential role of ion transport, they fall short in addressing the evolving interfacial dynamics. This limitation paved the way for the development of sharp-interface models, which explicitly track the moving boundary and incorporate reaction kinetics and curvature effects.

Building on the early diffusion-controlled concepts later models introduce a more rigorous treatment of the evolving boundary between the lithium deposit and the electrolyte.

Dendrites are formed when lithium is deposited unevenly on the anode in lithium metal batteries. In this context, sharp interface models have the lithium electrolyte interface as a moving interface which is governed by ion flux and reaction kinetics [5], [16]. Monroe and Newman developed a propagation model for lithium/polymer cells that highlighted how mass transport limitations, interfacial kinetics, and local surface perturbations determine whether dendritic protrusions grow or are suppressed [16]. Their follow-up study further revealed the influence of mechanical deformation and elastic stresses on dendrite propagation [5].

Typically, these models start by solving Laplace's equation for the electrochemical potential $\mu(x,t)$:

$$\nabla^2 \mu(x,t) = 0, \tag{2.9}$$

in the electrolyte, with boundary conditions at the moving interface $\Gamma(t)$ enforcing ion flux balance

$$D\nabla c \cdot \mathbf{n}|_{\Gamma(t)} = v_n \rho_m. \tag{2.10}$$

where D is the diffusion coefficient (or effective transport coefficient) of lithium ions in the electrolyte, $\mathbf{n}$ is the interface normal, v_n is the normal velocity of the interface, and ρ_m is the molar density of the deposited material.

Additionally, a Gibbs–Thomson-like condition often appears at the interface, relating local curvature κ to the chemical potential, thus capturing the effect of surface tension or surface energy:

$$\mu_{int} = \mu_{eq} + \gamma_S \kappa, \tag{2.11}$$

where μ_{eq} is the equilibrium chemical potential of the interface and γ is the interfacial energy. This condition helps determine whether small perturbations on the interface will grow, giving rise to dendrites.

2.2.1.2 Phase-Field Methods

The sharp-interface models served as a basis for the eventual development of the more complex phase-field models. Phase-field modelling has gained significant traction in studying lithium dendrites because it can capture complex morphological changes without requiring explicit tracking of moving boundaries. In this framework, the interface between distinct phases, such as solid lithium ($\theta = 1$) and electrolyte ($\theta = 0$), is described by a continuous order parameter θ that transitions smoothly over a finite interface width (Figure 4) [35]. This approach naturally emerges from solving partial differential equations and eliminates the computational challenges associated with explicitly tracking sharp interfaces.

The method has its roots in studies of phase transitions and solidification, where a free-energy functional drives the system toward lower energy states and defines the evolving morphology. For lithium dendrite growth, the free-energy functional is typically expressed as

$$\mathcal{F}[\theta, c] = \int \left(f_0(\theta) + \frac{\epsilon^2}{2} |\nabla\theta|^2 + g(\theta, c) \right) dV, \tag{2.12}$$

where $\mathcal{F}[\theta, c]$ is a double-well potential favouring $\theta \approx 0$ or $\theta \approx 1$, ε is a parameter related to the interface thickness, and $g(\theta, c)$ incorporates chemical and electrochemical contributions that depend on both θ and the local lithium ion concentration c, f_0 is the bulk free energy density and ϵ is the strain tensor [36]. This functional is sometimes decomposed further into separate chemical and electrostatic parts, with the latter often coupled to Poisson's equation to account for local charge imbalances.

In electrodeposition contexts, while the total mass of lithium is conserved, ϕ itself is typically not conserved because it merely labels regions as either solid or liquid. Therefore, it is described by the Allen–Cahn relaxation equation:

$$\frac{\partial \theta}{\partial t} = -M_\theta \frac{\partial \mathcal{F}}{\partial \theta}, \tag{2.13}$$

where M_θ is a mobility parameter.

Variables like the lithium-ion concentration, c, represent conserved quantities. Their evolution is governed by a conservation law, typically modeled via a Cahn-Hilliard diffusion equation:

$$\frac{\partial c}{\partial t} = \nabla \cdot (D \nabla c) + \sigma_S, \tag{2.14}$$

where D is the diffusivity and σ_S includes source or sink terms (such as those from interfacial reactions). The ion concentration field is coupled to θ so that, for instance, reaction kinetics at the interface (where θ transitions) influence c, and vice versa.

Electrochemical kinetics at the electrode–electrolyte interface is incorporated by linking the local reaction rate (often modelled using Butler–Volmer kinetics) to the phase field. This coupling allows the model to dynamically capture phenomena such as nucleation overpotentials, SEI formation, and side reactions that influence lithium deposition.

Furthermore, dendrite growth in real systems exhibits strong crystallographic anisotropy, meaning lithium tends to deposit preferentially along certain orientations. To capture this effect, an anisotropic surface energy function $\gamma_S(\hat{\mathbf{n}})$ is introduced:

$$\gamma_S(\hat{\mathbf{n}}) = \gamma_0\big(1 + \delta\Omega(\hat{\mathbf{n}})\big), \tag{2.15}$$

where $\boldsymbol{\gamma_0}$ is the isotropic surface energy and $\Omega(\hat{\mathbf{n}})$ reflects orientation-dependent growth [37].

As discussed previously, mechanical stress is also critical, as lithium undergoes significant volume expansion during deposition. An elastic energy term,

$$E_{elastic} = \int \frac{1}{2}\sigma{:}\,\epsilon \; dV, \tag{2.16}$$

is added to account for stress fields that may either stabilize or destabilize growing dendrites.

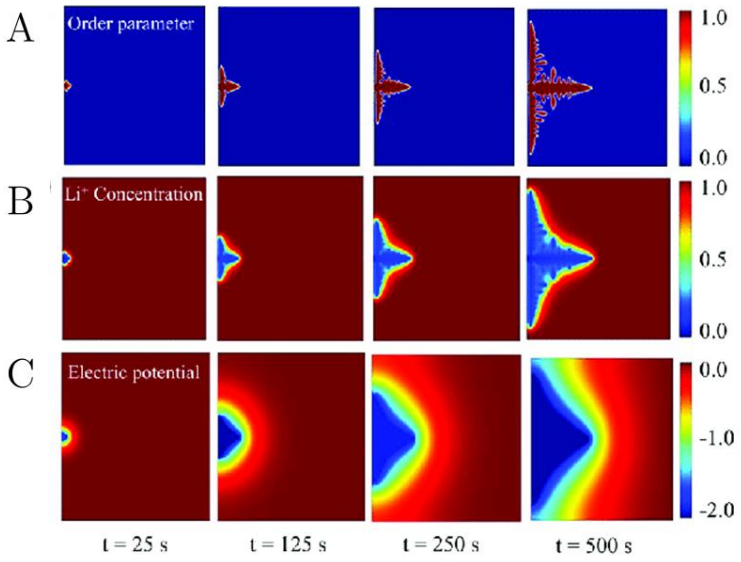


Figure 4: Phase-field simulation of Li dendrite growth. Evolution of order parameter (A), Li+ concentration (B), electric potential (C) [38].

Phase field modelling is a computationally expensive approach, especially for three dimensional systems where high spatial resolution is needed to capture the diffuse interface. These challenges can be mitigated by adaptive mesh refinement and parallel computing techniques. Additionally, the accurate parameterization of interfacial properties and

reaction kinetics is also challenging and often requires extensive experimental work and multiscale modelling. Future developments in phase field models are expected to include improved electrochemical descriptions, more efficient numerical methods, and data-driven approaches for parameter identification, leading the way to more optimized designs of lithium metal batteries of the next generation.

2.2.1.3 Conclusion

In summary, continuum models have evolved from simple diffusion-controlled approaches to sophisticated sharp-interface and phase-field frameworks that capture the complexities of lithium dendrite growth. They provide valuable insights into mass transport, reaction kinetics, interfacial curvature, and mechanical stresses, all crucial for understanding and mitigating dendritic failures. Despite limitations under idealized conditions, these models guide experimental design and optimization of electrode architectures. Future work will refine these methods by integrating multiphysics phenomena and leveraging advanced numerical techniques. Collectively, continuum models represent a powerful toolset for advancing lithium metal battery performance and safety.

2.2.2 Molecular Dynamics Simulations

Building on our discussion of continuum models, which effectively capture mass transport, charge transfer, and morphological evolution over macroscopic scales, atomistic modelling now takes centre stage by revealing the microscopic processes underlying lithium dendrite formation on metal anodes. Whereas continuum approaches describe behaviour from micrometres to centimetres, atomistic simulations delve into the nanometre-scale dynamics occurring over nanoseconds. This chapter focuses on how these methods explain fundamental phenomena such as Li-ion adsorption, nucleation, surface diffusion, and interfacial reactions, thereby linking atomic-scale events to the macroscopic dendritic structures.

Atomistic modelling of lithium dendrite formation employs molecular dynamics (MD), wherein Newton's second law,

$$m_i \frac{d^2\mathbf{r}_i}{dt^2} = -\nabla_i U(\mathbf{r_1}, \mathbf{r_2}, \ldots, \mathbf{r_N}) \tag{2.17}$$

governs atomic motion. In "ab initio MD" (AIMD), the forces acting on atoms are computed via Density Functional Theory (DFT) simulations at every timestep, thus capturing the instantaneous electronic structure of the system [39]. DFT provides a practical route to solving the Schrödinger equation for a multielectron system by recasting the problem in terms of electron density rather than the full many-electron wavefunction. This method captures the essential physics of electron interactions while making the calculations computationally manageable. The computed forces are then fed into classical equations of motion to update the positions and velocities of the atoms, which allows the simulation to evolve according to Newton's laws with quantum-level accuracy [39]. AIMD, while being extremely precise, are very computationally demanding. Therefore, AIMD is restricted to small systems (a few hundred atoms) and short timescales (picoseconds), though it provides valuable benchmark data for validating empirical potentials (Figure 5) [40].

This rigorous approach allows for accurately describing the phenomena such as making and breaking of chemical bonds, redistribution of electron density in response to atomic movements [39]. In the case of lithium electrodeposition, it is used to simulate the formation

of the solid electrolyte interphase (SEI) and giving insights into reaction mechanisms and pathways.

To overcome the scale limitations of AIMD, empirical potentials such as the Embedded Atom Method (EAM) and its variant, the Modified EAM (MEAM), are employed in classical molecular dynamics simulations. Here, the total energy is approximated as a sum of pairwise interactions plus an embedding energy that depends on the local electron density contributed by surrounding atoms. EAM thus captures the general many-body cohesion in a metal but lacks explicit angular (directional) dependence [41]. Since lithium electrodeposition is sensitive to crystallinity and the specific arrangement of atoms on the lithium surface, the directional bonding and anisotropic effects might be crucial. In such cases, the Modified Embedded Atom Method (MEAM), which includes angular terms to better capture directionality is be preferable over the standard EAM to accurately simulate nucleation and growth processes [42].

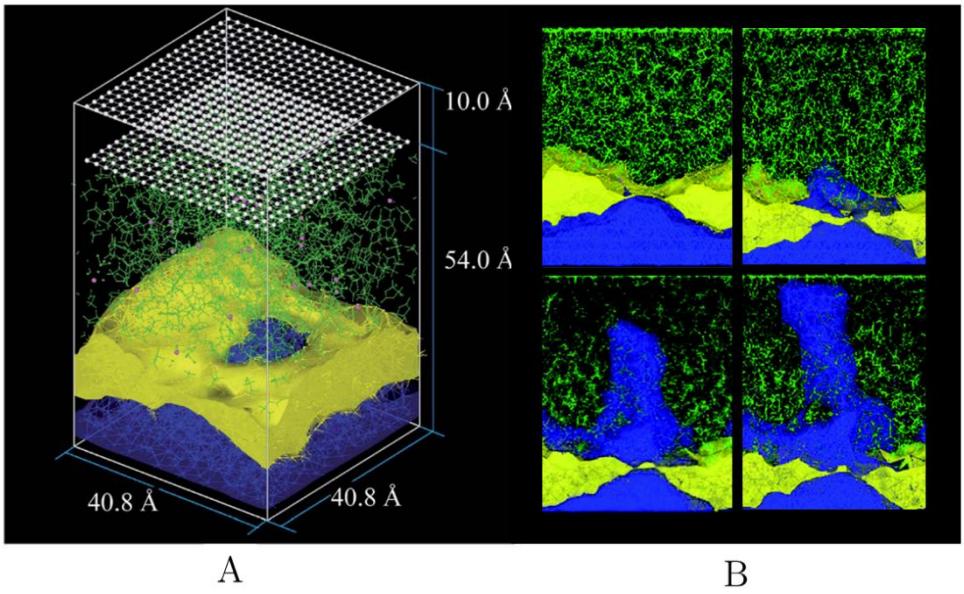


Figure 5: A molecular dynamics simulation of lithium dendrite growth. Li-metal (blue), Li^+ (pink), EC and PF_6 (green), SEI structure (yellow). Initial simulation state (A) and simulation progression snapshots (B) [40].

To bridge the gap between the high accuracy of ab initio methods and the extensive scales accessible via classical MD, machine learning (ML) potentials have emerged. These potentials are trained on large datasets of DFT calculations, offering near quantum mechanical accuracy at a computational cost similar to classical MD [43]. ML potentials are a promising route for extending simulation capabilities both in terms of length scales and timescales, while accurately capturing the complex interfacial phenomena that underlie dendrite formation.

One of the most challenging aspects of electrodeposition modelling using molecular dynamics approach is the incorporation of electrochemical conditions. Traditional MD does not inherently account for electrons or electrode potentials, yet the electrochemical environment is a critical determinant of lithium deposition behaviour. Researchers have addressed this by imposing fixed potential differences; either through adjusted atomic charges, uniform electric fields, or constant-potential (charge equilibration) schemes. One recent study integrated a constant-potential method MD to capture the dynamic nucleation of lithium dendrites under realistic electrochemical conditions [44].

Another significant challenge is the disparity between the short timescales and small spatial domains accessible to MD simulations and the longer timescales and larger length scales relevant to practical dendrite formation. Data from MD, such as diffusion coefficients, nucleation rates, and interfacial energies, can serve as inputs for continuum models that capture larger-scale morphological evolution. These multiscale coupling strategies are essential for connecting atomistic insights with full-scale battery performance [40], [43].

Experimental validations further bolster the relevance of atomistic modelling. Advanced techniques like in situ electron microscopy and atomic force microscopy provide real-time imaging of lithium deposition, offering benchmarks for simulation predictions [45]. For instance, dynamic observations have offered real-time insight into the electrochemical reaction dynamics at the lithium metal/electrolyte interface [46]. Additionally, the simulation of nanoscopic dendrite initiation highlight how local crystal decomposition at the SEI can trigger lithium clustering; a precursor to dendrite formation [43]. Moreover, complementary studies addressing strain effects [47] and self-healing mechanisms [48] further enrich our understanding of these complex phenomena.

In conclusion, atomistic and MD simulations provide a detailed mechanistic understanding of lithium dendrite nucleation and growth by capturing atomic-scale processes; from Li-ion adsorption and surface diffusion to nucleation and interfacial reactions. Despite challenges in force field accuracy and the inherent timescale gap between simulations and real-world phenomena, the integration of classical MD, ab initio MD, and ML-accelerated techniques has advanced our ability to predict and ultimately mitigate dendrite formation. Continued progress in simulation methodologies and their integration with experimental observations will be crucial for developing safer, high-energy-density lithium metal batteries.

2.2.3 Discrete Stochastic Models

Discrete stochastic simulation methods have emerged as powerful tools for bridging the gap between detailed atomistic models and continuum-scale descriptions in electrodeposition research. In this chapter, we explore three major families of such methods: diffusion-limited aggregation (DLA), Monte Carlo (MC) approaches, including kinetic Monte Carlo (kMC), and cellular automata (CA) models.

While DLA captures the fractal, dendritic growth resulting from simple random-walk deposition [13], MC/kMC models incorporate detailed kinetic processes like activation barriers and collective diffusion to provide quantitative insights into deposit morphology [49], [50].

Cellular automata, which can be viewed as a generalized framework encompassing DLA as a specific case, efficiently simulate large-scale pattern formation by updating discrete cell states via local rules [51], [52].

Together, these methods offer complementary perspectives for understanding the stochastic nature of electrodeposition phenomena across mesoscopic to macroscopic scales.

2.2.3.1 Diffusion-limited Aggregation

In previous chapters, the mesoscale and the atomic scale dynamics of dendrite growth were discussed with continuum models and molecular dynamics simulations, respectively. Stochastic methods, such as Diffusion-limited aggregation (DLA) models, Monte Carlo models and Cellular Automata models are generally representative of mesoscopic scales as well, however it can be argued that some might be applicable to macroscale phenomena when the growth process remains predominantly diffusion-limited [53]. For example,

phenomena such as viscous fingering (the unstable interface of two mixing fluids) or lightning exhibit similar fractal behaviour across different scales, suggesting that the underlying diffusion processes can produce self-similar structures at different scales [13].

Diffusion-limited aggregation (DLA) models have long been recognized for their ability to simulate the formation of branching, tree-like structures arising from random walks of diffusing particles (Figure 6). Introduced by Witten and Sander in 1981 [13], this approach was used to describe fractal aggregates formed by particles that stick upon contact with an existing cluster. DLA has since been shown to apply directly to the formation of dendritic electrodeposits in electrochemical systems [14], [54]. Phenomena such as mass transport play a heavy role in the formation of lithium dendrites, which means that the rate at which lithium ions reach the growing interface is the controlling factor in the evolution [14]. Such a regime has been identified at certain conditions, under high enough current densities, as the diffusion-limited regime [55].

The fundamental concept underlying DLA is that particles (abstract representations for the diffusing species) undergoing random Brownian motion irreversibly adhere to an existing aggregate or seed. In the simplest discrete-lattice version, one begins with a seed site. Individual particles are introduced far away from the seed, then diffused randomly until they eventually attach to the cluster. Over many iterations, the aggregate takes on a fractal form with a fractal dimension typically between 1.6 and 1.8 in two dimensions. In three dimensions, the fractal dimension is typically higher than in two dimensions, though the structures remain quite open and tree-like [56]. Witten and Sander, presented the idea that such growth patterns are universal signatures of random walk-driven processes and that the resulting "Brownian trees" reveal critical phenomena arising from irreversible aggregation events [13]. In lithium electrodeposition contexts, the species of interest is Li+. In the diffusion-limited regime, these ions migrate through the electrolyte and attach when reaching the electrode. The ion migration is the mechanism that largely determines the resulting dendrites [14].

The fractal nature of dendritic growth has been verified in numerous metals, not just lithium. For instance, Voss and Tomkiewicz [57] conducted early computational studies aimed at replicating dendritic electrodeposition processes using a DLA-type algorithm, noting that the simulated deposits display fractal characteristics consistent with experimental measurements. Similarly, Ozbey and Bayirli [58] found that the fractal dimensions of manganese dendrites formed in natural geological settings align closely with those.

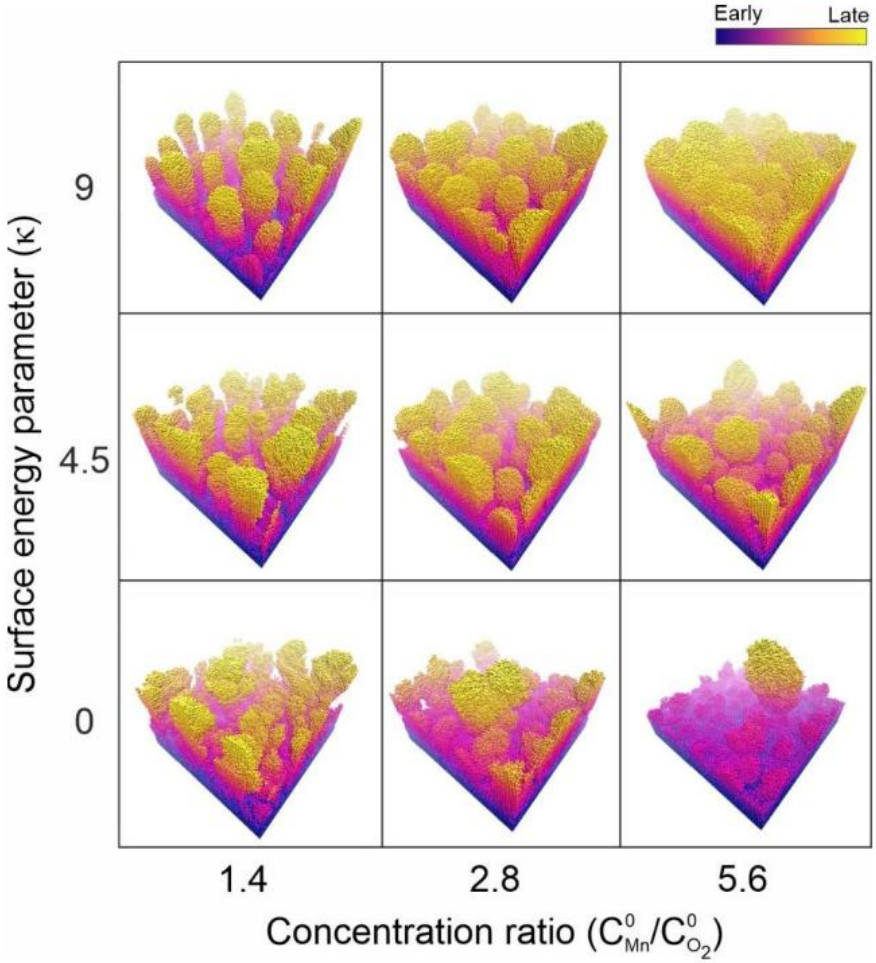


Figure 6: DLA-based simulation results of 3D manganese dendrites [59].

To tailor DLA specifically to electrodeposition, various modifications were introduced. One key extension was to include electric field bias in the random walk. Whereas the original DLA scheme assumed an unbiased Brownian motion, electrochemical deposition takes place under an applied voltage or current, imposing a directional bias to ion transport. Castro et al. presented a framework that integrated such a bias along with surface diffusion terms [54]. Their multiparticle model recognized that, under a potential difference, ions are more likely to move along the electric field gradient toward the negatively polarized electrode. They also allowed for the possibility that freshly deposited atoms, or adatoms, could migrate along the surface at a smaller but non-negligible rate. That additional "surface diffusion" mechanism can modify the local topography, smoothing certain protrusions or altering branch evolution.

DLA-based models of electrodeposition have been used to explore crossovers between nucleation-dominated regimes and dendritic growth regimes. One study examined how the nature of deposited structures transitions from small clusters to large dendrites as the applied current density or overpotential increases. At low current densities, the model predicts relatively isolated nucleation events that can remain modest in size or merge into shorter, thicker deposits. At high current densities, the morphological instability driving dendritic branching becomes more pronounced, leading to long, needle-like structures [60].

Sanchez, Bernal, and Riveiro [61] expanded the classic DLA model by simulating multiple particles simultaneously for the electrodeposition of Co-P alloys, noting that it

better captures collective shielding effects: once a branch begins to form, it can locally alter the electric field distribution, reducing ion transport to neighbouring regions. Because multiple ions can attach simultaneously or quickly one after another, the growth pattern can differ from the single-particle scenario.

Macroscale effects, such as electrode edge effects, and with that, the effect of variations in electric fields on the deposition process have also been studied with DLA. The local electric field might be strongly non-uniform near corners, protrusions, or boundaries of current collectors, favouring the rapid development of dendrites in these regions [62].

While DLA is effective in mimicking the fractal geometry of lithium dendrites, it overlooks certain crucial aspects of the system that can be important in practice. Many DLA based approaches assume that the reaction occurs instantaneously and the sticking probability remains constant once a Li+ ion or atom reaches the aggregate without consideration for reaction kinetics at the electrode surface [14]. In truth the reaction rates can be influenced by factors, like overpotential and the condition of the solid electrolyte interface (SEI). In many DLA frameworks the inclusion of the SEI is integrated into the stickiness probability.

Furthermore, the way current is distributed changes as dendrites grow according to the solutions of Laplace or Poisson equations for potential. Research has indicated that when a small disturbance occurs on an electrode surface, mass transport to the protrusion increases compared to the surrounding flatter areas, leading to faster growth of the protrusion [63].

Despite their inherent simplifications, DLA-based models remain exceptionally valuable for elucidating the role of randomness in the onset and evolution of dendritic features. They complement more deterministic continuum models and more detailed atomistic or molecular dynamics simulations by offering a view of the mesoscale, where large-scale deposit morphology emerges. Direct comparison to experiments, especially with the recent advance of 3D imaging methods, continues to confirm that the branching patterns seen in electrodeposition arise, to a significant extent, from a diffusion-limited process akin to that encapsulated by the classic DLA framework [54], [59], [61], [64]. Random walk simulations that incorporate electric field bias, surface diffusion, multiparticle interactions, and local chemical effects thus stand as an integral part of the battery modelling toolbox.

2.2.3.2 Monte Carlo Methods

Another type of models falling into this category is are the Monte Carlo (MC) and kinetic Monte Carlo (kMC) methods. These work by randomly sampling microscopic events according to their physical rates. Unlike DLA models, Monte Carlo approaches (especially kinetic Monte Carlo) allow to incorporate physical processes such as activation barriers, collective diffusion (e.g., atom hopping, atom exchange), and impact of external fields. For instance, in kMC simulations of electrodeposition, the probability of an atom hopping, exchanging places with a neighbour, or migrating in space is computed via exponential rate laws based on activation energies, and the simulation clock advances by an interval inversely related to the sum of all event rates. This framework allows the model to account for the randomness of atoms as well as more complex deterministic dynamics that influence electrodeposition.

In one of the studies focusing on Lithium electrodeposition, the Monte Carlo method was used to investigate the influence of charging protocols on the growing structures [65]. Pulsed charging conditions were investigated. Diffusion, as well as electromigration were accounted for in the model. The results of the model, as well as experimental observations on a scaled coin-cell model showed, that 1 ms pulses, followed by 3 ms rest periods can reduce the average dendrite height by 2.5 times, compared to continuous charging

(adjusted for total charging time). The simulation results imply that shorter pulses are less likely to create regions of significant ion-depletion around dendrite tips [65].

Several studies have applied MC and kMC to electrodeposition processes other than lithium. A kMC approach, using the atom potentials of the embedded-atom method, to simulate copper deposition. Their method captures the influence of activation barriers and collective diffusion mechanisms on deposit morphology, providing quantitative insight into the evolution of microstructure over realistic time scales [66].

Another study extended Monte Carlo simulations to a two-dimensional thin-layer electrodeposition process, examining how ion transport and surface reactions dictate step coverage and film uniformity in micro-scale trenches [67].

These investigations demonstrate that MC and kMC models, unlike DLA models, can provide predictions beyond the simpler fractal descriptions and can effectively bridge the gap between atomic-level events and macroscopic deposit properties [66].

2.2.3.3 Cellular Automata Models

Cellular automata (CA) models represent another class of stochastic simulation methods. In CA, the system is divided into a grid of cells each of which can exist in one of a finite number of states (for example, representing metal deposit, electrolyte, or inactive regions). Their state changes with discrete time steps (simultaneously for all cells or asynchronously via certain rules) based on simple local rules that depend on the states of neighbouring cells. These rules can be designed to mimic fundamental processes in electrodeposition, such as ion diffusion, nucleation of a deposit, growth due to local field effects, and even local reorganization, allowing CA models to capture complex pattern formation, including dendritic growth. Although they sacrifice some of the more detailed kinetics found in more sophisticated models, they are simple and therefore computationally efficient. CA models are generally used to simulate large-scale behaviour of systems [51].

Diffusion-limited aggregation (DLA) can be understood as a specialized form of cellular automaton (CA) in which the system's rules are tailored to irreversible particle aggregation. While general CA models update each cell's state based on a broader set of local rules, DLA models restrict these rules to capture the essence of diffusion-driven, irreversible aggregation. As such, DLA is essentially a CA with a very simplified, specific rule set that leads to characteristic dendritic or fractal growth patterns [64].

One study presented a combined cellular automaton – finite difference method (CA-FD), used to simulate lithium dendrite growth in lithium metal batteries. The CA part of the model was responsible for the local state changes at the electrode surface (nucleation, deposition), while the FD part is used to solve the continuum equations for ion transport and electric potential in the electrolyte.

The result show, that higher interfacial overpotentials, as well as higher current densities accelerate the growth of dendrites. Furthermore, more side branches formed in the case of high overpotential [68].

One study demonstrates a CA model in which leveller molecule additives were used. These can preferentially adsorb onto existing dendrite tips and passivate high-curvature regions, to achieve more uniform deposition [64]. The results support the theory that these molecules could significantly impact the fractal morphology, preventing branched growth and promoting uniform deposition.

Although these CA models typically sacrifice some of the detailed kinetic information provided by kMC methods, they successfully capture the emergent, large-scale morphologies of dendrites, highlighting the role of localized interactions in driving macroscopic deposition patterns. This complementary use of CA models helps bridge the

gap between simple qualitative descriptions and more computationally intensive, quantitative approaches.

2.2.3.4 Conclusion

In conclusion, discrete stochastic models give complementary insights into electrodeposition across multiple scales. DLA models generally capture the fractal, dendritic nature of depositions via simple irreversible random walks, sometimes extended to account for electric field potentials and surface diffusion phenomena [13], [54]. Monte Carlo methods on the other hand include detailed processes like activation barriers and collective diffusion [65], [66]. Cellular automata models, which can be viewed as a generalized framework encompassing DLA as a specific case [60], offer computationally efficient simulations of large-scale pattern formation and morphological evolution, even though they may sacrifice some kinetic detail. Cellular automaton models offer excellent computational efficiency for the simulation of large-scale pattern formation, but sacrifices some kinetic detail. Together, these bridge the gap between atomic-level phenomena and macroscopic behaviour, thereby complementing both continuum and molecular dynamics simulations [14], [54].

2.3 NMR and MRI in Electrodeposition Research

Lithium dendrite formation poses a key challenge in the development of safe, high-performance lithium metal batteries. While a range of diagnostic techniques can provide snapshots of dendrites after formation, magnetic resonance–based methods stand out for their ability to probe these structures noninvasively and in real time. This chapter explores how nuclear magnetic resonance (NMR) and magnetic resonance imaging (MRI) enable researchers to observe dendrite growth and associated phenomena during actual battery operation. By leveraging the intrinsic magnetic properties of nuclei, these methods deliver insights into changes in electrode morphology, electrolyte distribution, and interfacial chemistry, offering a window into the fundamental processes driving dendrite nucleation and evolution.

2.3.1 Nuclear Magnetic Resonance (NMR) Spectroscopy

2.3.1.1 NMR Signal Origin

Nuclear magnetic resonance (NMR) spectroscopy is a powerful analytical technique, that is makes use of the magnetic properties of atomic nuclei with nonzero spin. These nuclei have an inherent magnetic dipole moment. When such a nucleus is exposed to a strong external magnetic field (B_0) its energy depends on its orientation with respect to the magnetic field. This energy is given by the Hamiltonian [69]

$$H = -\gamma \hbar I_z B_0, \tag{2.18}$$

where γ is the gyromagnetic ratio, $\hbar$ is the reduced Planck's constant, and I_z is the z-component of the spin. For a spin-½ nucleus, magnetic quantum number can have the values $m_I = \pm ½$ and the corresponding energy levels

$$E = -\gamma\hbar \left(\pm\frac{1}{2}\right) B_0, \tag{2.19}$$

which yields an energy difference $\Delta E = \gamma \hbar B_0$. The populations of these energy levels at thermal equilibrium follow the Boltzmann distribution. N_- and N_+ are the number of high and low-energy level nuclei, respectively:

$$\frac{N^+}{N_-} = e^{\left(-\frac{\Delta E}{k_B T}\right)} = e^{-\frac{\gamma \hbar B_0}{k_B T}}, \tag{2.20}$$

where k_B is Boltzmann's constant and T is the absolute temperature. At typical experimental temperatures the energy difference is small, leading to only a slight population imbalance. Enough, however, to produce a net magnetization along the direction of B_0 and provide the basis for the detectable NMR signal [69]. This splitting gives rise to the characteristic Larmor precession frequency, with angular frequency

$$\omega_0 = \gamma B_0. \tag{2.21}$$

When radiofrequency (RF) radiation at the Larmor frequency is applied, nuclei absorb energy and transition between these states. The perturbation from a short, intense RF pulse tips the net magnetization vector ($M = (M_x, M_y, M_z)$) away from the z-axis, creating transverse components which precess around B_0 [69]. The subsequent relaxation back to equilibrium is described by the Bloch equation:

$$\frac{d\mathbf{M}}{dt} = \gamma (\mathbf{M} \times \mathbf{B}) - \frac{M_x \mathbf{i} + M_y \mathbf{j}}{T_2} - \frac{M_z - M_0}{T_1} \mathbf{k}, \tag{2.22}$$

where T_1 is the spin–lattice (longitudinal) relaxation time, T_2 is the spin–spin (transverse) relaxation time, and M_0 is the equilibrium magnetization along B_0. It is important to note, that this is a macroscopic equation; it does not describe the motion of individual nuclear magnetic moments, which follow the laws of quantum mechanics. Rather it represents the motion of their averages that is represented by the nuclear magnetization in the sample. Specifically, it describes how the system returns to equilibrium after excitation. As the net magnetization is tipped away from the z-axis, a transverse component M_{xy} arises, which processes at the Larmor frequency. As M_{xy} decays, primarily due to T_2 (or T_2^* when B_0 field inhomogeneities are considered), the resulting free induction decay (FID) signal can be written as [69]:

$$S(t) \propto M_{xy}(0) e^{-\frac{t}{T_2^*}} e^{-i\omega_0 t}. \tag{2.23}$$

Fourier transformation of the FID converts this time-domain signal into a frequency-domain spectrum, where resonance peaks corresponding to different interactions appear. Among these the chemical shift interaction due to different chemical environments in molecules is the most prominent interaction in nuclei with spin ½. The peak positions, line shapes, and intensities provide insights into molecular structure, dynamics, and interactions.

2.3.1.2 NMR System

The heart of an NMR system is a superconducting magnet, that produces a strong, homogenous static magnetic field (B_0). To maintain superconductivity, it is constantly cooled using liquid helium, usually in combination with liquid nitrogen as a thermal shield. The NMR probe inserts at the centre (bore) of the magnet. It contains precisely tuned radiofrequency (RF) coils, which both transmit the excitation RF pulses and receive the resulting free induction decay (FID) signals from the sample. The sample, usually contained

in a specialized tube, is positioned precisely within the sensitive volume of the probe, which corresponds to the location of the magnet, where the filed has the highest homogeneity. The spectrometer's console controls the pulse sequence and digitizes the FID, sending the data to a dedicated computer, where further analysis, such as Fourier transform, is done. Additional gradient coils are often incorporated for spatial encoding in multidimensional or imaging experiments, enabling detailed mapping of chemical environments and dynamic processes. Together, these components form a highly integrated system that converts the subtle magnetic interactions at the atomic level into valuable chemical and structural information [70].

2.3.1.3 Advanced NMR Techniques

Beyond chemical shifts, interactions between nearby nuclei through indirect spin–spin coupling (J-coupling) can split resonance peaks into multiplets. J-coupling occurs due to the interaction of nuclei and the electrons that bond them. The strength of this coupling provides information about how atoms are connected and arranged in a molecule. This enriches the NMR spectrum, offering detailed insight into molecular structure and dynamics.

Another critical aspect of NMR spectroscopy is its ability to resolve complex mixtures without the need for extensive sample preparation. In MAS, for example, the sample is spun rapidly at 54.74° relative to the static magnetic field, which averages out anisotropic interactions such as dipolar couplings and chemical shift anisotropy, yielding high-resolution spectra even for solid samples [71]. Diffusion-ordered spectroscopy (DOSY) utilizes pulsed field gradients to encode molecular diffusion into the NMR signal, allowing the distinction of species based on their translational mobility [72]. In multidimensional NMR, correlations between different nuclear spins are recorded over several dimensions, providing detailed information on molecular connectivity and spatial proximity [71]. These advanced techniques have found significant application in battery research, where in situ NMR methods can monitor the local environments of lithium ions and the evolution of electrode–electrolyte interfaces during charge–discharge cycles, thus guiding improvements in performance and safety [8].

Recent advances in NMR hardware, including the development of higher magnetic field strengths and more powerful RF amplifiers, have further enhanced sensitivity and resolution. This is particularly important when studying systems with low natural abundance or inherently low sensitivity, such as lithium metal [71]. In addition, techniques such as dynamic nuclear polarization (DNP) have been introduced to boost the sensitivity of NMR by transferring polarization from electron spins to nearby nuclei [73]. Although DNP requires careful experimental design, it offers the possibility of selectively enhancing signals from regions of interest, such as the solid–electrolyte interphase (SEI) formed on lithium metal surfaces.

Overall, the non-destructive nature of NMR, its ability to yield quantitative information, and its sensitivity to the local environment make it ideally suited for investigating electrochemical processes. In lithium dendrite research, NMR can reveal both the formation of microstructures and the evolution of the SEI without perturbing the cell's operation. These capabilities render NMR a cornerstone technique in the field of battery research.

2.3.1.4 NMR Studies in Lithium Dendrite Research

NMR began gaining traction in battery research in the early 2000s when ex situ techniques were first employed to analyse electrode composition and structure after cycling. As research progressed, in situ and operando NMR methods emerged, providing real-time

insights into dynamic processes occurring during battery operation. Today, NMR is a key tool for investigating a range of phenomena; from lithium plating and dendrite formation on metal anodes to ion transport in electrolytes and the evolving properties of the solid electrolyte interphase (SEI) [8].

A study presents an in situ ^{7}Li NMR investigation of the formation of metallic lithium microstructures during battery cycling [74]. The primary premise was to develop a quantitative, non-destructive method to monitor early dendritic growth. By leveraging the skin-depth effect of the RF field, the technique distinguishes between the bulk lithium deposit and microstructural lithium, whose NMR signal is directly proportional to its mass. Batteries were cycled under controlled current conditions while sequential NMR spectra were acquired and analysed. The results revealed that up to 90% of the deposited lithium forms as microstructures, correlating with performance degradation. This work provides a robust framework for quantifying dendrite formation, thereby offering critical insights for developing strategies to mitigate lithium dendrite growth in next-generation batteries.

Another study integrates in situ ^{6}Li/^{7}Li NMR spectroscopy with scanning electron microscopy to capture the real-time evolution of lithium deposits under operando conditions. By monitoring changes in the NMR signal during plating and stripping, the work quantitatively assesses the development of dendritic and mossy structures (Figure 7). Complementary SEM imaging provides detailed morphological confirmation, linking NMR signal variations to specific deposit geometries. It was found, that microstructure evolution is strongly influenced by parameters such as current density and electrolyte composition, which in turn affect battery safety and performance [12].

Another investigation focuses on quantifying inactive lithium, often referred to as “dead lithium”, and its role in battery degradation. Using a non-invasive, continuous in situ ^{7}Li NMR method, the study tracks the intensity variations of lithium metal signals during cycling in full-cell configurations. This technique allows for the differentiation between active lithium and electrically isolated deposits, while simultaneous electrochemical data verify the observed capacity losses. The results reveal that dead lithium formation, alongside continuous corrosion processes, constitutes a major source of irreversible capacity loss, emphasizing the importance of a stable SEI to mitigate these effects [75].

A further study enhances the sensitivity of NMR to the interfacial region between the lithium metal and the SEI by employing room-temperature dynamic nuclear polarization (DNP) [76]. Using microwave radiation close to electron spin resonance frequency, nuclei become hyperpolarized, due to the transfer of polarization via various mechanisms. Polarization is transferred from conduction electrons in the metallic lithium to nearby nuclei, thereby selectively amplifying signals from the SEI–metal interface. The method reveals chemical and structural information about the SEI, allowing for tracking of various species that form during SEI formation. The findings indicate that this technique can reliably increase the amount of signal by roughly an order of magnitude [76].

Bridging observational techniques with mathematical modelling, another study suggests an improved Nernst-Planck electrolyte model, including a concentration sink term to account for the ion depletion region near the negative electrode. Using the electrolyte ion concentration profiles obtained with NMR, the classic Nernst-Planck model predicts unphysical negative ion transference numbers. By feeding these NMR measurements into inverse modelling algorithms, the parameters in the continuum model were fitted until the simulated output (electrolyte ion concentration profiles) closely matched the experimental NMR observations. The best model was determined based on the discrepancies between the model prediction and NMR data, and validated with known material properties from the literature [77].

A slice-selective NMR diffusion method is presented to measure ion transport properties within operating battery electrolytes. This technique enables the measurement of local self-

diffusion coefficients of lithium ions. By correlating diffusion data with electrolyte ion concentration profiles, the study highlights that the electrolyte transport properties are highly concentration-dependent and in order to accurately estimate those properties, one requires spatial and temporal dependence of ions self-diffusivity. This method offers a robust way to study electrolyte properties in order to design electrolytes, suitable for cycling of lithium metal batteries [78].

A comprehensive review by Pecher et al. [8] provides an overview of the methodologies and challenges in applying NMR to battery research. This work emphasizes that, despite the high sensitivity and rich chemical information provided by NMR, issues such as low signal-to-noise ratios and the long experimental times required for certain in situ measurements remain challenges.

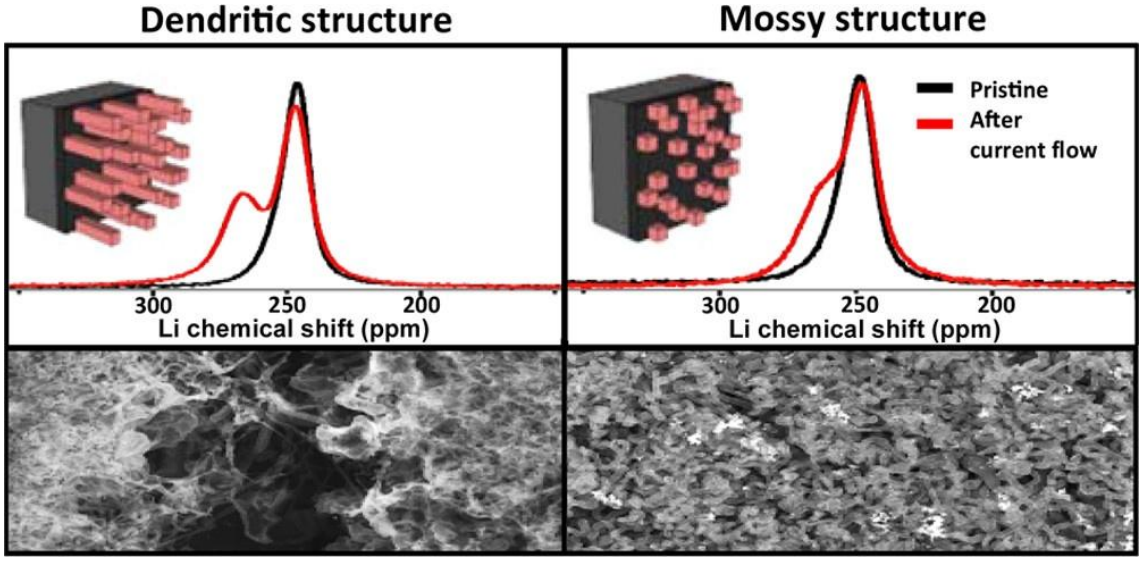


Figure 7: Schematic representation of Li NMR signal for Dendritic (left) and mossy structures (right) [12].

2.3.2 Magnetic Resonance Imaging (MRI)

This chapter explores the fundamental concepts of MRI relevant to lithium electrodeposition studies, highlights key parameters that influence image contrast and resolution, and reviews notable applications where MRI has enabled a deeper understanding of lithium dendrite formation and propagation.

2.3.2.1 Fundamentals of MRI

Magnetic resonance imaging (MRI) can be viewed as an extension of nuclear magnetic resonance (NMR) spectroscopy by enabling spatially resolved measurements, making it a powerful, non-invasive tool for investigating complex processes within electrochemical cells. In contrast with conventional NMR spectroscopy, which is largely used to extract chemical and structural information at the molecular level (as discussed in the previous subchapter), MRI introduces magnetic field gradients to encode spatial information into the measured signal.

- A gradient G_f, typically along the x-axis imposes a linear variation of the magnetic field in this direction, and with that, a linear spatial variation of resonant frequencies, which can be separated in the frequency domain.

- A short gradient pulse in a second dimension (e.g. G_ϕ), the spins acquire a phase shift, dependent on their position on the respective axis. The magnitude of this gradient pulse is varied incrementally, constructing a set of phase-encoded signals, that can be Fourier-transformed to reconstruct the spatial distribution in the y-direction.
- When a third, slice selection pulse (G_{ss}) is applied, a selective RF pulse can excite only the spins in a thin slice of the sample. The slice thickness depends on the RF pulse bandwidth and the gradient strength.

This scanning method allows to fill the whole k-space (spatial frequency domain) with data points. A Fourier transform converts this into a real image. To understand this gradient-encoding of spatial information better, we can interpret the received MRI signal as a Fourier transform of the spatial distribution of spins:

$$S(t) \propto \int \rho(\mathbf{r})\ e^{-i\phi(\mathbf{r},t)}\ d\mathbf{r}, \tag{2.24}$$

Where $\rho(\mathbf{r})$ is the spin density at position $\mathbf{r}$ and $\phi(\mathbf{r},t)$ is the phase accumulation acquired by the spins under gradient $\mathbf{G} = (G_f, G_\phi)$:

$$\phi(\mathbf{r},t) = \gamma \int_0^t \mathbf{G}(\tau)\cdot\mathbf{r}\ d\tau, \tag{2.25}$$

where γ is the gyromagnetic ratio. Introducing the k-space formalism, we define the k-space coordinate as

$$\mathbf{k} = \frac{\gamma}{2\pi}\int_0^t \mathbf{G}\ d\tau\,. \tag{2.26}$$

Rewriting the signal in terms of k-space gives

$$S(t) \propto \int\ \rho(\mathbf{r}) e^{-i2\pi k(t)\cdot\mathbf{r}} d\mathbf{r}. \tag{2.27}$$

2.3.2.2 MRI Imaging Techniques

Spin-Echo

Spin echo imaging is the most basic, commonly implemented imaging method which relies on the spin-echo phenomenon. This is created by two RF pulses, separated by a time $TE/2$, where TE is the time of the observed spin-echo peak. First, a 90° pulse flips the magnetization into the xy plane. After a period of time TE/2, a significant amount of spin-spin dephasing occurs. A 180° refocusing RF pulse effectively reverses the direction of dephasing spins, causing them to refocus in a "Spin-Echo". This technique mitigates inhomogeneity-induced dephasing effects (T_2^*) [69].

Gradient-Echo

In gradient-echo imaging, a single lower flip angle RF excitation pulse is followed by gradient reversals rather than a 180° refocusing pulse. After the excitation RF pulse, the readout gradient dephases the spins in the transverse plane; then the polarity of this gradient is reversed to rephase them, forming an echo signal. This method is typically faster than spin-echo, however, it is sensitive to both spin-spin defocusing, as well as field inhomogeneities. Gradient-echo method is useful for rapid imaging but also prone to susceptibility artefacts [69].

Inversion Recovery
Inversion recovery imaging begins with a 180° inversion RF pulse that flips the net magnetization along the z-axis. During a controlled inversion time (TI), the spins partially return to equilibrium at rates determined by T_1 relaxation. A subsequent 90° RF pulse then tips the partially recovered magnetization into the transverse plane for detection. By varying the TI, one can create strong T_1-weighted contrast or even nullify signals from specific tissues or regions, making inversion recovery sequences highly flexible for a wide range of contrast-enhanced applications [69].

Advanced MRI Methods
Advanced MRI methods include a range of techniques designed to extract more detailed or specialized information from a sample or patient. For example, echo-planar imaging (EPI) captures data for an entire image in just one or a few echoes, allowing for rapid acquisition that is critical in dynamic or functional studies. Parallel imaging utilizes multiple receiver coils to reduce scan times and improve spatial resolution, while compressed sensing algorithms further accelerate data collection by reconstructing under sampled signals through advanced mathematical techniques. Diffusion-weighted and diffusion tensor imaging characterize the mobility of particles to reveal microstructural features, such as neuronal fibre tracts in the brain or porosity in materials. Functional MRI (fMRI) detects small changes in blood oxygenation (BOLD contrast), enabling non-invasive mapping of neural activity in real time. Additionally, techniques like magnetic resonance spectroscopy (MRS) provide in situ metabolic information, and advanced hardware, such as higher-field magnets or stronger gradient systems, continues to push the limits of resolution and sensitivity for both clinical and research applications [79].

2.3.2.3 Dendrite Research Using MRI

In one of the early demonstrations of applying ^{7}Li MRI to lithium batteries, researchers were able to observe locations where metallic lithium formed within the electrode stack [17]. In this MRI method, a spin-echo sequence was used, with RF excitation pulses with frequencies chosen to only excite the bulk-metal ^{7}Li, far enough from the electrolyte peak. Additionally, ac chemical shift imaging (CSI) was performed, essentially capturing a 1D NMR spectrum in space. This enables the separation of lithium deposits from bulk electrolyte lithium. This work was a major advance, showing that MRI could track dendrite growth in operando.

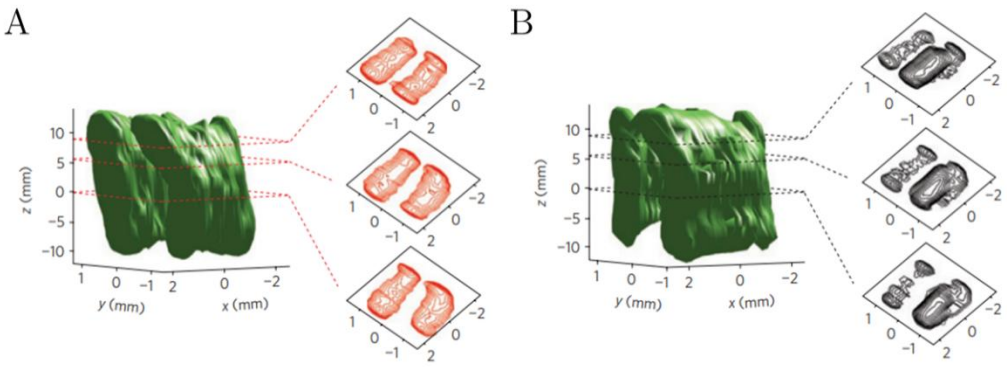


Figure 8: 3D MRI images of Li-metal cells. ^{7}Li MRI in its pristine state (A) and after charging (B). The two-dimensional slices in each panel are horizontal (x–y) cross-sections [17].

Another investigation expanded on this work to visualize more complex phenomena, such as skin effects in conductors, where electromagnetic fields decay exponentially within a conductor [80]. Specifically, by examining lithium metal electrodes, the authors demonstrated how bulk metals behave during MRI. With electrodes being modelled as thin cuboids and a perfect conductor, the magnetic fields were calculated for different orientations in respect to the RF field, taking skin effect into account. From this, the expected MRI signal was simulated and validated with MRI experiments. The results demonstrate a strong dependence of the detected MR signal on the relative orientation between the metal's faces and the rf field. For instance, faces perpendicular to the rf field experience significantly diminished excitation, attributed to opposing fields generated by induced eddy currents, while other faces show enhanced signal intensity.

One study investigates lithium dendrite growth in rechargeable batteries using in situ ^{7}Li MRI to simultaneously monitor electrolyte depletion and lithium microstructure formation [11]. By combining one-dimensional spin-echo imaging for electrolyte concentration profiles with chemical shift imaging (CSI) to distinguish pristine Li metal (250 ppm) from mossy (260 ppm) and dendritic (270 ppm) deposits, the work correlates dendrite growth with local ion transport. Cells charged at various current densities reveal that at high currents, dendrite initiation coincides with electrolyte depletion near the negative electrode, aligning with theoretical predictions based on the characteristic ion-exhaustion time (Sand's time) [14]. On the other hand, at low currents, dendrites form earlier, indicating additional growth mechanisms possibly related to solid electrolyte interphase (SEI) heterogeneity. Overall, this integrated MRI approach provides a non-invasive, quantitative tool to understand the interplay between ion transport and lithium deposition, offering valuable insights for enhancing battery safety and performance [11].

Real batteries are usually assembled using electrically conductive pouch materials, making them unsuitable for direct MRI investigation of the battery's internals. To combat this, a new MRI technique was introduced, termed inside-out MRI (ioMRI), to diagnose lithium-ion pouch cells non-destructively [81]. When a cell is placed in a strong magnetic field, the electrode materials distort the magnetic field around the cell, which can be measured using MRI. The variations of the magnetic fields act in a similar way as field gradients. Spins accumulate different amounts of phase, depending on the local magnetic field strength. Such phase images can be unwrapped, allowing for the reconstruction of magnetic field maps around the pouch. These shifts in the magnetic field were then modelled using numerical methods to determine the effective change in magnetic susceptibility, which correlates directly with the amount of lithium intercalated into the cathode material.

This means, that it is possible to determine the state-of-charge (SOC), as well as manufacturing defects using ioMRI. Extending this work, the same framework was used to track current distributions during cell cycling [82]. Beyond verifying SOC, it captures current "hot spots" and asymmetries that develop with different current rates or when cells are mechanically damaged. These field maps offer a practical way to diagnose aging or performance issues tied to uneven current flow. Together, both studies establish ioMRI as a powerful, non-destructive diagnostic tool that measures not only electrode material states but also in situ current pathways; yielding comprehensive insight into battery health and operation.

So far, some studies targeting lithium spins directly were presented. However, the intrinsic properties of lithium isotopes result in a much lower signal-to-noise ratio (SNR), compared to studied on proton (^{1}H) NMR and MRI. Protons have much higher gyromagnetic ratio, which translates to a stronger MR signal. For a nucleus with gyromagnetic ratio γ, the equilibrium magnetization (per unit volume) is given by

$$M_0 = \frac{N\ \gamma^2\ \hbar^2\ I(I+1)B_0}{3\ k_B\ T}, \tag{2.28}$$

where N is the number of spins per unit of volume and I is the spin quantum number. The signal is proportional to the time derivative of the magnetization. Therefore,

$$S \propto \omega_0 M_0 \propto \gamma B_0(\gamma^2 B_0) \propto \gamma^3 B_0^2, \tag{2.29}$$

and SNR scales roughly as

$$SNR \propto \gamma^3. \tag{2.30}$$

Given the gyromagnetic ratios of ^{1}H and ^{7}Li are (42.58 MHz/T and 16.5 MHz/T, respectively):

$$\frac{SNR_{^7_{Li}}}{SNR_{^1_H}} \approx (0.39)^3 \approx 0.06, \tag{2.31}$$

implying that ^{7}Li signal is only 6% as strong under the same conditions.

A very innovative study by Ilott *et al.* [10] presents an alternative approach. Relying on the fact that most battery electrolytes contain organic solvents, they used ^{1}H spin-echo MRI experiments to get an inverse image of the growing lithium structures. Instead of measuring the metal signal itself, changes in local susceptibility or magnetic field distributions resulting from metallic growth are tracked, giving an indirect yet highly sensitive metric of dendrite growth. Alongside that, they performed RF and static magnetic field calculations to quantify the amount of the growing structures. This study was a fundamental shift from conventional lithium imaging, providing much clearer spatial, as well as temporal information. Because the method relies on proton signals in the electrolyte, it could be readily adapted to other battery chemistries. By not requiring specialized lithium-MRI hardware this work makes fast, high-resolution in situ battery imaging accessible and offers a powerful tool for advancing next-generation battery technology.

2.3.3 Conclusion

In summary, both NMR spectroscopy and MRI contribute significantly to understanding and mitigating lithium dendrite growth. NMR provides molecular-level information on ionic species and interfacial reactions, shedding light on how dendrites originate and how they interact with electrolytes or protective layers. Meanwhile, MRI complements these findings by delivering spatially resolved images of dendrite formation under realistic cycling conditions, enabling direct (as well as indirect) visualization of electrode architecture changes. Taken together, these magnetic resonance techniques offer a powerful toolkit for correlating electrode microstructure, electrochemical performance, and safety outcomes. As further improvements in resolution and experimental design emerge, NMR and MRI are likely to play an even more integral role in advancing next-generation lithium metal battery technologies.

2.4 Dendrite Prevention

This chapter briefly introduces dendrite prevention strategies by highlighting advanced approaches such as electrolyte engineering, anode surface modifications, and SEI

optimization. These methods are designed to stabilize lithium deposition and mitigate safety risks, thereby enhancing battery performance and longevity [15].

2.4.1 Electrolyte Engineering

Recently, research has been focused on designing electrolytes that modulate Li transport, nucleation, and interfacial stability to prevent uncontrolled dendrite growth. Among the most promising strategies of dendrite prevention are electrolyte additives, high-concentration electrolytes, and the formulation of advanced materials such as liquid crystalline phases. These approaches aim to establish uniform lithium deposition while mitigating side reactions that destabilize the electrode–electrolyte interface.

One major advancement has been the use of electrolyte additives to reinforce the solid electrolyte interphase (SEI) [83]. By selecting additives that decompose preferentially at the anode surface, the resultant SEI can better accommodate volume changes during lithium plating and stripping. For instance, fluoroethylene-carbonate (FEC)-based additives have shown promise in creating LiF-rich interphases that promote homogeneous Li deposition, although recent work highlights ongoing challenges in controlling their consumption and maintaining stability over extended cycling [84]. In parallel, others have proposed alternative methods such as self-healing electrostatic shields [85], in which a charge-distribution mechanism smooths the lithium surface during plating, thereby reducing the risk of dendrite tip propagation.

Novel solvent systems also play a pivotal role in dendrite mitigation. A prime example is the crown ether-based electrolyte engineering approach [86], wherein crown ethers (cyclic compounds consisting of ether groups) and lithium ions form complexes that manage ion transport pathways, leading to more uniform plating. Similarly, liquid crystalline electrolytes demonstrate how ordered solvent domains can facilitate controlled Li diffusion and favor planar electrodeposition [87]. Another major development is the "solvent-in-salt" concept, wherein an extremely high salt concentration reduces free solvent molecules, thereby suppressing side reactions and yielding a more stable interphase [88]. Localized high-concentration electrolytes containing cyclic carbonates further illustrate how careful tuning of solvent composition can enhance Li stability and minimize dendritic protrusions [89].

Alongside these solvent and additive strategies, in situ formation of robust SEIs has also garnered significant attention [90]. The premise involves initiating interfacial reactions early in the battery's life cycle to produce a chemically and mechanically resilient barrier against dendritic growth. Complementing this approach, high transference number electrolytes have been reported to reduce concentration polarization at the electrode surface and thereby mitigate hotspot formation that triggers dendrites [91]. In these formulations, the polymer or ionic liquid matrix is engineered to transport Li preferentially, decreasing the accumulation of anions at the electrode–electrolyte interface.

Despite these advances, several challenges remain unresolved. First, there is no single electrolyte composition that guarantees universal dendrite suppression. Each formulation exhibits trade-offs among ionic conductivity, interfacial impedance, and long-term chemical stability [18]. Second, the exact mechanisms of interphase evolution, particularly under demanding fast-charge or low-temperature conditions, remain only partially understood, necessitating further in situ characterization techniques. Moreover, ensuring reproducibility and scalability is non-trivial, especially given the complexity and cost of certain novel solvents or additives.

In conclusion, electrolyte engineering has demonstrated potential to significantly mitigate dendrite growth by manipulating Li solvation, improving SEI robustness, and controlling deposition morphology. High-concentration solvents, self-healing mechanisms,

crown ethers, and carefully selected additives all contribute to building safer and more durable lithium metal batteries. Future research efforts should focus on identifying universal design rules that integrate advanced in situ diagnostic tools and computational modelling to guide electrolyte design. Such combined insights will be crucial for overcoming remaining gaps in understanding and realizing next-generation lithium batteries with improved safety and performance profiles.

2.4.2 Anode Surface Modification

Mechanical modifications, such as surface texturing and patterning, have been extensively investigated to improve lithium metal anode performance. The mechanical surface modification approach focuses on creating a controlled interface that directs lithium-ion flux during plating. By engineering the surface roughness and geometry, researchers have demonstrated that directed Li plating can mitigate the initiation of dendritic growth, which is typically associated with uneven current distribution [92].

Complementary to these efforts, hierarchical structure designs have garnered significant attention. This strategy involves constructing multi-scale architectures that not only offer mechanical stability but also guide lithium deposition from the interior to the exterior of the anode. Such designs reduce localized current densities and alleviate the stresses that contribute to dendrite formation, thereby improving both the safety and longevity of the battery [93].

Micro-patterning techniques further refine the surface engineering of lithium metal anodes. Studies have shown that introducing micro-scale patterns on the lithium surface can suppress dendrite growth by optimizing the deposition sites and lowering the peak current densities. Notably, research into patterned anodes indicates that the size and distribution of these features have a direct impact on the cycling performance and overall efficiency of lithium metal batteries [94], [95].

Controlled deposition methods also play a crucial role in dendrite prevention. By fine-tuning the deposition parameters, it is possible to achieve a more uniform lithium layer that minimizes the risk of dendrite initiation. This approach, often coupled with advanced imaging and real-time monitoring techniques, allows for precise control over the plating and stripping processes, which is essential for maintaining a stable anode interface over repeated cycles [96].

Recent strategies have extended beyond purely physical modifications to include the design of three-dimensional structures and composite matrices. The integration of ordered three-dimensional architectures not only enhances the uniformity of the lithium plating process but also provides a robust scaffold that can accommodate the volume changes inherent in lithium cycling [97], [98]. Similarly, the development of lithium-coated polymeric matrices represents an innovative approach to mitigate volume changes while ensuring dendrite-free deposition. This method leverages the mechanical flexibility of polymers to absorb stress and maintain interfacial integrity, offering a promising route toward durable lithium metal anodes [99].

Overall, the literature reflects a clear trend toward the integration of multiple engineering strategies to address dendrite growth. While significant progress has been made, challenges remain in balancing mechanical stability with high electrochemical performance. Open questions include the long-term durability of these engineered interfaces and the scalability of micro-patterning and composite matrix techniques. Future research directions should focus on optimizing these designs, understanding the interplay between electrode structure and electrolyte behaviour, and developing cost-effective manufacturing processes that can translate these laboratory-scale innovations into commercial technologies.

2.4.3 SEI Engineering

In lithium metal batteries, the SEI arises from the spontaneous reaction of lithium with electrolyte components. These reactions produce a mixture of organic and inorganic species that forms a passivating layer on the anode surface. However, many research efforts focus on artificially creating or modifying this layer to better control its composition, structure, and chemo-mechanical stability from the start.

Recent research on dendrite prevention in lithium metal batteries (LMBs) has focused extensively on tailoring the solid electrolyte interphase (SEI), as the interphase plays a decisive role in regulating ion transport and preventing unwanted dendritic growth [18], [93]. Early studies demonstrated that dendrites primarily nucleate due to non-uniform current distribution at the anode, leading to unstable plating and stripping cycles [18]. Since then, efforts have shifted to developing stable SEIs and artificial coatings that mitigate these inhomogeneities while enhancing electrochemical stability.

A critical direction involves designing hierarchical SEI structures that adapt to dynamic battery interfaces [93]. Such approaches include using multi-layered or functionally graded films that can accommodate volume changes while preserving interfacial integrity. The organic-inorganic composite SEIs have garnered particular interest, as they exhibit high ionic conductivity and robust mechanical strength [100]. Another rapidly emerging theme is the self-forming or self-healing nature of interphase coatings, wherein specific additives or polymeric networks enable the SEI to continuously repair fissures generated during repetitive cycling [101]. One example involves employing highly fluorinated electrolytes that foster a LiF-rich SEI, known for its superior mechanical resilience and chemical inertness [102].

Meanwhile, tailored polymeric binders and elastomers have demonstrated promising results in reducing local stresses and sealing cracks before dendrites can form [103]. By crosslinking lithium ions into a flexible polymer matrix, the SEI can self-heal while maintaining ionic pathways, effectively prolonging the battery's cycling life. Furthermore, recent breakthroughs in molecular engineering suggest that organic molecules can undergo in situ polymerization at the electrode interface, producing highly uniform, ion-conductive films [104]. These findings underscore the importance of precise chemical control during SEI formation, pointing to advanced electrolyte formulations and targeted additives as key design strategies.

Despite these advances, conflicting results remain regarding the optimal balance of mechanical toughness, ionic conductivity, and interfacial stability [105]. Some studies advocate for harder, ceramic-like interphases to physically block dendrite penetration, whereas others emphasize polymer-based SEIs that can flexibly adapt to volume changes [100], [105]. Additionally, questions persist about the long-term chemical compatibility of certain electrolytes with lithium metal, as well as the scalability of laboratory-scale techniques. These uncertainties underscore the complexity of simultaneously optimizing electrochemical, mechanical, and interfacial properties in a single SEI structure.

Looking ahead, a more detailed understanding of the SEI's dynamic evolution during cycling is needed, particularly under realistic battery conditions [106]. Advanced in situ characterization methods, such as cryogenic electron microscopy and operando spectroscopy, are increasingly crucial for unravelling the nuanced mechanisms behind interphase growth and dendrite nucleation. Future research directions may include the development of multifunctional interphases that incorporate self-healing, high-strength, and high-conductivity features in one coherent design. Additionally, exploring synergistic strategies that combine robust SEI architectures with novel electrode structures, such as 3D current collectors or host materials, could offer further gains in preventing dendrite formation.

In conclusion, recent work has highlighted the pivotal role of SEI engineering in achieving dendrite-free lithium metal anodes. Progress has been made in designing multi-layered, self-healing, and molecularly engineered interfaces to modulate ion transport and accommodate volumetric changes. Yet, the field still contends with competing visions for the ideal SEI composition and morphology. Continued research into advanced characterization and scalable interphase fabrication methods will be essential for realizing the next generation of high-energy-density, dendrite-resistant lithium metal batteries.

2.4.4 Other Methods

Beyond the extensively researched approaches of anode engineering, SEI formation, and electrolyte modifications, recent literature highlights several complementary strategies to mitigate lithium dendrite growth. These methods focus on optimizing charging protocols, applying mechanical stress or external pressure, designing advanced separators, and enhancing mass transfer during electrodeposition.

One promising strategy is the optimization of charging protocols, particularly through pulse charging. Pulse charging techniques involve applying intermittent current pulses rather than continuous charging. This method allows brief relaxation periods during which concentration gradients can equilibrate, thereby reducing localized high current densities that typically lead to dendrite formation. Mayers et. al. demonstrated that pulse charging can significantly mitigate dendritic growth, leading to more uniform lithium deposition [90]. In a similar vein, research has shown that modulating the internal electric field during charging; by reversing the dendrite growth direction and eliminating concentration polarization, can stabilize lithium deposition [107]. Such approaches expose the importance of dynamic charging strategies that adjust current density in response to local conditions, suggesting that smart charging protocols may offer a viable route to extend battery life and safety.

Mechanical stress control is another area gaining attention. The application of external pressure has been revisited as a means to suppress dendrite formation by physically constraining lithium deposition [108]. By carefully engineering the cell's mechanical environment, it is possible to impose a uniform compressive force that deters the formation of protrusions and encourages the growth of a dense, uniform lithium layer. This approach is particularly attractive because it leverages fundamental mechanics without requiring major modifications to the electrode materials themselves.

Functional separator design also plays a crucial role in preventing dendrite penetration. Recent developments in separator technology have focused on integrating mechanically robust, ionically conductive layers that physically block dendrite propagation while maintaining high ionic transport. One study describes a multi-layered separator architecture that combines a flexible polymer matrix with ceramic coatings [109]. Such separators not only inhibit the mechanical penetration of dendrites but also contribute to a more homogeneous ion distribution across the cell. This dual function is essential for high-energy applications where even minor dendritic growth can compromise cell integrity.

In addition to these strategies, enhancing mass transfer during electrodeposition has been recognized as a critical factor for achieving uniform lithium deposition. It was demonstrated that optimized electrode geometries and improved electrolyte flow can facilitate a more uniform distribution of lithium ions [110]. By reducing the localized depletion of lithium and ensuring steady ion flux, these design modifications help prevent the formation of concentration gradients that trigger dendritic growth.

Trends across these studies suggest that integrating multiple control methods, such as combining optimized charging protocols with mechanically robust separators, can synergistically improve dendrite suppression. However, open questions remain regarding

the optimal balance between these approaches. For example, the trade-off between applying sufficient mechanical pressure to prevent dendrites and avoiding excessive pressure that may damage cell components is not yet fully resolved. Similarly, while pulse charging has shown promising results in laboratory settings, its scalability and compatibility with existing battery management systems require further investigation.

In conclusion, recent advances emphasize that effective dendrite prevention in lithium metal batteries may require an approach that combines innovative charging protocols, controlled mechanical stress, advanced separator design, and enhanced mass transfer techniques. Future research should focus on integrating these methods into practical cell designs and establishing scalable manufacturing processes that maintain battery performance and safety.

Chapter 3

MR Imaging of Lithium Dendrite Growth

3.1 Introduction

Chapter 3 bridges the gap between theoretical models and practical observation by using operando ^{1}H MRI to follow lithium plating and stripping inside an otherwise opaque cell. Our first hypothesis is that how you wire identical lithium half-cells, either in series or in parallel, dictates whether dendrites grow in a self-regulated, uniform fashion or run away in just one compartment. The second hypothesis proposes that "dead" lithium, which no longer participates in cycling, can be revealed by deliberately reversing current once per experiment and watching which deposits fail to dissolve. Indirect ^{1}H MRI, which images the proton-rich electrolyte rather than lithium metal itself, provides the necessary non-invasive, three-dimensional view at a few-hundred-micrometre resolution.

The chapter's first study tests the influence of circuit topology. A single housing is re-configured three ways—as one large cell, as four parallel sub-cells, and as four sub-cells wired in series—then charged at the same total current while rapid, sequential 3D scans track where the electrolyte signal is displaced by growing dendrites. By comparing dendrite volumes and morphologies across these modes, we directly probe whether series connections indeed enforce uniform growth and whether parallel connections allow runaway behaviour.

The second study uses the same symmetric Li|Li cell but drives it with a single reversal of the applied current. This polarity-cycling experiment lets us observe which portions of plated lithium strip away when the field flips, and which remain "dead", within one continuous imaging sequence. Because the cell is symmetric, the electrodes simply reverse roles, offering a direct test of how well reverse-plating can heal or reveal inactive deposits; a test, that MR imaging should give a clear answer for.

After introducing the design of our MRI-compatible phantom and the evolution of its sealing and gasket materials, the chapter details the materials, instrument settings and data-processing routines common to both studies. We then describe the specific conditions for each experiment, present their imaging results, and interpret them in a unified discussion. A brief conclusion highlights the key takeaways and prepares the ground for the modelling work in Chapter 4.

3.2 Materials and Methods

3.2.1 MRI Instrumentation

All experiments were carried out on a 9.4 T wide bore vertical superconducting magnet (Jastec, Tokyo, Japan) (Figure 9). The setup included a 30 mm bore Bruker Micro 2.5 microimaging system (Bruker, Ettlingen, Germany) with a maximum gradient strength of 650 mT/m, a Tecmag Redstone spectrometer (Tecmag, Houston, TX, USA), for pulse sequence control and signal acquisition. In all experiments, the assembled cell is placed in the centre of the bore (*xy*-plane) and in the region where the static field is most homogenous.

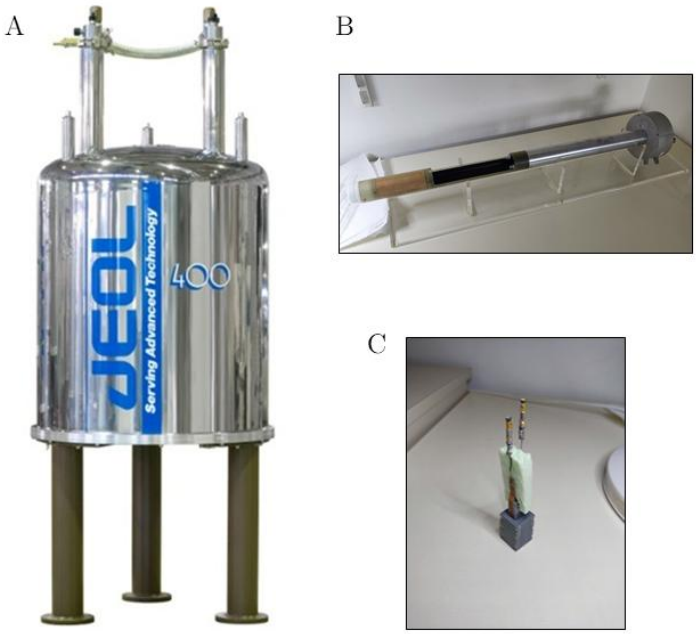


Figure 9: Experimental equipment; Jastec 400 MHz WB magnet (A), Bruker MICRO 2.5 gradient/RF probe (B) and the imaging phantom, ready to be inserted into the probe (C).

Sample positioning in an MRI system can be critical for image quality. Lithium has a high magnetic susceptibility. When exposed to a strong magnetic field, such as B_0, the difference between the susceptibilities in an environment can significantly distort the magnetic field. As discussed in previous chapter, such inhomogeneities result, depending on the imaging sequence used, in image artefacts. Aligning the electrodes in a particular orientation in respect to the static magnetic field B_0 is crucial for minimizing magnetic susceptibility effects. It was found that positioning the electrodes so that its largest surface lies parallel to the B_0 field minimizes image artefacts. This minimizes the cross-section that interacts with B_0 [111], [112].

Furthermore, proper orientation of electrodes in respect to the RF field (B_1) is essential for achieving a homogenous distribution of sample excitation. RF pulses induce eddy currents in conductive materials, which produce their own, opposing magnetic field. Improper alignment results in both areas of over- and under-excitation. Again, some imaging protocols are more, some less susceptible to these variations. Inhomogeneous

absorption of the RF pulse energy may result in not only distorted images but may also impact the experiment. Uneven heating of the electrodes can impact reaction rates. It was found that orientating electrodes parallel with respect to B_1 is optimal [111], [112]. Due to this reason, the RF probe was operated in single channel (linear polarization) mode.

Finally, a custom, in-house build low-pass RF filter is used in-line between the cell and electric current source. As the lithium plates act as antennae, that pick up the signal generated by the RF probe, this piece of hardware is necessary to isolate the cell from the current source.

3.2.2 Pulse Sequence

In indirect imaging of lithium dendrites, choosing between spin-echo and gradient-echo sequences involves balancing trade-offs between contrast, speed, and artefact suppression. Spin-echo sequences offer robust images with desired NMR relaxation weighting, reduced susceptibility artefacts and improved resilience to magnetic field inhomogeneities due to their refocusing pulses. However, these sequences require longer scan times and higher RF power, potentially leading to sample heating, and as they are less sensitive to T_2^* effects[113], they might miss subtle changes in dendrite structures. In contrast, gradient-echo sequences are faster and more sensitive to local magnetic susceptibility differences, accentuating small dendrite-induced variations through T_2^* contrast. Yet, this sensitivity can also lead to significant artefacts and lower signal-to-noise ratios, complicating interpretation.

The potential downside of gradient based methods is lower spatial imaging resolution. As this method is T_2^* weighted, it is more susceptible to signal distortions due to growing dendrites. While this means potentially higher contrast, it could result in loss of spatial information in cases, where magnetic field would be essentially "shielded" over the range of multiple voxels as a result of growing dendrites.

In the context of indirect dendrite imaging, a gradient-echo based method was already studied [10]. The authors stated that spin-echo sequences could also be used for this application, they highlighted the fact that RF inhomogeneities compromise their use, resulting in image distortions. This is true especially for fast/turbo spin-echo sequences, where signal distortions accumulate with each consecutive refocusing pulse.

Our aim was to explore the viability of spin-echo sequences. We hypothesized that a well-designed imaging experiment could overcome the issues associated with spin-echo methods, such as prolonged imaging times and imaging artefacts induced by metallic deposits. Simultaneously, the benefits of such an approach could be leveraged, to obtain images that capture more structural details of dendrites.

The RARE MRI imaging method (Rapid Acquisition with Relaxation Enhancement) is a fast spin-echo technique that dramatically reduces scan time by generating a train of echoes following a single excitation pulse. Instead of acquiring one echo per excitation, the method applies a series of 180-degree refocusing pulses to create multiple echoes that fill different parts of k-space in a single shot. In our case, a train of four echoes was used, repeated two times for signal averaging.

Here, a possibility of using a driven-equilibrium spin-echo (DE-SE) sequence presents itself. The obvious benefit would be shorter imaging times, without loss in contrast. DE-SE resets the transverse magnetization after each shot, meaning most of the signal is recovered until the next TR. This could bring scan times closer to gradient echo sequences, with only a small increase of susceptibility sensitivity (which can also provide more contrast, but at a cost of spatial resolution). In addition, RARE sequences can often introduce train-length-dependant k-space weighing (and resulting edge blurring), which

could also be avoided using DE-SE. This remains an interesting avenue to explore in future fork.

3.2.3 Electric Current Source

The potential was first regulated using a standard laboratory power supply operated in current-limit mode. Although this allowed us to cap the maximum current through the cell, its built-in current regulator only offered coarse adjustment, its resolution was comparable to the target operating currents, so control accuracy proved insufficient for reproducible experiments.

To improve precision, we then built an in-house constant-current source cantered on an LM317 linear regulator. An Arduino (Arduino S.r.l., Monza, Italy) microcontroller set the LM317's trim resistor to the desired current and read the resulting cell voltage via its onboard 10-bit ADC. A simple Python script running on a PC polled the Arduino over USB and appended timestamped voltage readings to a log file. This arrangement gave fine control over current and automated potential recording, but still lacked the advanced electrochemical features required for more complex protocols.

Accordingly, all subsequent work employed a dedicated potentiostat/galvanostat, BioLogic VSP-3e, (BioLogic Science Instruments, Seyssinet-Pariset, France) in a two-electrode configuration. Experiments ran under a combined constant-current (CC) / constant-voltage (CV) regimen: during CC mode the system enforces the set current until (if) the cell potential reaches 4.0 V, at which point it switches to CV mode and holds the voltage constant. Once the current rises back to the target value, it reverts to CC operation, ensuring precise delivery of both current and potential throughout each cycle.

3.2.4 Electrolyte Characterization

The electrolyte used in all experiments is identical; a 1 M solution of lithium hexafluorophosphate salts ($LiPF_6$) in a 1:1 (v:v) mixture of ethylene carbonate (EC) and dimethyl carbonate (DMC). The electrochemical properties of the solution are reported in Table 2. As ^1H imaging will target hydrogen atoms of the solvent molecules, it is critical to determine T_1 and T_2 of the electrolyte, to properly set the imaging parameters in order to obtain images with the best possible quality.

T_1 is determined by applying two successive RF pulses (180° and 90° pulse) and varying the delay time between the pulses (τ). The first 180° pulse inverts the magnetization to the negative direction. During the delay time, the longitudinal magnetization relaxes exponentially towards the equilibrium. The 90° pulse converts the longitudinal magnetization to the transverse plane for the FID signal acquisition. The signal amplitudes immediately after the second pulse are plotted against the corresponding delay times. $T_1$is determined by fitting the exponential inversion recovery model to the datapoints:

$$S(\tau) = S_0 \left(1 - 2e^{-\frac{\tau}{T_1}}\right). \tag{3.1}$$

In our case, due to a mixture of two types of solvents, the above relationship was found to be biexponential, with T_1 values of 996 ms and 640 ms.

For T_2 measurement, a spin echo sequence with varying echo times (TE) is used. For each echo time, the echo amplitude is recorded. As with the T_1 measurement procedure, an exponential decay function is fitted to the dataset to determine T_2:

$$S(TE) = S_0 \; e^{-\frac{TE}{T_2}}. \tag{3.2}$$

The resulting relationship was found to again be biexponential, with the mean T_2 of ~530 ms.

Table 2: Properties of 1 M solution of $LiPF_6$ in EC:DMC 1:1 (v:v) [30], [114].

Property	**Reported Value**
Ionic Conductivity	~ 10 mS/cm
Viscosity	~ 3.5 cP
Density	~ 1.26 g/cm^3
Electrochemical Stability	Up to 4.5 V vs Li/Li$^+$
Li$^+$ Transference Number	~ 0.38
Binary (salt) Diffusion coefficient	~$2.5 \cdot 10^{-6}$ cm^2/s (at 20°C)
Li$^+$ Diffusion coefficient	~$2.0 \cdot 10^{-6}$ cm^2/s
PF_6^- Diffusion coefficient	~$4.0 \cdot 10^{-6}$ cm^2/s

3.2.5 Housing Manufacturing

For typical Li-ion batteries for example, aluminium laminate is used for the pouches, enclosing the battery. For MRI imaging, inclusion of electrically conductive materials is not desirable, due to aforementioned reasons. Another factor is material neutrality during imaging; meaning that under imaging operating conditions, the housing material should not produce NMR signals. This is generally not an issue, as most solid materials produce little to no signal compared to liquids. Besides that, the housing is exposed to electrolyte, which contains harsh solvents, which may degrade the housing material. Therefore, careful consideration of the choice of cell housing materials is necessary.

PEEK plastic was initially considered, as it is known to be very chemically inert, therefore making it an ideal choice, however, the production of PEEK cells was a time-costly process, as well as somewhat limited to simpler designs.

Stereolitography (SLA) 3D printing allows for cost-effective, very rapid prototyping. This process allows to go from cell modelling to finished product within a single day. SLA is an additive manufacturing process which uses an ultraviolet display to selectively cure a photosensitive liquid resin layer by layer. In contrast with fusion deposition modelling (FDM), this method produces completely solid, non-porous prints.

The materials used for the cell housing design were Prusament Resin Tough (Prusa Research a.s., Prague, Czech Republic) and Phrozen TR300 (Phrozen Tech co., ltd., Hsinchu city, Taiwan). Both materials underwent basic testing for chemical stability. Test models were manufactured and exposed to the electrolyte in an argon glovebox. After exposure both test models were visually inspected for visible changes. No discoloration, swelling, cracking, or surface degradation was observed on any model, as well as no coloration of the electrolyte was observed. Both models were also weighted before and after prolonged exposure and no significant changes in mass were observed. The material properties of both models after proper curing are presented in Table 3.

Table 3: Material properties, as listed in the respective technical data sheets. Mechanical properties correspond to cured models.

	Prusament Tough	**Phrozen TR300**
Tensile Strength	41.6 MPa	56.5 MPa
Elongation at Break	5.8 %	4.5 %
Tensile Modulus	1.6 GPa	2.7 GPa
Flexural strength	33.5 MPa	/

Heat deflection temperature (0.45 MPa)	55 °C	65 °C
Hardness (Shore D)	75.7 D	80 D
Viscosity (23°C)	180-230 mPa.s	110-160 mPa.s

Various housing parts were printed with the Prusa SL1S stereolithography printer. The printer G-codes were generated using the PrusaSlicer software using the parameters described in Table 4. After printing, post-processing of the parts was done with the Prusa CW1S post-processing station. After removing the parts from the print build plate, they were washed in two stages using isopropanol (IPA) baths for 5 minutes each. The purpose of two stage washing is to remove as much of the uncured resin as possible. The prints were then dried for 5 minutes at 45°C and cured for 20 minutes under UV light.

Table 4: Printing parameters

	Prusament Tough	**Phrozen TR300**
Exposure time @ Layer height	2.6 s @ 100 µm	1.8 s @ 100 µm
	2.0 s @ 50 µm	1.4 s @ 50 µm
	1.8 s @ 25 µm	1.2 s @ 25 µm
Bottom exposure time	25 s	20 s
Faded layers	5	
Lift time	1 s	
Lifting speed	22 mm/s	

3.2.6 Development of the Imaging Cell

Battery research encompasses a range of cell designs, each employed at different stages of development and for distinct investigative purposes. At the early stage, coin (button) cells provide a cost-effective means of quickly screening new electrode materials or electrolytes. Their straightforward assembly and small volume make them ideal for examining fundamental properties, though they can overlook certain behaviours—such as mechanical or thermal effects—that become more critical in larger formats. Moving beyond coin cells, reusable lab-scale cells (e.g., Swagelok-type) enable more precise control over cell geometry, compression, and electrode arrangement, often including three-electrode configurations that isolate the working electrode's behaviour from the counter electrode [115]. For applications closer to industry, pouch cells allow for scalable prototypes (ranging from single- to multi-layer configurations) and are frequently used to bridge the gap between lab-scale experiments and commercially relevant sizes. Finally, cylindrical (e.g., 18650, 21700) and prismatic cells offer standard packaging and robust mechanical designs, mirroring most commercial lithium-ion batteries in laptops, electric vehicles, and stationary energy storage systems [116], [117].

Despite these well-established designs, investigating battery cells using Magnetic Resonance Imaging (MRI) poses unique challenges. Because MRI is extremely sensitive to the presence of magnetic and conductive materials, most battery hardware (which contains metals and other MRI-opaque components) can introduce severe signal distortion, susceptibility artefacts, and RF shielding effects. Even non-magnetic metals may cause considerable field inhomogeneities that complicate image acquisition and interpretation. Additionally, many standard cell formats are not readily adapted to the stringent size, shape, and material constraints needed to fit inside MRI equipment, requiring customized cells made from specialized, non-metallic materials. Such modifications can limit the ability

to replicate standard internal pressures or electrode configurations, thus making it challenging to collect fully representative data on battery performance in an MRI setting.

Throughout the development of the experiment, we discovered that designing and assembling a functional lithium cell is far from trivial. Apart from a handful of studies that focus specifically on cell-failure mechanisms, little attention is paid to reporting practical difficulties. Either failed experiments are simply left out of the literature, or we were uniquely unlucky. In our case the predominant problem was the formation of gas—and the accompanying rise in internal pressure—which eventually led to electrolyte leaks. Although we followed established protocols to minimise residual moisture and oxygen exposure of both lithium and electrolyte, gas generation remains hard to suppress, because dendrite formation inevitably decomposes a significant fraction of the electrolyte.

Our first prototype was a small prismatic cell (Figure 10A) with 16 × 4 mm lithium electrodes placed 8 mm apart. The housing parts were machined from PEEK. After positioning the electrodes on the main body, we added a layer of copper foil, a silicone gasket and two PEEK covers, which were secured with M2 × 6 mm nylon screws. To simplify filling, we later introduced a fill port in the main body that was sealed with a rubber O-ring and an M2 nylon screw. This design yielded several successful experiments; however, rising pressure often forced electrolyte past the gasket, producing leaks. The decisive factor behind the uneven success rate is still unclear, but we suspect that when leakage did occur the escaping electrolyte quickly absorbed atmospheric moisture, accelerating its degradation.

To test alternative geometries, we turned to SLA 3D printing. The revised concept comprised a two-piece housing into which small strips of lithium foil were inserted before assembly (Figure 10B). The resulting structure created seven compartments whose lithium electrodes were arranged so that the electric field alternated direction from one compartment to the next, giving an overall series configuration. Each chamber was equipped with its own lateral fill port. We first tried a 3D-printed TPU gasket between the two halves; chemical compatibility with the electrolyte was uncertain, so we also evaluated flat silicone and butyl gaskets. Exposure tests showed obvious degradation of silicone, whereas TPU and butyl appeared intact, though visible integrity alone is not a reliable indicator of long-term chemical stability. A closely related parallel-configuration version, employing the same division scheme, was produced as well.

Ultimately, leakage in the newly designed cells (Figure 10B) proved even more severe than in the first design (Figure 10A), regardless of the gasket material. Consequently, we discontinued this line of development.

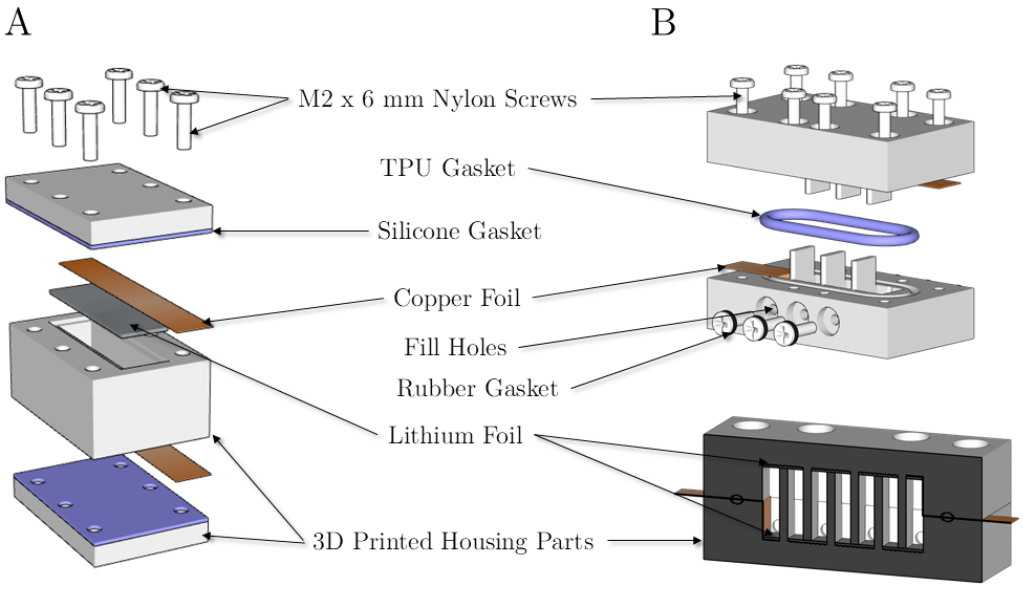


Figure 10: First cell design for early imaging experiments (A) and later design, intended to study dendritic growth in a seven-compartment series configuration design (B). The figure shows an exploded (upper) and cross-section (lower) view of the cell.

The next generation pursued a cup-like housing intended to stop electrolyte from escaping (Figure 11). The body features insertable electrodes and is closed with a top cover secured at first by nylon screws (Figure 11A), later by a threaded cap, wrapped with a few turns of polytetrafluoroethylene (PTFE) tape (Figure 11B). The introduction of the screw-on lid meant that the way we introduced the copper current collector had to be changed. A narrow gap, deliberately left in the side-wall, allowed us to insert copper foil and then fill the gap with liquid resin, which was photopolymerised in place, forming a seal around the copper electrodes.

Although several experiments were completed successfully, the design ultimately reproduced the same failure mode: during galvanostatic periods the pressure spikes created by gas evolution still exceeded the strength of the seal. Once even a pin-hole opened, the interior was exposed to ambient moisture; part of the electrolyte evaporated, part reacted chemically, and a sizeable fraction was simply pushed out of the cell by the internal over-pressure. Displacement of the liquid phase was visible in the in-situ MRI images and was confirmed by observation after the experiment the wet areas that formed around the sealing surfaces.

Because continuous SEI formation generates gas no matter what, the interior depth of the cup was increased; by filling the cell only partly we created a small pocket that remained occupied by inert argon and acted as a compressible head-space. We also added a second sealing stage; a TPU O-ring compressed between two profiled plates as the lid was tightened.

Under some conditions these measures preserved integrity, yet a new phenomenon appeared: the meniscus between liquid and argon became visibly distorted, with electrolyte creeping up one of the lithium foils. The behaviour is consistent with the electro-capillary effect: by the Young–Lippmann relation the charged metal lowers the local contact angle, the surface tension γ_S drops, and the meniscus climbs the conductor [118].

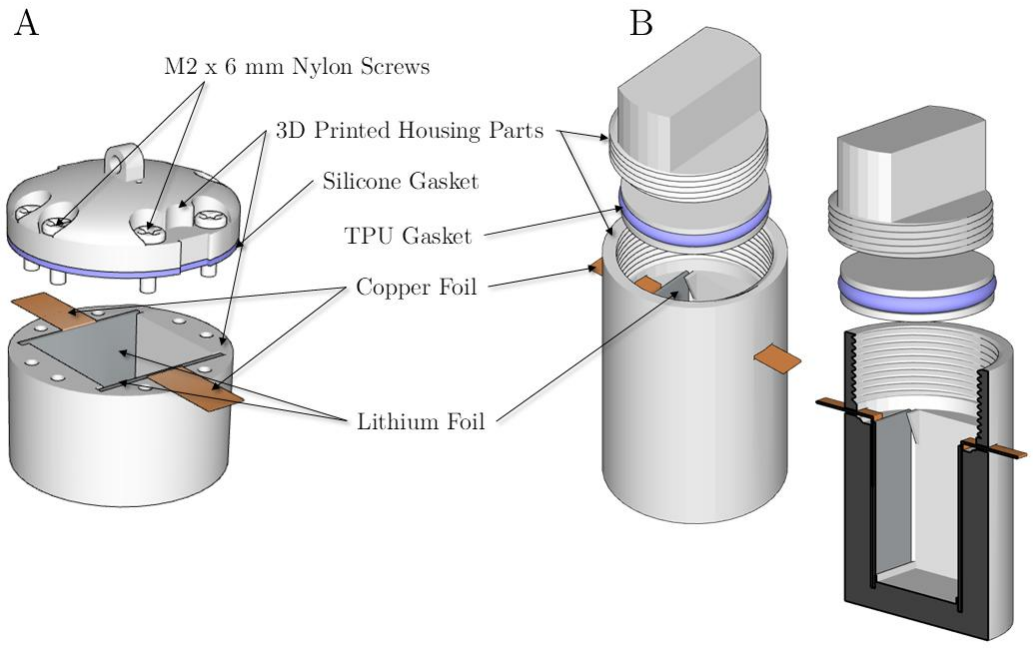


Figure 11: First cup-type cell design (A) and a later evolution of the cell (B).

Our latest iteration therefore circles back to the original prismatic layout, but with three critical changes (Figure 12). First, the gasket is now cut from PTFE, whose chemical inertness toward battery-grade carbonate electrolytes is well documented [119]. Second, the housing plates are clamped with brass screws and nuts; the higher allowable preload compared with nylon fasteners greatly stiffens the joint and suppresses pressure-induced bowing. Third, the fill port is sealed by a microporous expanded-polytetrafluoroethylene (ePTFE) membrane that acts as a one-way vent, permitting gaseous by-products to escape while blocking liquid [120]. Although extended testing is still in progress, this combination has yielded the most stable imaging phantom we have built to date.

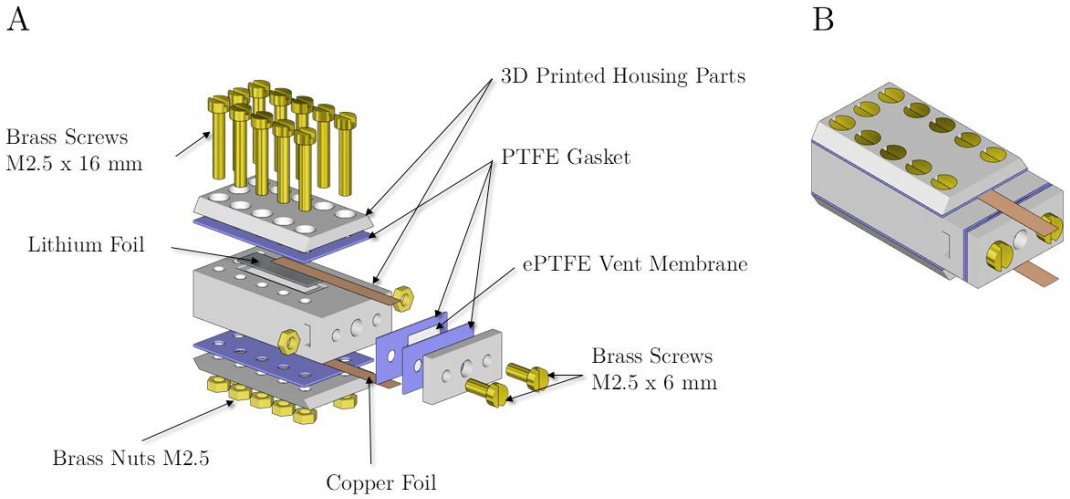


Figure 12: Latest development of the imaging cell, as per time of writing. This design features brass fasteners, PTFE gaskets and a hydrophobic ePTFE vent membrane. The cell is shown in an (A) exploded and (B) assembled view.

3.2.7 Studies

3.2.7.1 Cell Configuration

The cells used in the configuration study were based on the previously described cup-style design featuring a threaded top lid. The housing features slits for 16 x 10 x 0.3 mm lithium electrodes to be inserted. Three distinct cell configurations were investigated: a four-compartment parallel configuration, a four-compartment series configuration, and a single-cell setup serving as a reference (Figure 13). The electrode distance is 16 mm in the single cell and parallel designs, while the thickness of each compartment in the series configuration was about 3.8 mm. The parallel design incorporates vertical walls embedded directly into the cell housing, functioning as physical barriers to ion motion and effectively dividing the internal space into four parallel compartments upon assembly. Conversely, the series configuration employs five evenly spaced slits within the housing, designed for the insertion of lithium plates. This arrangement creates four compartments electrically connected in series. In both multi-compartment designs, the individual compartments are not fully isolated, although convection-driven electrolyte mixing between compartments is presumed minimal.

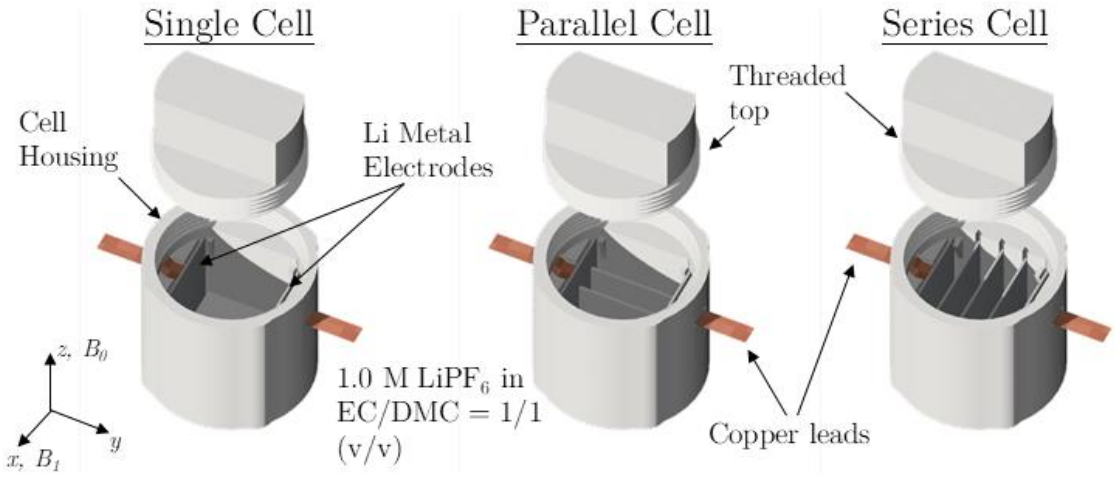


Figure 13: Cell assemblies for the cell configuration study and their orientations in the MRI magnet relative to B_0 and B_1.

Dendrite growth began concurrently with the start of ^{1}H MRI image acquisition, maintaining a constant charging current of 1 mA ($j \approx 0.66$ mA cm^{-2}) throughout the experiment, with an upper voltage limit of 4.0 V. Each image acquisition lasted approximately 2 h and 20 min, followed by a 1 h pause before starting the next image acquisition. In total, for each battery configuration (single cell, cells in parallel, cells in series), 20 sequential images were acquired, which corresponded to 67 h of experiment time.

3.2.7.2 Polarity Reversal

For the full-cycle experiment, the cell depicted on Figure 11B was used. The orientation of the cell in the magnet was the same as in the cell configuration study (electrode normal perpendicular to B_0, and B_1).

The cell was filled with 2 mL of electrolyte, to a height of about 8 mm, leaving some head space for the gases released from the electrolyte. The cell was operated in CC mode with the galvanostat in constant current (CC) mode with 1.5 mA of current in both

directions, yielding a current density of about $j \approx 1.2$ mA/cm^2. The polarity was reversed after 20 h of experiment time.

3.2.8 Image Processing Methods

In this study, the imaging process involved several stages to convert and process data for analysis. Initially, images were captured using the TNMR imaging software and saved in the proprietary `.tnt` file format. A custom macro was employed within ImageJ to automate the process: each image was opened, and every slice was exported as a `.dat` file, representing a matrix of image values. Subsequently, these `.dat` files were imported into a Python environment using the open-source Spyder integrated development environment (IDE). Within Python, the image sequences were organized and manipulated as four-dimensional NumPy arrays with dimensions corresponding to time (t), and spatial coordinates (x, y, z), enabling comprehensive analysis of the imaging data.

The initial step in the image analysis involved identifying an intensity threshold to differentiate dendritic regions from areas consisting solely of electrolyte. This determination was conducted through an image histogram analysis, which began with computing histograms for every image in the sequence. The histogram of the baseline (first) image was then subtracted from each subsequent histogram, generating 'difference histograms'. These difference histograms were scrutinized to pinpoint a transition zone characterized by an increase in low-intensity voxel counts and a corresponding decrease in high-intensity voxel counts, indicative of the threshold intensity value. Once this threshold intensity was established for each image, an inverted thresholding procedure was applied, assigning a voxel value of 1 to intensities below the threshold and a voxel value of 0 to intensities above it. Finally, these binary masks underwent filtering by connected components (small volumes, not connected to the electrode/deposit via any of direct six neighbours were deleted) as well as manual refinement to eliminate artefacts arising from gas bubbles or other imaging anomalies. Connective-component filtering was manually screened, to prevent potential loss of disconnected “dead” lithium. Counting all voxels in the final mask yields apparent dendrite volume $V_{apparent}$.

Because each voxel usually contains a mixture of electrolyte and metal, the mask overestimates the true metal volume. Therefore, a calibration factor $f(t)$ is introduced that represents the mean lithium filling fraction of the dendritic voxels at a given time-point.

$$f \;=\; \sum V_{electrolysis} / \sum V_{apparent}, \tag{3.3}$$

where

$$V_{electrolysis} = \frac{Q(t) M_{Li}}{z F \rho_{Li}}, \tag{3.4}$$

is the lithium volume predicted from the cumulative charge $Q(t) = I \cdot t$ (with $z = 1$ and ρ_{Li} the metal density). The corrected dendrite volume ($V_{dendrite}$) for any individual cell then follows as

$$V_{dendrite} = f \cdot V_{apparent}, \tag{3.5}$$

This allows us to convert MRI signal voids into a time-resolved, quantitative measure of the lithium metal that has plated in each image.

3.3 Results

3.3.1 Cell Configuration Study

Figure 14 (Columns A, C, E) presents sequential three-dimensional magnetic resonance (MR) images illustrating dendritic development in symmetric lithium-metal cells over time. Each column corresponds to one of the tested configurations: a single cell, four parallel cells, or four series-connected cells. In all cases, a 1 mA constant current is supplied. In these MR images, the bright regions represent the proton-rich electrolyte, whereas the darker, branched regions indicate the formation of dendrites at the lithium anodes.

Dendrites initially appear as relatively dense "mossy" deposits and gradually transition into more branched structures as the experiment continues. Gas voids (small dark circular spots) sporadically emerge near the anode.

When four identical cells are connected in parallel (Figure 14C), they each share the same electrical potential but can carry different currents. This results in uneven dendritic growth across the four compartments. One cell may exhibit a dominant, "runaway" dendrite expansion if it has a locally lower resistance, diverting more current and thus plating lithium more quickly. Gas pockets also form, but these largely remain small and confined within each individual cell compartment.

All four cells in series (Figure 14E) carry the same current, leading to a relatively uniform rate of dendrite growth across all cells. Most cells begin to show dendritic structures nearly simultaneously, and they reach the opposing electrode around the same time (after about 28 hours). Fewer large gas voids are present, and when they occur, they do not appear to significantly alter the growth pattern among different series-connected cells.

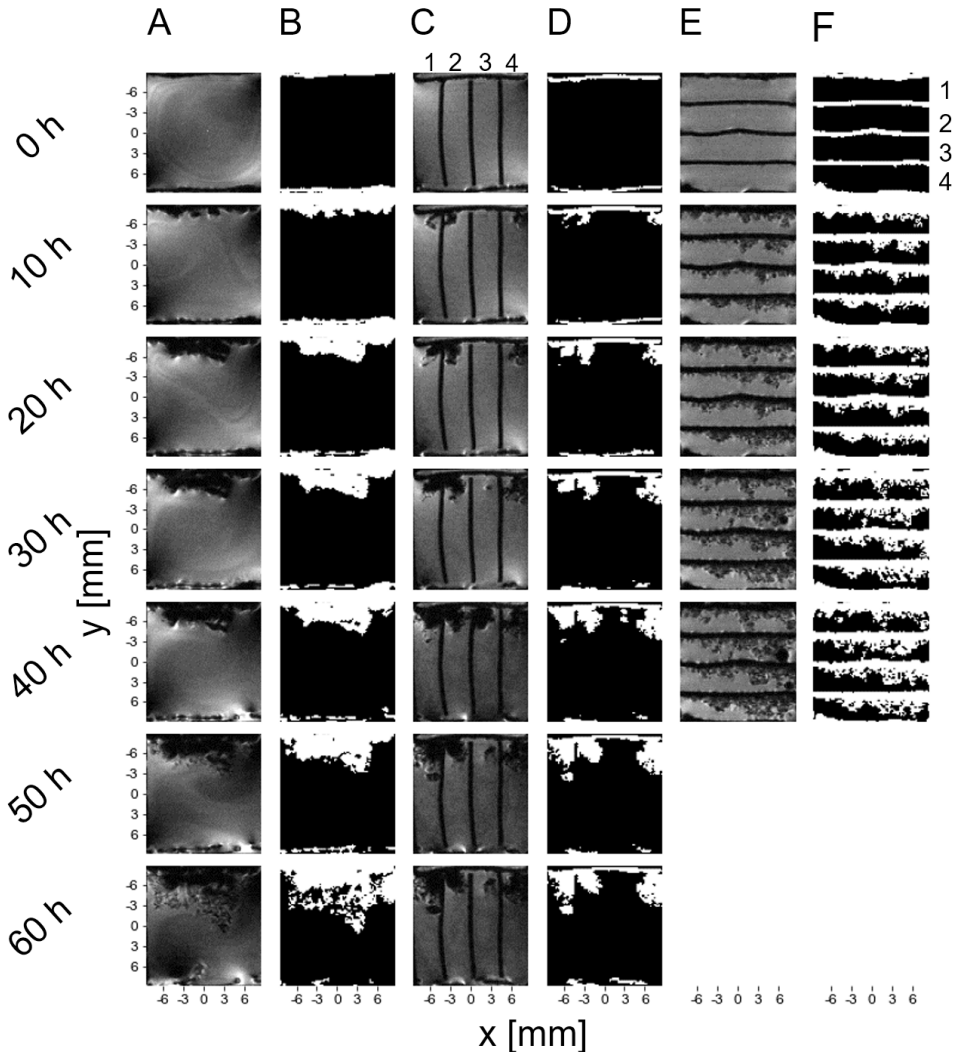


Figure 14: Dendritic growth imaging and segmentation. This composite figure displays two sets of panels for each battery configuration. The panels (A, C, E) show conventional 3D MR images where the bright areas represent the electrolyte and the dark, branched regions indicate dendritic deposits. The panels (B, D, F) present binary images derived by applying a threshold; here, the dendritic regions and electrodes are highlighted in contrast to the background. The figure contrasts three setups; a single cell, cells connected in parallel, and cells connected in series, illustrating how configuration impacts dendrite morphology and uniformity.

To quantify dendrite formation, the MR images were processed via a thresholding technique (shown in Figure 14, columns B, D, F). After establishing a suitable intensity threshold from the overall brightness distribution, voxels beneath the threshold were classified as "dendritic" or electrode-containing regions.

By comparing the intensity histograms (Figure 15) at each time point against a baseline (the first image), one can pinpoint the growing "low-intensity" region attributed to dendrites. A clear threshold near an intensity value of about 50 separates the bright electrolyte signal from darker dendritic regions.

Summing the voxel volumes labelled as dendrites gives an "apparent dendrite volume," $V_{apparent}$. When normalized to the electrode's surface area, $S_{electrode}$, we obtain a time-evolving trend of dendrite accumulation.

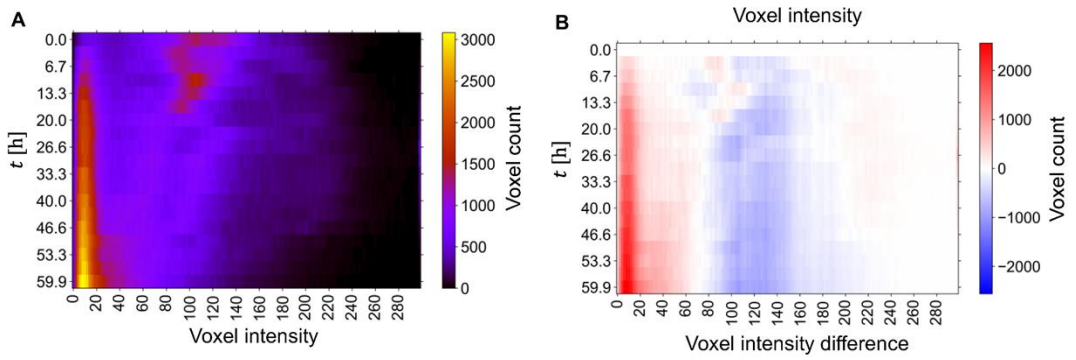


Figure 15: Temporal histogram analysis for threshold determination (single-cell configuration). This figure comprises two color-coded panels. Panel A is a stacked display of intensity histograms taken at successive time points; each row corresponds to a distinct moment in the experiment and shows the shift from a predominantly electrolyte signal to a growing population of low-intensity (dendritic) voxels. Panel B shows the difference between each histogram and the baseline, with a clear transition region (around an intensity value of 50) identified as the optimal threshold for segmenting dendritic structures from the electrolyte background.

Figure 16 plots $V_{apparent}/S_{electrode}$ over time for the single-cell reference (blue circles) as well as each cell in the parallel (panel A) and series (panel B) configurations. Key observations are:

Single cell: Dendrite growth displays a sigmoidal trend. It rapidly increases over the first ~19 hours, slows briefly, and then accelerates again around the 40-hour mark.

Cells in parallel: Growth rates vary noticeably among the four cells. One cell, in particular, may show minimal deposition, while another may experience much faster dendrite formation. On average, however, the overall rate (red triangles) keeps pace with the single-cell trend.

Cells in series: All four cells grow dendrites more uniformly, at least until the deposits begin to reach the opposite electrodes. Notably, after ~28 hours, the dendrites in multiple cells short-circuited the gap, so data at later time points are not shown for those cells.

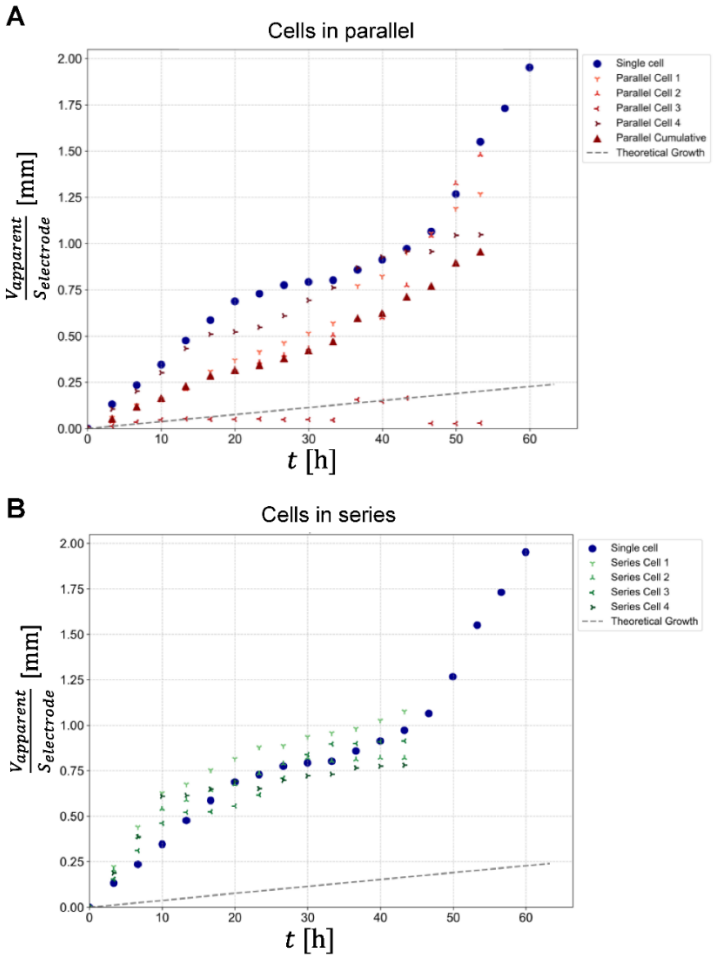


Figure 16: Apparent dendrite volume vs. time. This graph plots the evolution of the "apparent" dendritic volume (the sum of all voxels classified as dendritic) normalized by the electrode surface area over the charging period. Different symbols represent data from individual cells within each configuration (single, parallel, and series). The curves illustrate a non-linear, sigmoidal increase in a single cell, variable rates among parallel cells, with one cell even showing minimal growth, and a generally uniform trend for cells in series. A dashed line marks the theoretical deposition volume predicted by Faraday's law, providing a reference for comparison.

Applying the aforementioned thresholding onto the images allows us to reconstruct a "dendrite-density" map (Figure 17), with bright values likely corresponding to denser structures, while dimmer areas represent less sense, highly dendritic growth. The time-lapse of the example slice of the electrodeposition plating for the single-cell experiment (Figure 17) shows clear distinction between the bright, dense, "mossy" growth (up to 43.3 h) and less-dense, likely dendritic formation from 43.3 h to 63.3 h.

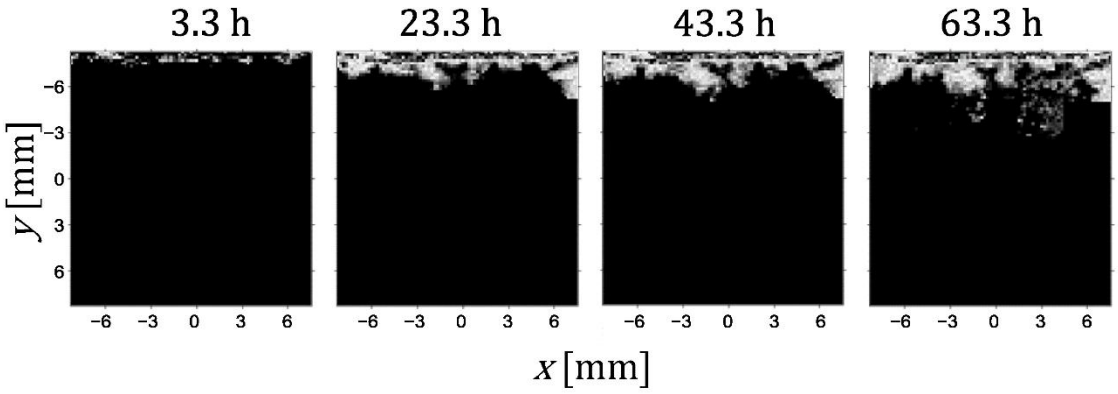


Figure 17: Time-Lapse of anode plating (single-cell experiment). This series of processed MR images captures a representative slice of a single cell at multiple time intervals (3.3 h, 23.3 h, 43.3 h, and 63.3 h). The images are produced by subtracting the baseline, normalizing to the average intensity of the electrolyte, and applying a masking technique to emphasize dendritic regions.

A direct comparison of $V_{apparent}$ with the theoretical volume of metallic lithium predicted by Faraday's law of electrolysis showed that the measured "apparent" volume far exceeds the actual deposited Li. This gap stems from partial filling of each voxel and magnetic-susceptibility or radio-frequency (RF) shielding effects. By assuming a uniform filling fraction f for all dendritic voxels at a given time point, one can more closely match the theoretical plating volume. Using the factor from (3.5, Figure 18 displays dendrite volumes (solid symbols) that generally align with theoretical expectations. The series cells clearly show more consistency, confirming a more even plating process.

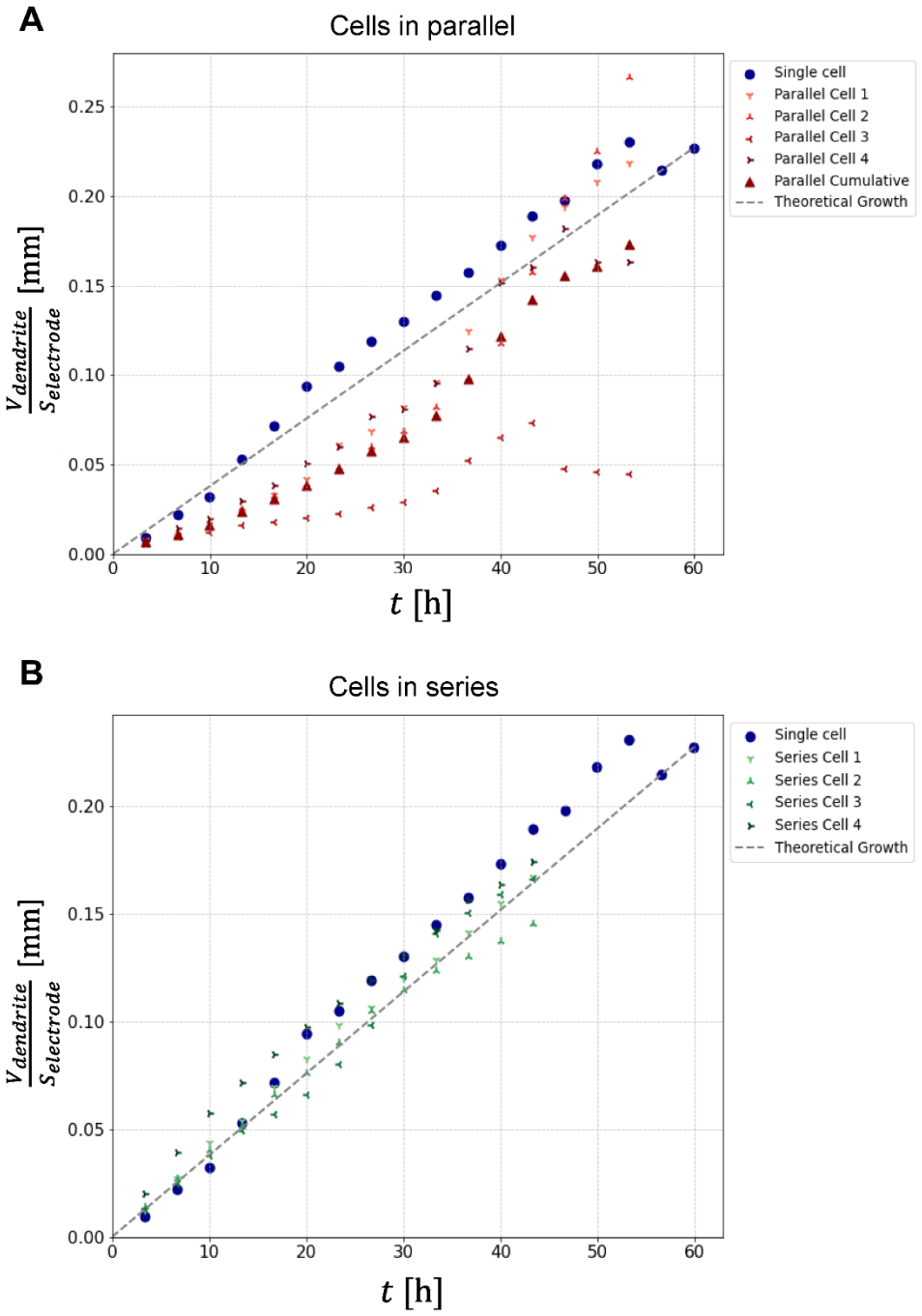


Figure 18: Calibrated dendrite volume (Corrected for Filling Fraction). In this figure, the initially measured dendritic volumes are corrected using a lithium filling fraction to yield a more accurate representation of the deposited lithium. The adjusted volumes (normalized by the electrode surface area) are plotted over time and against the theoretical growth for (A) parallel and (B) series configuration.

Because MRI measures signal from the electrolyte protons (^{1}H), dendrites manifest as regions of diminished (or zero) signal intensity. However, additional signal deficits arise from physical displacement of electrolyte, leaving less liquid in the voxel, and susceptibility and RF shielding. Metal deposits distort local magnetic fields and reduce effective RF penetration. To estimate realistic values of actual volume, taken up by the dendrites, a

filling fraction f is determined. This fraction changes as the deposition progresses, and allows to track the density progression of the growth. As shown in Figure 19, which shows the signal and filling fraction averaged across all experiments, dendrites with a smaller filling fraction f cause less MR signal drop, whereas more densely plated voxels exhibit near-complete signal loss. Both the overall fraction f and the average normalized signal from dendritic voxels gradually stabilize after around 40 hours, suggesting that later-growth dendrites become progressively less dense, also causing less signal loss.

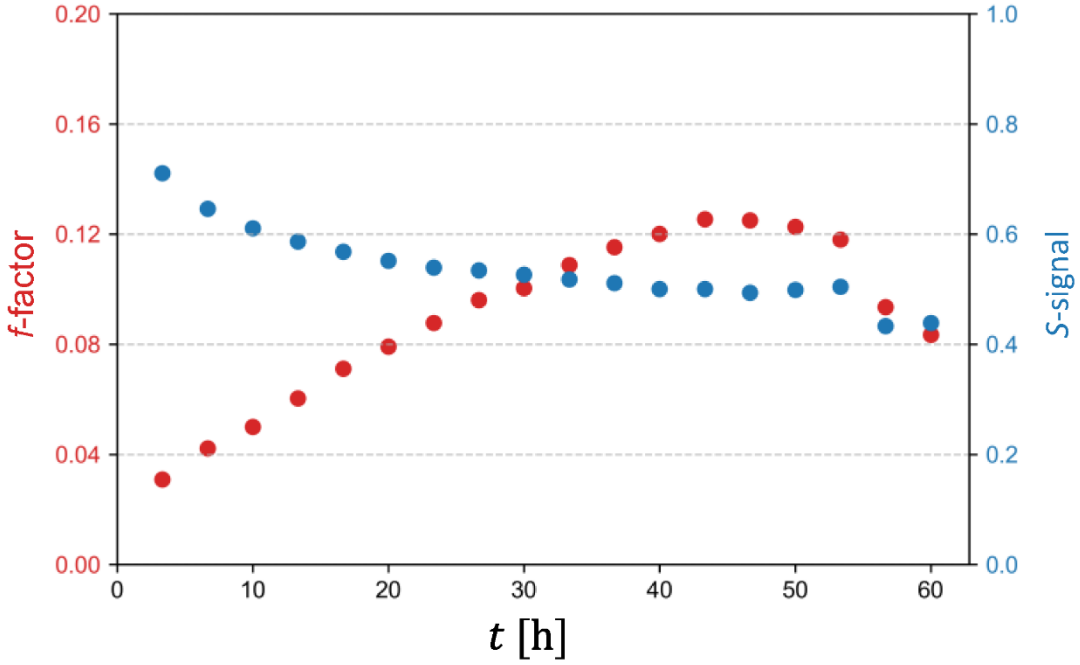


Figure 19: Relationship between voxel filling factor and MR Signal. This graph illustrates how the dendritic voxel filling fraction (a measure of the fraction of each voxel occupied by lithium) and the normalized MR signal evolve over time.

3.3.2 Polarity Reversal Study

Figure 20A shows a time-lapse of xz MRI slices at different y-positions (different slices in xz plane) over the duration of the experiment. During the first half-cycle (0–20 h, positive current), Electrode 1 (the anode in this phase) exhibits progressive dendrite formation, visible as dark "void" or branching regions encroaching into the electrolyte. Electrode 2 (the counter electrode) remains relatively featureless, with minimal deposit formation.

Once the polarity is reversed (20–40 h, negative current), new dendrites appear on Electrode 2, while the previously formed deposits on Electrode 1 begin to degrade. This behaviour is reflected in Figure 20B, which tracks the maximum deposit height along yz projections. As time progresses in the second half-cycle, Electrode 2's dendritic front height rises steadily, whereas Electrode 1's maximum height remains relatively unchanged.

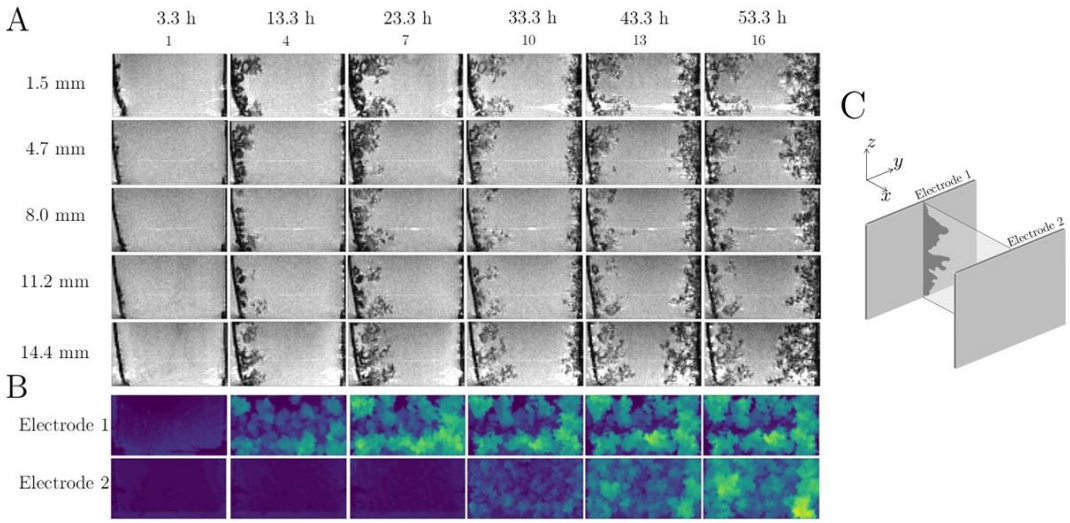


Figure 20: Time-lapse of xz MRI slices at various values of y (A) and yz projections of maximum mask height for both electrodes (B), reflecting a time-lapse of deposit growth in height on both electrodes (Electrode 1 refers to the anode of the first half-cycle). The orientation of the cell in the coordinate system is shown on panel C.

Figure 21 shows the intensity difference maps between successive images in the sequence, along with the corresponding MRI slice. Such a representation allows to track not only the growth (red areas) and dissolution (blue areas) of lithium but also movement and deformation of existing growth. At 30.0 h and 33.3 h, on the first electrode, where lithium is oxidized, clear movement of a large dendrite structure is visible.

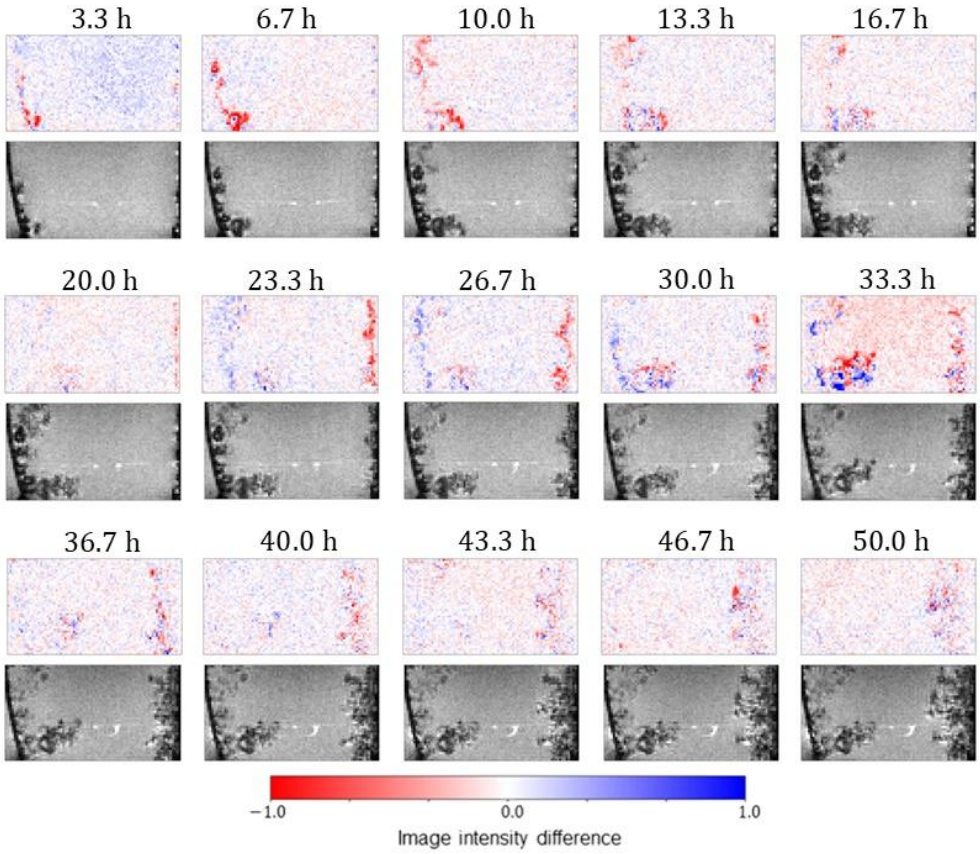


Figure 21: Voxel intensity differences between each sequential image, along with MR images (shown for xz slices at $y = 9.3$ mm). Red represents a decrease in image intensity, while blue indicates image intensity increase relative to the voxel at same location but at the previous timepoint. Areas of decreasing intensity corresponds to dendrite growth, while areas of increasing intensity indicate dissolution of dendrites.

In Figure 22A, the binary-mask volumes for each electrode are plotted over time. During the first 20 h, the mask volume for Electrode 1 (blue curve) grows from near zero to a peak, while Electrode 2 (red) stays negligible. Immediately after the polarity switch, Electrode 1's volume drops (dissolution), and Electrode 2's volume begins a near-linear increase before slightly levelling off toward the end of the experiment.

Figure 22B highlights the average deposit density (analogous to a filling fraction, f). The theoretical electrolysis volume was divided by the volumes of new growth in each image (number of new voxels multiplied by voxel volume). Electrode 1 starts around 0.10–0.12 g/cm^3 and gradually declines to ~0.04 g/cm^3 by the end of its plating phase. In the second half-cycle, Electrode 2 briefly spikes to ~0.45 g/cm^3 immediately after polarity reversal—likely a short-lived, high-density plating or segmentation artefact—then converges to more moderate values (~0.05–0.10 g/cm^3). Both electrodes thus tend to stabilize around relatively low average densities once their dendritic films have grown for several hours.

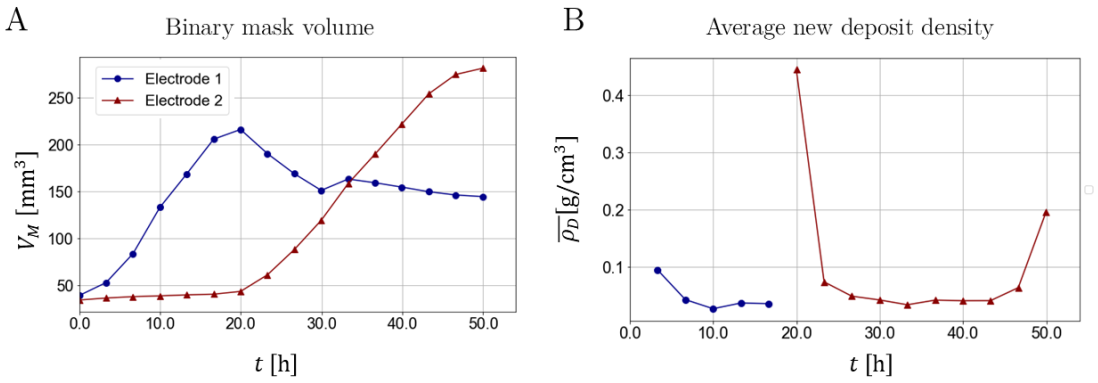


Figure 22: Volumes of the binary masks of the anodes for both half-cycles (A) and average density (B, Analogous to filling fraction f, (3.3) of new deposits. Blue and Red curves represent both electrodes, respectively. Electrode 1 was the anode for the first half-cycle and Electrode 2 for the second.

Figure 23A shows tip growth rate maps, where positive (red) regions mark outward dendrite growth and negative (blue) regions indicate dissolution or shrinkage. During the first half-cycle, Electrode 1's growth rates remain predominantly positive, whereas Electrode 2's are near zero. After the 20 h mark, the situation reverses: Electrode 1's growth rate turns negative (blue), confirming dendrite retreat, and Electrode 2 exhibits positive growth.

Figure 23B plots the maximum and average front heights for both electrodes. In the first half-cycle, Electrode 1's maximum front height increases steadily from 0 to ~5 mm; after reversal, that height declines only very slightly. By contrast, Electrode 2 transitions from near-zero heights to a comparably growing front, reaching up to ~5 mm by the end of the experiment.

Lastly, Figure 23C shows the cell potential over time. The voltage transitions from ~+0.3 V and declines to +0.16 V during the first phase. Upon reversing the current at 20 h, the potential flips sign (near −0.16 V), undergoes a spike (−0.38 V) before settling at around −0.18 V. A minor transient at ~30 h does not appear to correlate with major morphological changes in the MR images or the volumetric data.

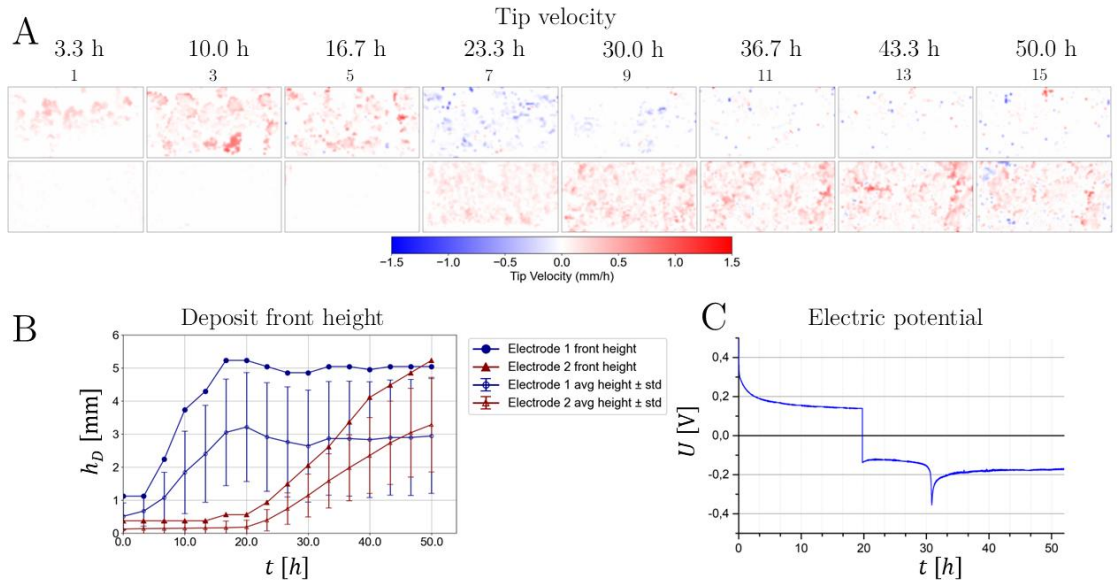


Figure 23: yz projections of growth rates of the growing deposits for both electrodes (each row corresponds to a different electrode) at various time points (A), maximum and average front height of the deposits (error bars represent the standard deviation from the average) for both electrodes (B) and electric potential during the experiment (C).

3.4 Discussion

3.4.1 Cell Configuration Study

Indirect 1H MRI of the electrolyte has proven to be an effective method for visualizing the evolution of dendritic structures on the lithium anode. The acquired MR images reveal dark, branching features that correspond with the progressive development of lithium deposits. Initially, the dendrites appear as dense, moss-like layers; as charging proceeds, these deposits evolve into more intricate, branched morphologies. This progression aligns with theoretical predictions based on electrolyte concentration gradients and local overpotential effects, as described in Sand's model and further elaborated by Chazalviel [14].

Sand's model (sometimes referred to in the context of "Sand's time") describes when the electrolyte adjacent to the electrode becomes fully depleted of ions during constant-current plating. Once the local ion concentration hits zero at the interface, electrodeposition becomes diffusion limited and dendritic growth typically ensues. The current at (or above) which this depletion occurs is often called the "critical" (or "limiting") current density. The Sand's time (t_s) for a binary electrolyte is defined via:

$$t_S = \frac{\pi D_{Li}(zFc)^2}{4(jt_a)^2}. \tag{3.6}$$

For a diffusivity D_{Li} of $2 \cdot 10^{-10}$ m^2/s, a current density of $j = 0.66$ mA cm^{-2} and anion transference number (t_a) of 0.62, the estimated sand's time amounts to approximately 15 hours, which should be resolvable in the scope of our experiment. It must be emphasised, that this model is highly idealistic and overlooks many critical phenomena, thus significant deviations from the predictions are expected in real-world conditions. Sand's model assumes that diffusion occurs in a one-dimensional manner across a flat, homogeneous electrode surface. In practical systems, electrodes often have non-uniform surfaces with microstructures or defects, leading to localized variations in ion concentration and deviations from the predicted one-dimensional profile. Unlike in real cells, where even slight temperature gradients can induce natural convection, the Sand's model assumes purely diffusion-driven transport. Furthermore, factors such as changes in viscosity, ion pairing, and interactions with the electrode surface (e.g., SEI formation) can alter electrolyte properties, which are assumed constant in the model. The model also presumes a constant current density with an immediate and uniform reaction at the electrode surface. However, real electrochemical reactions can exhibit complex kinetics, with localized overpotentials and transient phenomena that are not captured in this idealized model.

Predicting the precise onset and location of the transition from mossy to dendritic growth in lithium-metal cells is challenging due to several interrelated factors. Small surface imperfections on the lithium anode can create localized "hot spots" where current density is amplified, initiating protrusion growth that subsequently distorts the local electric field and ion concentration. This feedback mechanism results in a highly nonlinear and dynamic process that is sensitive to even minute variations in electrode roughness [14]. Furthermore, lateral ion diffusion in the electrolyte causes non-uniform concentration gradients, especially in complex cell geometries, making it difficult to predict when the depletion at a particular site will trigger rapid dendritic branching [121]. Mechanical stresses arising from volumetric changes during lithium deposition and stripping add another layer of complexity; these stresses can either promote or inhibit localized growth depending on whether they are tensile or compressive, as described by Monroe and Newman [5].

Additionally, the formation and evolution of the solid–electrolyte interphase (SEI) alter local overpotentials and reaction kinetics, further complicating predictions [122].

Inspecting the MRI images (Figure 14, columns A, C, E) reveals that there are two distinct morphologies, that are observable; dense growth, that progresses slowly and produces areas of more pronounced signal shielding, compared to the dendritic growth, which on MR images appears to be slightly brighter and much more branched, but most importantly, exhibits much faster growth compared to mossy deposits. For example, this can be clearly seen in Figure 14A, where up to 50 h, the deposits are dense and there is little progression in the height of the deposits, but after 50 h, there is suddenly growth, that spans halfway into the cell.

Interestingly, in the parallel configuration, the regime of mainly dendritic growth is never reached, while in the series experiment, the growth appears to be dendritic almost from the beginning. As explained, the times of growth phase transition are very difficult to predict in real cells. Incidentally, the apparent transition times may exhibit significant variance even in seemingly identical operating conditions. Due to the inhomogeneous nature of electrodeposition, it might even be possible that two growth peaks at different positions in the cell might simultaneously grow in different regimes.

In these experiments on parallel cell configurations divided into multiple compartments, the results do not quite align with the hypothesis. One would expect more growth of the dendritic kind, compared to the simple cell design. This is due to two main reasons: uneven current distribution and limited lateral ion conduction. In a parallel circuit, each compartment's net current is dictated by its local impedance. Even slight differences (e.g., a slightly lower interfacial resistance) can lead one compartment to draw disproportionately higher current. Once a particular compartment experiences higher current, local ion depletion can set in more readily, driving the formation of dendrites. Secondly, because the walls prevent ion exchange between compartments, each region has only its own local electrolyte supply. If a compartment begins drawing high current, it cannot "pull" ions from its neighbours, so it may deplete quickly. This local depletion amplifies the overpotential at emerging protrusions, accelerating tip-controlled dendritic growth in that specific region. When comparing the results of the "simple" and "parallel" experiments (Figure 14, columns A, C), although not significantly, the onset of dendritic growth is indeed earlier in the parallel experiment. This can be more clearly interpreted from the graph of the dendrite mask growth (Figure 16A). With the onset of dendritic growth, the volume of the binary mask increases at a steeper rate. In the parallel experiment, this soft transition occurs after approximately 30 – 40 h of experiment time, while this transition in the curve for the simple cell binary mask takes place sometime after 40 – 50 h.

Inspecting the series configuration experiment, it appears that the growth is more or less dendritic from the onset of plating. With the electrode areas and therefore current densities between the simple and series cases is identical, the only significant difference is the electrode spacing. Each compartment in the series cell has $1/4^{\text{th}}$ of the inter-electrode distance of the simple cell design. A shorter gap between the electrodes means ions travel a shorter distance, so the local concentration gradient (and associated overpotential) can become steeper at the electrode surface. By contrast, a wider gap gives the ions more volume to diffuse through before reaching the electrode, generally moderating concentration gradients. In the case of a smaller electrode spacing, the same current density must be supported over a smaller interelectrode distance, so local lithium-ion depletion happens more quickly, raising the possibility of earlier dendritic (tip-controlled) growth. Secondly, with a shorter path, any minor surface irregularity could more rapidly amplify local current densities at deposit tips, resulting in branching filaments instead of a uniform or mossy layer. Conversely, larger electrode spacings spread the same current density over a deeper electrolyte region, potentially reducing how quickly depletion zones form and

keeping the overall system in a mossy or more uniform deposition regime for longer. Consequently, if different compartments in a multi-electrode cell have slightly different electrode separations (due to assembly tolerances or design variations), you may see one region transition to a dendritic regime sooner than the others. This effect is particularly noticeable under higher current densities, where small differences in geometry and spacing can generate large differences in local ion concentration gradients and, therefore, in the regime of lithium plating.

Moving on from the investigation of growth regimes in different cells, the comparison of per-compartment deposits shows clear distinctions between parallel and series configurations. In the parallel configuration, the calibrated dendrite volume (Figure 18A) as well as direct observation of MRI images (Figure 14C) show that one department exhibits little to no growth. In the later stages, (after 40 h) the spread between the amount of deposits per compartment further increases. This is in line with the already mentioned predictions. Since the current density distribution is limited per compartment, it is more likely that one compartment experiences a slightly higher deposition rate than others, leading to self-accelerated growth. On the other hand. the uniform dendritic growth observed in series-connected cells suggests the presence of self-regulatory mechanisms that help prevent runaway deposition. The initial hypothesis predicted, that if any compartment contains taller dendrites, the ohmic resistance of the compartment drops, thus causing a lower overpotential for that compartment relative to others, slowing dendrite growth. However, it seems that electrolyte resistance presents only a small part of the overall cell impedance. The key resistance in such a system arises typically not from the bulk electrolyte but from the interfaces. The double layer and SEI introduce significant kinetic barriers that determine the effective overpotential for deposition. Therefore, while a local decrease in ohmic resistance may occur where dendrites grow taller, it does not translate to a proportional decrease in the overall overpotential because the kinetics of lithium ion reduction (and side reactions) at the electrode surface dominate. Therefore, the uniform amount of deposits in each compartment is likely a result of identical current densities across compartments. This finding is consistent with the framework proposed by Monroe and Newman [5], which emphasizes the importance of delivering an equal current to all cells. These observations support diffusion-limited deposition models that indicate controlled current distribution is critical for achieving homogeneous lithium deposition [121].

A significant challenge in quantifying lithium deposition is reconciling the theoretically predicted lithium volume with the “apparent” dendrite volume derived from MR images. The apparent volume is often larger due to partial voxel filling and signal attenuation effects resulting from magnetic susceptibility and RF shielding. This discrepancy has been noted in studies using FLASH imaging sequences [10]; although our use of a RARE sequence reduces these effects, careful calibration remains essential. Moreover, the observed non-linear growth patterns indicate the existence of multiple growth regimes, likely reflecting a transition from dense, uniform deposition at lower current densities to more branched structures when the diffusion-limited regime is reached.

Electrolyte stability also emerges as a critical factor. Even with rigorous control of moisture, trace impurities in $LiPF_6$-based electrolytes can lead to localized degradation, influencing dendritic growth dynamics. Reviews by Piglowska et al. [123] and Yang et al. [124] highlight the necessity for stringent electrolyte composition and cell sealing to mitigate such effects.

In summary, our observations underscore the critical roles of uniform current distribution, local ion concentration gradients, and electrolyte stability in dictating dendritic growth morphology. The integration of advanced 1H MRI techniques with quantitative volumetric and density analyses not only corroborates existing theoretical

models, including those by Chazalviel (1990) and Monroe and Newman (2005), but also lays the groundwork for improved strategies to suppress dendrite formation, ultimately enhancing the safety and performance of lithium metal batteries.

3.4.2 Polarity Reversal Study

These results demonstrate how polarity reversal affects the onset of dendritic growth. During the first stage, dendrites grow as expected. Similarly to the cell configuration study, the growth starts out as denser, moss-like deposits and quickly transitions into dendritic growth. The estimated Sand's time for this cell is around 4.7 h, thus transition to the dendritic regime is to be expected earlier than in the cell configuration experiments. A qualitative analysis of MRI images indicates that this is indeed the case. The volume of the binary mask shows a steep rise between images 3 and 4, indicating that dendritic regime of growth is already active after approximately 10 hours of experiment time (Figure 22A). After reversal, the dendritic growth is very similar that in the first stage, although the slope of the dendrite mask volume growth is slightly less steep. As per image observations showing dendritic growth in the first stage, as well as estimated Sand's time for ion depletion at electrode surface, it is reasonable to expect a strong concentration gradient would have formed across the cell by the time of polarity reversal. Interestingly, however, if such a gradient exists, the experimental observations indicate, that it seems to play little role in the second part of the deposition process (reversed polarity). An abundance of Li^+ ions should near the surface of the anode should, in theory, result in a more even deposition, however, this is not evident from the results.

The deposit fill fractions, i.e. mean dendrite density graph (Figure 22B) shows that in the second stage, the estimated density of newly deposited lithium in the first recorded image after polarity reversal shows a significantly higher density compared to the beginning of the first phase of deposition (~0.45 g/cm^3 vs ~0.1 g/cm^3). It should be emphasised, that in order for a direct comparison of initial densities in respective phases to be possible, the first image should have been recorded under open-circuit (OC) conditions. This is because the densities are estimated based on differences in dendrite mask volumes between successive images. Since dendrites were growing from the beginning of the experiment, the first estimations for deposit density can be made for the interval between the first and second image, while the last image in the first phase of the experiment serves as the "zeroth" image for the second phase.

In both polarities, a higher initial density is in line with the observations, that dense, mossy growth occurs in the first few hours of deposition, as base-controlled, nucleation limited growth is dominant. In the later stages of both polarities, the densities seem to stabilize at around $0.03 - 0.05$ g/cm^3. Unfortunately, no existing results were found in the literature to validate these estimations.

Dendrite front growth rates (Figure 23) show, that dendrites in both phases grow with a rate of approximately 0.7-1.3 mm/h. Chazalviel established an idealized model, that predicts the tip growth rate based on the electric field in the bulk electrolyte and anion mobility (2.1). Given that the reported conductivity figures for the given electrolyte are around 10-12 mS/cm (Table 2), the electrode distance L is 15 mm and the current I is 1.5 mA, we can estimate the potential drop and thus the electric field in the bulk electrolyte is:

$$E = \frac{U_e}{L} = \frac{IR}{L} = \frac{I}{\sigma A} \sim 8 \text{ V m}^{-1}. \tag{3.7}$$

Given the known anion diffusion coefficient, and an assumed temperature of 25°C, one can calculate anion mobility via

$$\mu_a = \frac{qD_-}{k_B T} \tag{3.8}$$

The resulting anion mobility is $1.36 \cdot 10^{-8}$ $m^2V^{-1}s^{-1}$. Using (2.1, the calculated front growth rate is $1.1 \cdot 10^{-7}$ m/s, or 0.4 mm/h. Figure 23 shows that tip growth rates range from approximately 0.5 to 1.5 mm/h. The results of the experiment are in the same order of magnitude as the estimation of the model. Chazalviel's model assumes the growth of "dense-parallel" deposits which grow uniformly. In reality, this is rarely the case, as the growth of dendrites is heavily dependent on the local environment, which may vary significantly throughout the cell. The actual space-charge region in a real cell is unlikely even and is a result of a balancing act between electromigration and diffusion of ions, as well as convection flows and displacement due to formation of gasses during SEI formation.

Previous studies revealed that lithium dendrite dissolution is highly non-uniform and often incomplete, governed by the solid electrolyte interphase (SEI), ionic transport through that SEI, and local charge-transfer kinetics [125]. Early studies using in situ microscopy showed that stripping (electro-dissolution) of Li proceeds heterogeneously, with dendritic protrusions dissolving unevenly and the SEI on Li breaking and reforming during stripping [126]. Upon current reversal, freshly deposited high-surface-area Li (with a fragile, thin SEI) oxidizes first at relatively low overpotential. This initial dissolution of dendritic Li is only partial – as the "fresh" Li is consumed, some dendrite tips lose electronic contact or become encased in SEI, turning into electrically isolated "dead" lithium that does not fully dissolve [22]. Once the active dendritic Li is depleted, the dominant anodic reaction shifts to the bulk Li metal electrode. Lithium then preferentially dissolves from the underlying substrate or larger deposits that were previously beneath the dendrites, which is kinetically more difficult due to the more developed SEI on these regions [22]. Consequently, the cell voltage rises to a peak until new ionic pathways emerge: the stripping current concentrates at defects or gaps in the SEI, leading to pit formation in the Li surface [22], [127]. The creation of such pits (and the rupture of SEI in those areas) lowers the local charge-transfer resistance and causes the overpotential to drop as dissolution proceeds preferentially at those sites. Notably, the remaining dendritic framework is not completely removed by stripping – large portions of the Li deposits can persist as inactive residue (dark "dead" Li) [127]. Operando visualizations have confirmed that these residual Li structures often survive the stripping process, and subsequent plating tends to nucleate new dendrites at or near the same sites (e.g. within previously formed pits or around the residual Li), rather than yielding a pristine surface [127]. This cycle leads to cumulative morphological roughening: each dissolution step roughens already uneven regions and leaves behind SEI-covered Li remnants, which in turn act as seeds for further dendritic growth in later cycles. The SEI thus plays a dual role – it mediates ionic conduction needed for Li dissolution, but it can also shelter parts of the dendrite from electrochemical oxidation. A thicker or less permeable SEI on older deposits impedes Li^+ transport and raises the stripping overpotential, often causing Li to dissolve from adjacent more accessible (or less passivated) sites instead. It was identified this incomplete stripping is a major factor in lithium metal's low coulombic efficiency [22]. More recent studies have built on this understanding by leveraging controlled rest periods and advanced diagnostics. For instance, it has been shown that during open-circuit rest, portions of the SEI can slowly dissolve into the electrolyte, which partially "unlocks" isolated Li and allows some previously stranded dendritic Li to be re-oxidized upon the next charge cycle [128]. Nonetheless, even with such mitigation, a fraction of the dendritic Li often remains unutilized, indicating that the tips of dendrites or deep inside SEI-covered regions are especially resistant to dissolution.

The observation from works, studying dendrite dissolution in lithium metal cells are largely validated with our experiment. It is clear, that after polarity reversal, mainly fresh dendrites dissolve. Results indicate, that dendrite tips dissolve only for a limited period of time (~10 h after polarity reversal). After dissolution of freshly-deposited lithium, the deposit front height remains constant (Figure 23B) and growth rates converge towards zero (Figure 23A). After dendrite tips are dissolved, the preferential dissolution sites shift towards the bulk electrode, with the majority of deposits remaining largely undisturbed (Figure 21).

The recorded electric potential (Figure 23C) shows a minor difference in the magnitude right before and immediately after polarity reversal (~20 mV). Over time, each electrode surface accumulates surface films, including SEI, dendritic or mossy deposits, and sometimes by-products like Li_2O or LiF. Because these films do not vanish when the current direction changes, it is common to see tens of millivolts difference in steady-state potential after polarity reversal [129].

Electric potential also shows a significant spike in overpotential that converges back towards the "equilibrium" potential after a few hours. No significant changes in the morphology of growing deposits were observed, therefore it can be assumed that this spike is related to the process of lithium stripping. This would be in line with the above-mentioned findings of existing studies, which mention that voltage spikes are a result of the depletion of active lithium and the need for the formation of a new ionic path for lithium stripping, however, this remains only speculation. Significant displacement of a large chunk of deposit is observable in Figure 21 at the same time point as the spike occurs. This could mean that part of the deposit became electrically inactive.

3.5 Conclusion

Operando ^{1}H MRI proved to be a powerful, non-invasive method for visualizing lithium plating inside an otherwise opaque symmetric Li|Li cell. By imaging the proton-rich electrolyte rather than the metal itself, we achieved 3D resolutions on the order of a few hundreds of micrometres and, after applying a simple histogram-based threshold and connected-component filtering workflow, converted signal voids into quantitative dendrite volumes, front heights, and growth rate maps without ever opening the cell.

When identical sub-cells were wired in parallel, slight differences in initial resistance caused one compartment to hog most of the current, leading to a runaway dendritic growth and produced numerous large gas voids. In contrast, series-connected cells, which by Kirchhoff's laws all carry the same current, exhibited nearly synchronous dendrite advance and comparable volumes across all four compartments. A single-cell configuration fell between these extremes, showing the classic mossy-to-dendritic transition predicted by Sand's model (Sand's time $\approx$ 15 h at 1 mA) with dendrites reaching a height of approximately 8 mm.

Polarity reversal after 20 h supplied a direct test for "dead" lithium. Only the freshest, most recently deposited dendrites dissolved in the subsequent ~10 h, while the underlying deposits, preserved by an insulating SEI, remained intact. After the dissolution of latest dendrite tips, the dissolution locations shifted near the electrode surface. Tip growth rates stabilised at 0.7–1.3 mm h^{-1} in both half-cycles, and front-height profiles converged near 5 mm despite a transient over-potential spike immediately after reversal.

Despite these successes, several limitations must be acknowledged. The 187 µm spatial resolution and susceptibility artefacts still obscure the earliest nucleation events and fine-scale branching. The custom cell design distinguishes our symmetric cell from commercial pouch-cell architectures, potentially affecting growth rates.

Looking ahead, several complementary diagnostics could deepen the picture that operando ^{1}H MRI has sketched so far. Electrochemical-impedance spectroscopy (EIS) performed in parallel with imaging would supply frequency-resolved transport parameters; bulk ionic conductivity, charge-transfer resistance and SEI evolution in real time; fitting equivalent-circuit elements to the evolving spectra would let us assign the onset of mossy-to-dendritic growth to specific impedance signatures and separate purely geometric current redistribution from true kinetic changes. On the fluid-dynamics side, velocity-encoded MRI (phase-contrast or grid-tagging methods such as SPAMM/DENSE) could be applied to a thin electrolyte slice to visualise convection rolls that develop once large lithium protrusions displace liquid and set up natural-convection loops; the distortion of a tagged 2D magnetisation grid would directly reveal flow vectors and could be cross-correlated with the location of fast-growing branches. To probe chemical transport, diffusion-tensor imaging (DTI) of the proton signal offers a route to mapping anisotropic solvent self-diffusion; hence local viscosity or salt-concentration gradients, while simultaneous ^{7}Li chemical-shift or ^{7}Li MRI would give absolute Li^{+} concentrations throughout the electrolyte. Combining indirect 1H MRI with 7Li MRI would simultaneously visualise the evolving space-charge layer and growing deposits, although ^{7}Li MRI suffers from low sensitivity, modern cryogenic coils and compressed-sensing reconstructions can cut acquisition times to minutes, making concentration mapping feasible on the same temporal scale as the ^{1}H scans. Together, these additions would turn the current single-contrast experiment into a multimodal, multiphysics platform capable of linking ion transport, fluid flow and space-charge formation directly to the morphological pathways captured in this chapter.

Overall, this chapter demonstrates that indirect ^{1}H MRI not only images but quantifies lithium dendrite dynamics in operando. It shows how circuit topology (parallel versus series) dictates morphological evolution, and it establishes a workflow for extracting volumes, tip growth rates, and filling fractions that will directly inform and validate the diffusion- limited aggregation and biased-DLA models developed in Chapter 4. These insights suggest that enforcing uniform current pathways (e.g., through series wiring or active battery management) and employing well-timed polarity reversals may both be viable strategies for mitigating dendrite-induced failure in next-generation lithium metal batteries.

Chapter 4

Electrodeposition Modelling

4.1 Introduction

Electrodeposition modelling provides the indispensable theoretical counter-part to the operando MRI experiments presented in the previous chapter. Whereas Chapter 3 revealed *where* and *when* lithium dendrites emerge inside a symmetric test cell, Chapter 4 seeks to expand/validate our understanding why those morphologies arise and how they evolve under different electrochemical conditions. To that end two similar, yet fundamentally very different numerical frameworks are developed. Both are modified versions of the simple diffusion-limited aggregation (DLA) model [13]. The first, labelled the Simple Deposition Prediction Model, focuses exclusively on modelling ion transport mechanics, aiming to replicate the diffusion-limited electrodeposition regime on a representation of the exact MRI cell. The DLA algorithm is coupled with a steady-state electric field that is the driving force for electromigration. The Laplace solver predicts where the electric potential drops steeply, and where lithium is most likely to nucleate. Because the algorithm neglects time-dependent mass transport and electron-transfer kinetics, it can be evaluated in seconds. It can be suited for rapid geometry optimisation and coupled with an imaging method such as MRI could prove useful in dendrite prevention studies that focus on altering ion-transport mechanics.

The second framework, the Two-Dimensional Multi-Body Diffusion-Limited Aggregation (MBDLA) Model, aims to combine the stochastic nature of dendrite growth with basic ion-transport and surface kinetics to explore the pattern formation across a range of operating conditions. Operating on a 512×256 lattice, it tracks thousands of explicit Li^+ ions that perform biased random walks through the electrolyte, accompanied by an evolving electric field and adhere to the metal surface according to a tuneable kinetic parameter k_r. A dimensionless electric-bias coefficient b_E controls the competition between diffusion and electromigration, while the free-ion volume fraction ρ_f sets the supply of plating species. By sweeping these three parameters the simulation generates a morphological phase diagram that links operating conditions to measurable descriptors such as deposit density, growth-front roughness and box-counting fractal dimension. This model provides a solid basis for further work possibly extending the model into a 3^{rd} dimension and relating with physical quantities. Along with some computing efficiency tweaks, such models provide a more time-efficient way to study the electrodeposition process compared to more complex phase-field and molecular dynamics models.

Although the presented models are similar, this chapter will be split, so each model will have a dedicated subsection; Chapter 4.2 presents the simple deposition prediction model and the second, 2D MBDLA model is presented in Chapter 4.3. Each chapter has the same structure; materials and methods, results and discussion. The chapter is concluded by a

common conclusion section (Chapter 4.4), highlighting where the two models converge, where they diverge and what that implies for designing dendrite-resistant lithium-metal batteries. This chapter lays the theoretical groundwork for the mitigation strategies and design guidelines that are distilled in the final chapter of this thesis (Chapter 5).

4.2 Simple Deposition Prediction Model

4.2.1 Materials and Methods

A lithium symmetric cell was constructed to observe and simulate dendritic growth under controlled conditions. The experimental protocol and raw image data processing procedures are described in Chapter 3.2. The cell used for imaging is shown in Figure 10A. The cell design features two 16×4 mm, 0.3 mm thick lithium plates, separated by a distance of 8 mm. Dendrite growth was driven by an applied current of ≈ 2.5 mA (≈ 3 mA/cm^2).

A diffusion-limited aggregation (DLA) algorithm with an applied electric-field bias was developed to simulate the growth of lithium dendrites between each MRI observation. The simulation domain was a 3D grid matching the internal dimensions of the cell at the MRI resolution. Specifically, a computational grid of $102 \times 51 \times 26$ voxels was used to correspond directly to the volume imaged by MRI. Each voxel in the grid represents a cube of side length 156 µm, and can be either empty (electrolyte) or occupied by deposited lithium. The initial condition for each simulation interval was derived from the MRI data: the binary mask of the dendritic structure at the beginning of that interval was loaded onto the grid, marking all voxels containing existing lithium deposits. This approach effectively "seeds" the simulation with the experimentally observed dendrite geometry up to that point in time. Before simulating further growth, the electric potential field in the electrolyte was computed by treating the existing dendrite structure as part of the boundary. The bottom (lithium) electrode – where dendrites form – was held at 0 V (ground), and the top lithium electrode was set to an arbitrary fixed positive potential (the field was later normalised), while the walls were treated as insulating boundaries. The Laplace equation $\nabla^2\varphi = 0$ was solved under these boundary conditions using *COMSOL Multiphysics* (Stockholm, Sweden) to obtain the electric potential φ throughout the electrolyte domain, from which the electric field $\mathbf{E} = -\nabla\varphi$ was derived. The computed 3D field was then used as an input to the DLA growth model.

For each deposition interval between MRI frames, the DLA algorithm was executed to simulate the stochastic growth of new lithium deposits. A number of lithium "particles" equal to the count of new dendritic voxels observed in the corresponding MRI interval was released into the simulation domain one by one. Each particle was introduced at a random position on the top boundary (the surface of the positive electrode) and allowed to perform a random walk through the electrolyte volume until it either attached to the existing dendrite structure or reached the bottom electrode.

To realistically bias the random walk according to electrochemical driving forces, a bias factor b_E was defined, ranging from 0 (completely diffusive transport) to 1 (completely field-driven migration). At $b_E = 0$, a particle has an equal probability to step in any of the six grid directions $(\pm x, \pm y, \pm z)$ at each move, reproducing an unbiased Brownian motion. At $b_E = 1$, movement is deterministic along field lines – the particle always steps in the direction that locally most strongly reduces the electric potential (i.e. directly toward the negative electrode). For intermediate values ($0 < b_E < 1$), the motion is a biased random walk: the probability p_i of stepping in a given direction i ($i \in \{x, y, z\}$) is proportional to the absolute component of the electric field in that direction:

$$p_{i+} = \begin{cases} \frac{1}{6} + b_E \left(E_i^{norm} - \frac{1}{6} \right) & \text{if} \quad E_i \geq 0 \\ \frac{1}{6}(1 - b_E) & \text{if} \quad E_i < 0 \end{cases}, \tag{4.1}$$

$$p_{i-} = \begin{cases} \frac{1}{6}(1 - b_E) & \text{if} \quad E_i \geq 0 \\ \frac{1}{6} + b_E \left(E_i^{norm} - \frac{1}{6} \right) & \text{if} \quad E_i < 0 \end{cases}. \tag{4.2}$$

Here, p_{i+}, p_{i-} are the jump probabilities in the positive and negative direction along the i-axis, E_i^{norm} is the component of the normalized electric field vector. This bias model effectively tunes the relative influence of electromigration and diffusion on how the lithium ions find the deposition sites. Each particle wanders under this biased random walk until it encounters a surface where it can stick: if it comes into contact with any voxel already occupied by lithium (the existing dendrite structure) or reaches the grounded electrode surface, it is deposited there. That particle's trajectory is then complete, and the next particle is released from the top. The growth simulation for a given interval continues until the predetermined number of new deposition sites (matching the MRI's observed growth for that interval) have been filled. This approach ensures that the simulated growth in each interval stops at a point comparable to the experiment, since the same amount of lithium is plated as was actually observed. The entire sequence of ten MRI experiments (nine intervals of growth) was simulated in this stepwise fashion. To account for the inherent randomness of the deposition process, each interval's simulation was repeated 50 times for each set of parameters, and the results were aggregated for statistical analysis. Bias values of $b_E = 0.0, 0.1, 0.2, \ldots, 0.9$ were tested, spanning the full range from pure diffusion-limited aggregation to strongly field-dominated growth. In total, 9 growth intervals $\times$ 10 bias settings $\times$ 50 runs = 4500 independent 3D simulations were performed. All simulation logic was implemented in Python, and a single-threaded run of one interval took on the order of 2–5 minutes on a standard desktop CPU (Intel i7 processor). This runtime was manageable for the large number of repetitions, and could be further reduced with code optimization or parallelization if needed.

Two quantitative metrics were defined to evaluate how well the simulations matched the experimental results. *First*, an overlap fraction o was calculated, defined as the fraction of the simulated deposition sites that correctly overlapped an actual dendritic growth site observed in the MRI. Equivalently, if N_d is the number of new dendrite voxels added in the experiment (and thus also in the simulation) for a given interval, and N_o is the number of those voxels that coincide in both the simulation and MRI datasets, then the overlap metric is $o = N_o/N_d$. This simple metric ranges from 0 (no overlap between simulated and real deposits) to 1 (perfect overlap, every simulated deposit is at a location where a real dendrite grew). Second, a displacement error s was introduced to capture the average distance between simulated and actual deposits. For each new dendritic voxel observed in the MRI, the shortest distance to any simulated new deposit voxel was measured. These distances were then averaged over all deposition events in that interval, and the result was normalized by the maximum possible distance in the cell (the length of the cell's spatial diagonal) to give a dimensionless measure. By definition, a smaller s indicates closer agreement: if $s = 0$, every simulated deposit lies exactly at a real deposit location (perfect prediction), whereas larger values signify that simulated deposits tend to land farther from where the real dendrites grew (poor spatial accuracy). Unlike o, s penalizes near-misses: even if a simulated voxel does not directly overlap the real one, it will still contribute a

smaller distance if it is nearby. Both parameters were computed for each individual simulation run and for each time step. These were then averaged over all 50 runs (and over all time intervals when comparing different b_E values) to obtain mean values with standard deviations. Together, these two metrics provide a robust assessment of model accuracy in reproducing not just the presence of dendrite growth at the correct locations (overlap) but also the proximity of any missed predictions (displacement). In addition to these direct comparison metrics, the fractal dimension of the dendritic structures was analysed as an independent indicator of morphology. Fractal dimension is a measure of how fully a pattern fills space, and for dendritic aggregates it quantifies their branching complexity. To compute the fractal dimension d_f of a 3D dendrite shape, a standard box-counting method was applied: the binary volume was covered with cubic boxes of size ε, and the number of boxes $N(\varepsilon)$ that contain any part of the dendrite was counted. Repeating this for a range of box sizes ($\varepsilon = 1$ voxel up to the size of the whole domain) yields a relationship $N(\varepsilon) \propto \varepsilon^{d_f}$ for self-similar structures. This procedure was performed on the 3D binary masks of the measured dendrites at each time point, as well as on the binary output of the simulated dendrite after each interval. For consistency, fractal dimensions were calculated on the "optimal" simulation runs (those using the best-fitting bias parameter, as determined by the overlap/displacement analysis) and then averaged over all times and repeats. The corresponding MRI-based fractal dimensions were similarly averaged, accounting for the small error due to image noise in the MRI data. For the schematic of the workflow, refer to Figure 24.

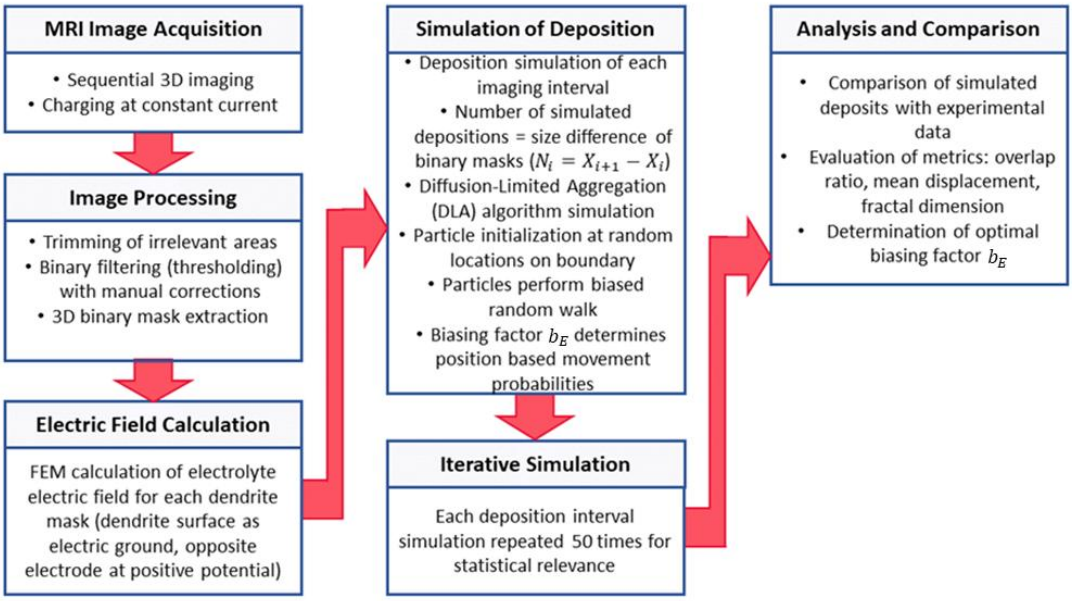


Figure 24: Comparison of fractal dimensions from MRI (blue) and simulations (red) over time. Simulation bars show the mean of 50 runs; error bars indicate standard deviation. MRI error bars reflect calculation uncertainty.

4.2.2 Results

Sequential 3D ^{1}H-MRI revealed a clear transition from an initially smooth Li surface to a densely branched network over the 33.3 h experiment (Figure 25). At 3.3 h the electrode–electrolyte interface was almost featureless. By 6.7 h isolated protrusions appeared; these early "seeds" extended significantly into the electrolyte but showed little lateral branching. Up to 30 h the deposits grew steadily, producing a sparse forest of filamentary dendrites

that consumed the majority of the inter-electrode gap. This rapid, dendritic growth is typical for the Sand's regime, where ion depletion near the surface and a strong electric field at the tips produced runaway elongation and branching [14]. After this point, the dendrites seemed to reach the opposing electrode, resulting in little additional growth.

Because metallic Li and the housing materials do not produce any detectable NMR signal, the MRI "void" exaggerates the true metal volume. Nevertheless, the binary masks extracted from each scan provide a reliable map of where new lithium has displaced and shielded the electrolyte, and thus form an experimental basis for model validation.

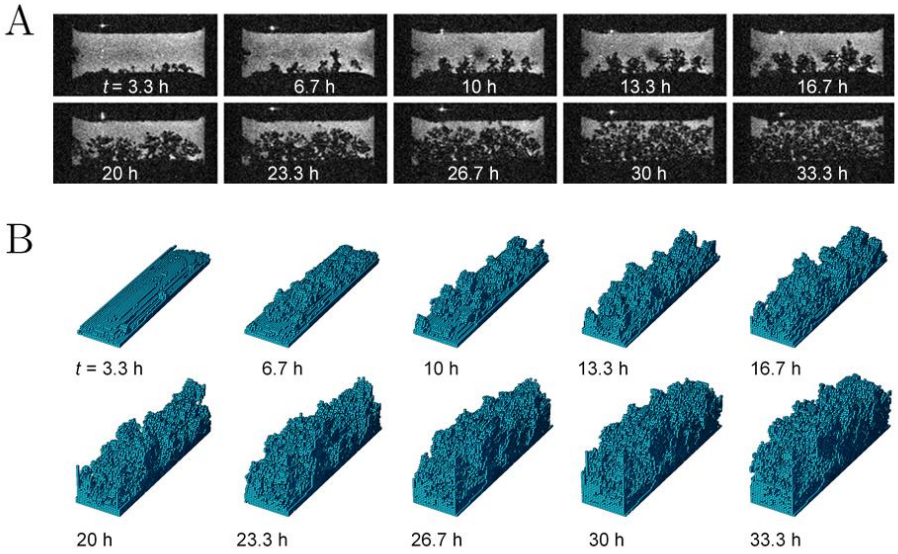


Figure 25: (A) Consecutive 2D slices through the cell show the Li surface progressing from nearly featureless (3.3 h) to a densely branched front (33.3 h). (B) Volume-rendered binary masks, derived from the same MRI data, visualise how protrusions propagate and merge throughout the electrolyte as charging proceeds.

Finite-element solutions of Laplace's equation, using each MRI-derived geometry as a boundary condition, showed that the presence of conductive protrusions focuses the electric field into narrow funnels at dendrite tips (Figure 26). Peak field intensities were 3–5× higher at the most advanced tips than at nearby flat regions, while sheltered recesses behind large branches experienced almost zero field. Current-density vectors pointed steeply into active tips, confirming that electromigration overwhelmingly directs Li^+ to these locations once even modest surface roughness develops. This non-uniform field distribution justifies the need for a growth algorithm that couples diffusion with a spatially varying drift term.

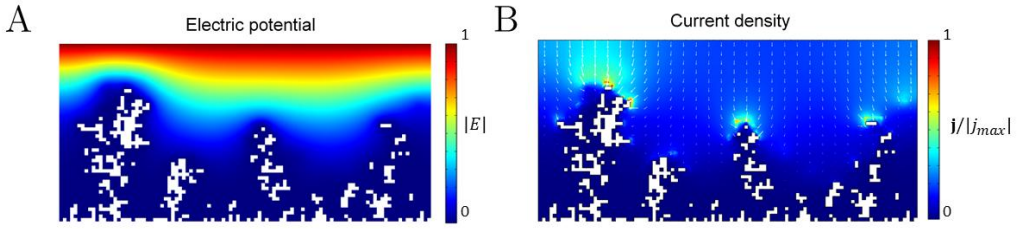


Figure 26: (A) colour map of electric potential, highest near the top and lowest at the dendrite-covered electrode bottom. (B) Corresponding current-density map with vectors

indicating ion flux; red regions at dendrite tips highlight intense, tip-focused currents that steer further growth.

The diffusion-limited aggregation (DLA) model was executed for bias factors $b_E = 0.0 - 0.9$ in 0.1 increments, for each time interval, which was repeated fifty times for statistics. Two metrics measured predictive accuracy: First, the overlap fraction (o) – the proportion of simulated voxels that coincide with experimentally observed new deposits and secondly, the displacement error (s) – the mean normalized distance from each real deposit voxel to the nearest simulated voxel.

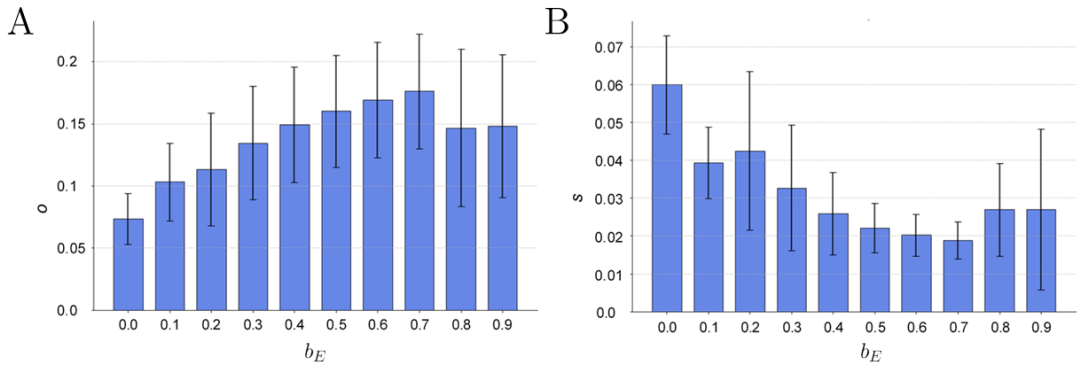


Figure 27 shows that the mean o rises monotonically from $\approx 0.08 \pm 0.02$ at $b_E = 0$ (purely diffusive) to a broad maximum of 0.17 ± 0.05 at $b_E \approx 0.7$, then plateaus. Conversely, mean s falls from 0.06 to a minimum of 0.02 around the same b_E value and increases slightly thereafter. The optimal compromise between diffusion and drift is therefore $b_E \approx 0.7$; this setting was used for all subsequent comparisons.

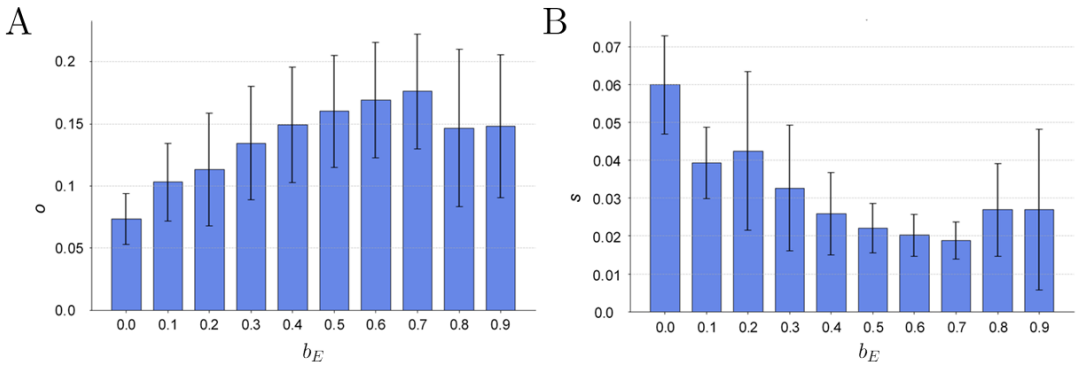


Figure 27: Bar charts summarise 50 simulation runs per time interval ($9 \times 50 = 450$ total), per b_E value. (A) Mean voxel-overlap ratio rises with b_E, peaking near 0.7. (B) Mean normalised displacement error falls to a minimum at the same b_E, confirming 0.7 as the optimal compromise between diffusion and drift. Error bars represent the standard deviation of the mean.

With $b_E = 0.7$, nine sequential "seed-and-grow" simulation sets were run, each starting from the preceding MRI mask and depositing exactly the number of new voxels recorded experimentally for that interval. Figure 28 overlays simulated additions (red) onto the measured structures. Throughout the experiment the model preferentially extends existing tips, mirrors branching directions, and rarely predicts deposits where none appear in the next MRI. Quantitatively, mean $o = 0.17$ and mean $s = 0.02$ across all intervals, confirming that nearly two-thirds of all new growth sites are predicted exactly and most of the remainder lie within one voxel (~0.16 mm) of the true location.

Discrepancies are most pronounced during the late dense-growth stage: the model occasionally over-concentrates deposition on the tallest branch, whereas the experiment shows a few secondary tips catching up. This reflects the stochastic nature of real Li plating, where local variations in SEI resistance or convection (which the present model omits) can slightly redistribute current.

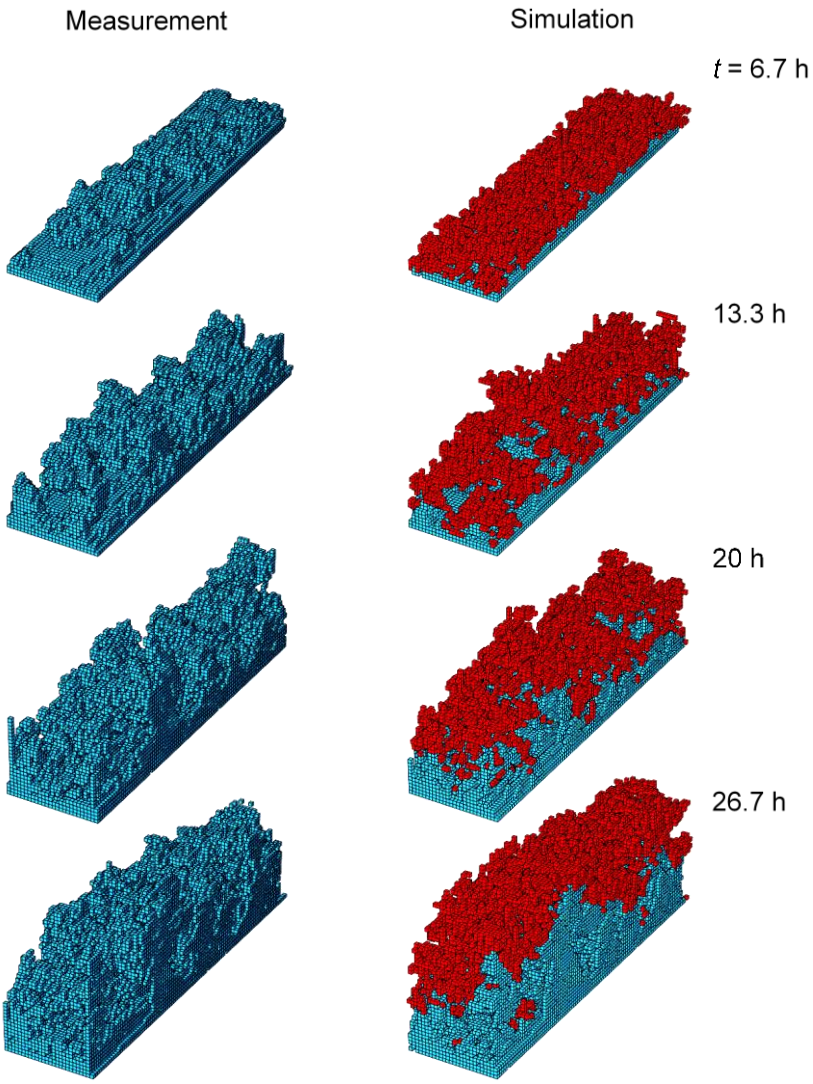


Figure 28: Validation of the biased-DLA model against MRI. For each time point, the left panel shows the 3D dendrite mask extracted from MRI; the right panel overlays predicted new deposition sites (red) from one randomly selected simulation (with $c = 0.7$) on the previous MRI frame. The close spatial match demonstrates that the model pinpoints where lithium is most likely to plate next.

Fractal dimension d_f was computed by 3D box-counting for both MRI and simulated structures at every time point (Figure 29). Experimentally, d_f rose from 2.23 ± 0.03 at 3.3 h to 2.55 ± 0.02 at 33.3 h, reflecting the progression from isolated spikes to a space-filling

ramified front; values consistent with classical 3D DLA where $d_f \approx 2.5$ [130]. The model reproduces this evolution: the simulated mean d_f per time interval is within error of the experimentally measured d_f at any time, confirming that the bias-tuned DLA algorithm not only places lithium in the right regions but also develops the correct multiscale branching morphology.

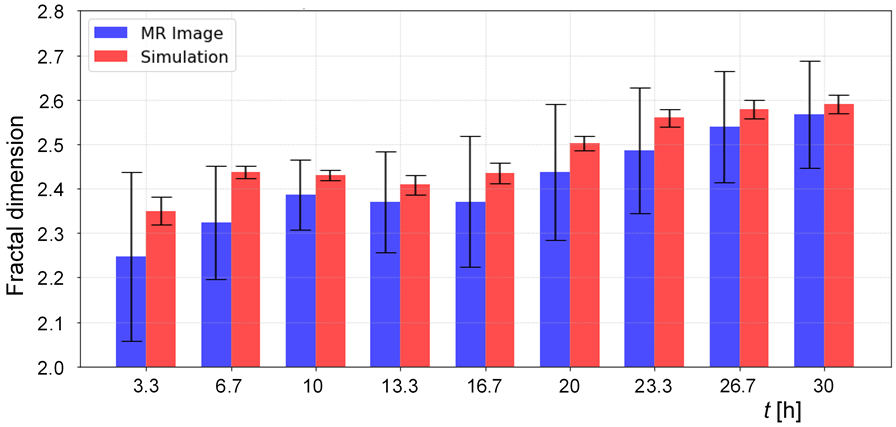


Figure 29: Fractal dimension (d_f) of measured and simulated dendrites over time. Blue bars track the fractal dimension derived from MRI masks; red bars give the average of fifty simulations. Both rise from ≈ 2.25 to ≈ 2.55, showing that the model reproduces the increasing geometric complexity of the growing deposit and remains within experimental uncertainty at every stage. Error bars on the MRI data stem from fractal dimension calculation uncertainty, while the error bars for the simulation data represent standard deviation of the average.

4.2.3 Discussion

The above results demonstrate that incorporating an electric-field bias into a diffusion-limited aggregation model can successfully replicate the growth of lithium dendrites as observed in operando MRI. While biased DLA approaches have been explored previously (for example, in 2D simulations of electrodeposition under a uniform field [54], [58], [130]), the present implementation distinguishes itself by dynamically coupling the bias to the evolving dendrite geometry. At each prescribed interval, the electric field is recalculated based on the current shape of the deposit, and the random-walk probabilities for incoming particles are adjusted accordingly. This represents a more realistic physical scenario than assuming a constant, unchanging field. This methodological improvement makes the model a hybrid between pure diffusion-limited aggregation and a deterministic electromigration-driven growth model. It focuses specifically on the competition between ionic diffusion and migration, which are believed to be the dominant factors in lithium dendrite formation under the high-current conditions of this study [14]. By intentionally simplifying or excluding other processes (mechanical stress effects, solid-electrolyte interphase (SEI) chemistry, surface energy anisotropy, etc.), the model remains computationally light while zeroing in on the essential electro-transport phenomena. Such simplicity is advantageous for a parametric study of dendritic growth tendencies. It is acknowledged that real battery systems involve many phenomena (Chapter 2.1) – for instance, stress in the lithium metal can influence dendrite growth, and SEI layers can modify deposition kinetics – but those were beyond the scope of the present simulation and were consistently neglected to keep the model tractable. Instead, the model effectively treats the ion concentration in the bulk electrolyte as roughly uniform (until dendrites grow, no concentration gradients are

explicitly modelled) and encapsulates the driving force balance between electromigration and diffusion in a single tuneable parameter c. This intentional reductionism allows for clear interpretation of results and fast computation, which are valuable for a first-pass predictive tool.

The conditions of our experiments fall into the so-called Sand's regime of dendritic plating, characterized by relatively high current density and the eventual depletion of electrolyte ions near the electrode surface. In this regime, electromigration of Li^+ toward the negative electrode is very strong; ions are pulled rapidly toward regions of high field, while diffusive transport struggles to resupply the ion-depleted regions behind the advancing deposition front, resulting in strongly branched, dendritic growth [121]. The DLA model, by itself, does not explicitly calculate ion concentration profiles; however, the bias factor b_E serves as an effective proxy for the relative dominance of electromigration vs. diffusion. A higher b_E value implies that the model is putting much more weight on the electric field – mimicking a situation where migration far outpaces diffusion – whereas a lower b_E corresponds to a more diffusion-moderated deposition. In physical terms, increasing b_E in the model is akin to either raising the applied current (stronger field) or reducing the diffusivity of ions (so that diffusion is less capable of smoothing out concentration differences). The calibration study found that $b_E \approx 0.7$ provided the best match to our data, indicating that under our experimental conditions, electromigration was indeed significantly more influential than diffusion, but a small degree of randomness (diffusive wandering) still had to be allowed to accurately reproduce the branching patterns. One assumption made in comparing the model to MRI data is the conversion between MRI voxel voids and lithium content. We assumed that one voxel of MRI void corresponds to one "particle" of lithium in the simulation (essentially a partition coefficient of 1 for lithium in dendrite vs. MRI void). Refining this conversion (for example, if MRI voids systematically overestimate actual lithium volume by some factor) would further improve the quantitative accuracy of the model, but the current approach is sufficient for capturing the overall behaviour.

Utility and Limitations of the Model: The biased DLA model presented here offers a computationally efficient way to predict dendritic growth patterns under conditions similar to our experiment. With only a single free parameter (b_E) governing the growth behaviour, it is straightforward to adjust and interpret. The model successfully reproduced key experimental observations – the spatial distribution of new dendrites, the branching complexity, and the general growth rate – which suggests it could be a useful predictive tool for scenarios where one needs to gauge where dendrites are likely to form. For instance, by tuning b_E according to a given set of operating conditions (electrolyte, current density, etc.), one could simulate and visualize potential problem areas for dendrite formation in a cell without conducting a full 3D experiment each time. However, there are some important limitations to acknowledge. First, the current model in its simplest form relies on experimental imaging input to know when to stop the simulation (i.e. how much lithium to deposit) for each interval. In a truly predictive standalone mode, one would need an independent way to decide how long to run the simulation or how many particles to deposit, based on the applied current and electrolyte properties. In principle, this could be done by linking the simulation to a known plating rate or limiting current density, but that isn't built into the present model. Second, the resolution of the model is constrained by the MRI voxel size. Our grid (156 μm voxels) treats each voxel as an indivisible chunk of lithium once filled. Real lithium dendrites are much finer (on the order of microns), meaning each "voxel particle" in the simulation actually represents an aggregate of many microscopic fibres. Thus, the model cannot and does not aim to resolve the micro-structure inside each voxel – for example, the model cannot distinguish whether a voxel is filled by one thick dendrite or several thinner ones. It instead operates at the mesoscale, tracking the envelope

of the dendritic mass. This is acceptable for comparison to MRI (since MRI also sees only the voxel-wise occupancy), but it means terms like "particle" in the simulation are a coarse concept.

A particularly novel aspect is the combination of a computed electric field with a stochastic growth algorithm, which, to our knowledge, had not been applied in 3D for lithium electrodeposition prior to this work. However, many ways to enhance the model remain. One improvement would be implementing a multi-particle deposition approach wherein many particles are allowed to move and deposit simultaneously (rather than strictly one after the other). This could better mimic the concurrent growth of multiple dendrite tips competing for ions, and might be necessary if one wanted to simulate effects like two nearby tips growing into each other's diffusion zones. Another extension would be to incorporate surface diffusion of lithium once deposited – currently, once a particle sticks, it stays fixed, but in reality, lithium atoms on the surface can relocate slightly, which might smooth out extremely sharp tips or allow slight coalescence of neighbouring branches [131]. Increasing the spatial resolution of the simulation (using smaller voxels) would improve the representation of fine structures, though at a computational cost. Perhaps the most significant upgrade would be to explicitly solve for ion concentration dynamics in the electrolyte during deposition. This would involve coupling the DLA deposition steps to a diffusion equation for Li^+ and could capture the formation of a true depletion region (space-charge layer) in the simulation. Including concentration and its effect on local overpotential would make the model much more self-contained – it could predict when deposition slows due to ion exhaustion, for instance, rather than relying on a predetermined particle count.

In summary, the biased DLA model validated by MRI provides a powerful and efficient tool for understanding dendritic growth. It captures the essential behaviour of lithium dendrites in a charging cell and offers a foundation upon which more detailed physics can be added.

4.3 2D MBDLA Model

4.3.1 Materials and Methods

The second modelling framework developed in this work is a two-dimensional, multi-body diffusion-limited aggregation (MBDLA) model that captures the interaction between ionic transport, electric-field migration and surface reaction kinetics during lithium electrodeposition. Whereas the simple 3D lattice model was constructed to predict the where of deposition inside an arbitrary experimental geometry, the 2D MBDLA model was designed to focus on the morphological regimes that emerge as the competing physical phenomena are tuned. Because the model is confined to a plane and abstracts away many electrochemical details, it is computationally cheap while still simulating the redistribution of the local electric field around a growing conductor and the probabilistic nature of lithium ion reduction at a rough interface.

Framework and model variables

The model is dimensionless, therefore the simulation particle does not necessarily represent a $^+$Li ion, but for the conceptual sake will be referred to as ions and free particles interchangeably. The simulated domain is a rectangular 2D lattice $N_x \times N_y = 512 \times 256$ sites in extent, with the vertical y-axis representing the electrolyte thickness above a flat lithium electrode. Every lattice site is assigned one of four states: deposit, mobile ion, surface-diffusing ion or empty electrolyte. At $t = 0$ the bottom row is fully occupied by

deposit cells, forming an equipotential cathode, while the electrolyte above it is seeded with a homogeneous random distribution of mobile ions at a user-specified volume fraction ρ_f.

An external electric field is applied between the top and bottom, driving cations toward the bottom electrode. To compute the electric field $\mathbf{E}$ at every point in the electrolyte, the electrostatic potential $\varphi(x,\ y)$ is solved from Laplace's equation with appropriate boundary conditions (see below).
Each simulation (Monte-Carlo) step, all the free particles in the simulation try to move according to a predetermined set of rules, in a random order. Particles that touch the cathode or dendrites are labelled as surface-diffusing particles until they are permanently stuck. The simulation stops, once the growth reaches a height of $y = 128$.

Whenever an ion attempts to move it consults a drift–diffusion rule derived from a dimensionless electric-bias parameter b_E, which scales the strength of directed motion relative to Brownian diffusion, thus serving the same function as in the previous model. The probabilities for the direction of the jump are based on the orientation of the vector $\mathbf{E}$ and are calculated as for the previous model, adapted for 2D. A big difference is introduced in the way the magnitude of $\mathbf{E}$ influences the jump probabilities. A hyperbolic mapping converts $|E|$ into an effective local drift coefficient $b_E^{(loc)}$:

$$b_E^{(loc)} = \frac{|E|/|E_{bulk}|}{1 + |E|/|E_{bulk}|} b_E. \tag{4.3}$$

When $|E| \ll 1$ the ratio is small and $b_E^{loc} \approx 0$; the walk therefore remains almost isotropic. When $|E| \gg 1$ the ratio tends to unity, so $b_E^{loc} \to b_E$; the drift share reaches a hard ceiling and the hop probabilities become insensitive to any further growth in $|E|$.

The second tuneable model parameter is surface reactivity (k_r), which dictates the activity of the ions once in contact with the surface of the electrode/deposit. In short, $k_r \to 0$ means low surface diffusivity of ions, high sticking likelihood, and vice-versa for $k_r \to 1$. Whenever a particle touches the growing structure, it follows the following rules:

- At coordination number ≥ 2 the ion sticks unconditionally
- Otherwise, a deposition probability p_{stick} is calculated from the local current density $\mathbf{j}$, normalized by the strongest flux in the whole electrolyte $\mathbf{j_{max}}$:

$$p_{stick} = (1 - k_r) \frac{|j|}{|j_{max}|} \tag{4.4}$$

- If not deposited, the ion jumps according to a "surface diffusion" jump probability p_{SD}, weighed by the current and target coordination numbers (n_c, n_t). Diagonal moves are permitted, but disfavoured:

$$p_{SD} = k_r(e^{n_t - n_c}) \times \begin{cases} 1; \text{ axial move} \\ 0.5; \text{ diagonal move} \end{cases} \tag{4.5}$$

  The probabilities are then normalised and a hop direction is selected with a random number $\in$ [0,1]. Such a method favours moves that increase coordination.
- If no valid moves are available, the particle sticks.

The final control variable is the free particle/ion density ρ_f. This number determines the initial density of particles in the electrolyte. An infinite electrolyte reservoir is simulated by keeping track of density of particles in a narrow band at the upper boundary and injecting them at random vacant sites at $y = 256$ when it drops.

The 2D domain uses closed boundary conditions in the lateral (horizontal) direction. On the top domain, an open boundary condition is used, so that the particles can move

out and be removed. Likewise, the top rows serve as a source of new ions, as described above. The schematic of the simulation model is shown in Figure 30.

Electric field calculation
The electric potential $\varphi(x, y)$ inside the electrolyte is recomputed periodically to account for the evolving conductor morphology. The electrode (as well as newly grown deposit cells) is clamped at $\varphi = 0$. The top boundary is held at a $\phi = 1$. The lateral edges are modelled as insulators (Dirichlet boundary conditions). Under the assumption that the Debye length is small relative to lattice spacing, free-charge density is neglected and the system obeys Laplace's equation $\nabla^2\varphi = 0$. After discretization with five-point finite differences, an algebraic multigrid solver (*PyAMG* library in *Python*) solves the linear system for φ at each node. From the potential, field $\mathbf{E}$ is derived. This electric field is calculated before the first simulation step, as well as every time the dendrite growth front grows by 10 grid units.

Parameter Space
The model was used to simulate the deposition for a broad range of control parameters. Parameter sets were constructed using every possible combination of the following values:
- For b_E and k_R the following values were used: (0.01, 0.1, 0.3, 0.5, 0.7, 0.9, 0.99)
- Three different concentration scenarios were simulated: Low, medium, and high free ion density with ρ_f set to 0.001, 0.01 and 0.1, respectively.
  This results in 147 simulation runs.

Simulation Performance
To reduce the simulation runtime, the lattice update kernel is JIT-compiled with *Numba*. The simulation was run on a standard PC (AMD Ryzen 5 3600 CPU) under a Windows environment. We leveraged parallel processing to perform multiple simulation runs in parallel (when doing parameter sweeps). Most 2D simulations completed in just a few minutes, while more extreme cases (e.g. very slow growth due to low b_E, ρ_f or high k_r leading to many simulation steps) could take 10 or more minutes to compute.

Metrics
Throughout each simulation, data were recorded intermittently to quantify the evolving morphology of the lithium deposit. Along some basic information (e.g. current number of simulation steps, number of deposited particles, maximum front height) key output measures recorded include:
- Deposit Density: This is defined as the ratio of the area occupied by deposited lithium to the total area below the maximum height of the deposit.
- Average Deposit Height: The average height is the mean of all the maximum heights for every x in the grid. The average is accompanied by the standard deviation, reflecting the surface roughness.
- Fractal Dimension: To characterize the morphology of the deposits in terms of self-similarity and branching, we calculated an approximate fractal dimension d_f of the 2D deposit clusters using a standard box-counting method, as described previously.

At the simulation end, the grid mask, which contains the information about all particles in the simulation, was written to a file.

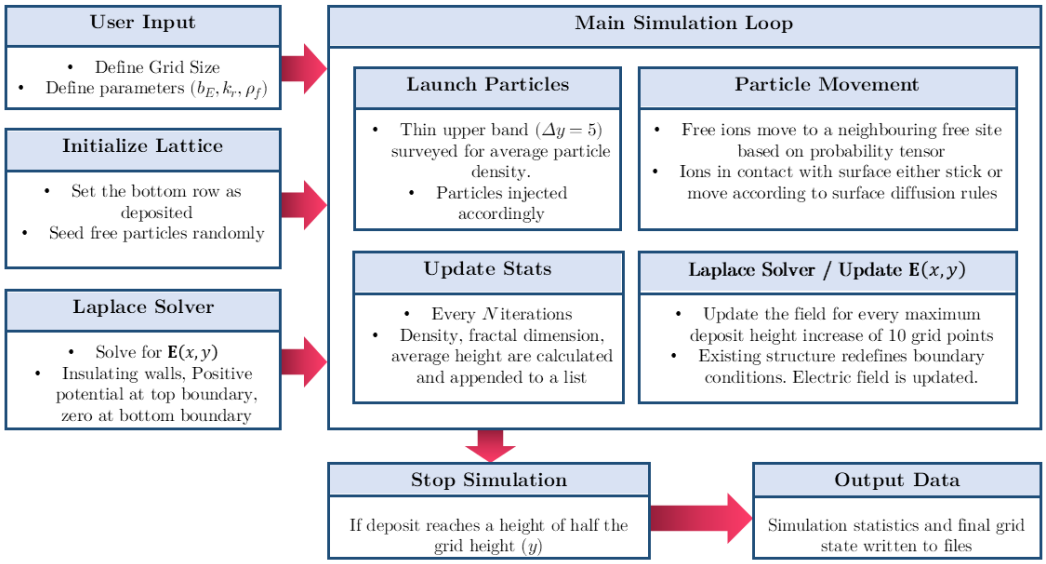


Figure 30: A schematic showing the algorithm composing the 2D multi-body diffusion limited aggregation (MBDLA) model.

4.3.2 Results

Figure 31 presents morphological phase diagrams from electrodeposits generated by the presented 2D multi-body diffusion-limited aggregation (MBDLA) model under an applied Laplacian field. Panel A illustrates the dependence of deposit density (ρ_d) on the dimensionless electric field bias (b_E), controlling ion drift, and the reaction rate parameter (k_r), controlling surface sticking versus diffusion. At low ion concentration ($\rho_f = 0.001$), deposits are sparse (~0.2 lattice-fill density) under diffusion-limited conditions (low b_E, low k_r), forming thin, fractal dendrites. Increasing either b_E or k_r enhances the density, reaching ~0.8–0.9 at high values, as stronger field biasing and faster surface kinetics encourage compact growth.

Raising the initial ion concentration ($\rho_f = 0.01$ or 0.1) increases baseline densities across conditions; even diffusion-limited growth deposits more material when ions are abundant. However, the roles of b_E and k_r remain significant, with contours sloping upward, suggesting compensation between strong electric fields and surface kinetics. At the highest concentration ($\rho_f = 0.1$), even diffusion-limited conditions yield densities around 0.3, higher than at lower concentrations, likely due to concurrent growth of multiple branches filling spaces.

Panel B shows the fractal dimension (d_f) across the parameter space, quantifying morphology from dendritic (~1.5–1.6) to near-planar (~1.8–1.9). Consistent with density results, lower fractal dimensions occur in diffusion-limited, low-field regimes, characterized by random diffusion and immediate sticking, producing filamentary dendrites. Moving toward high b_E and k_r conditions, fractal dimensions approach the Euclidean limit (2.0), indicating dense, space-filling deposits. Both stronger electric fields and increased surface diffusion (higher k_r) monotonically raise d_f, reducing branching and enhancing compactness.

Notably, initial ion concentration minimally influences d_f, as geometry predominantly depends on kinetic and field effects rather than ion availability. However, slightly higher fractal dimensions appear at elevated ion concentrations, even in diffusion-limited regimes,

aligning with increased density observations. Thus, Figure 31 delineates morphological transitions from fractal dendrites (low density, low d_f) to compact deposits (high density, high d_f), smoothly varying with electric field and reaction kinetics.

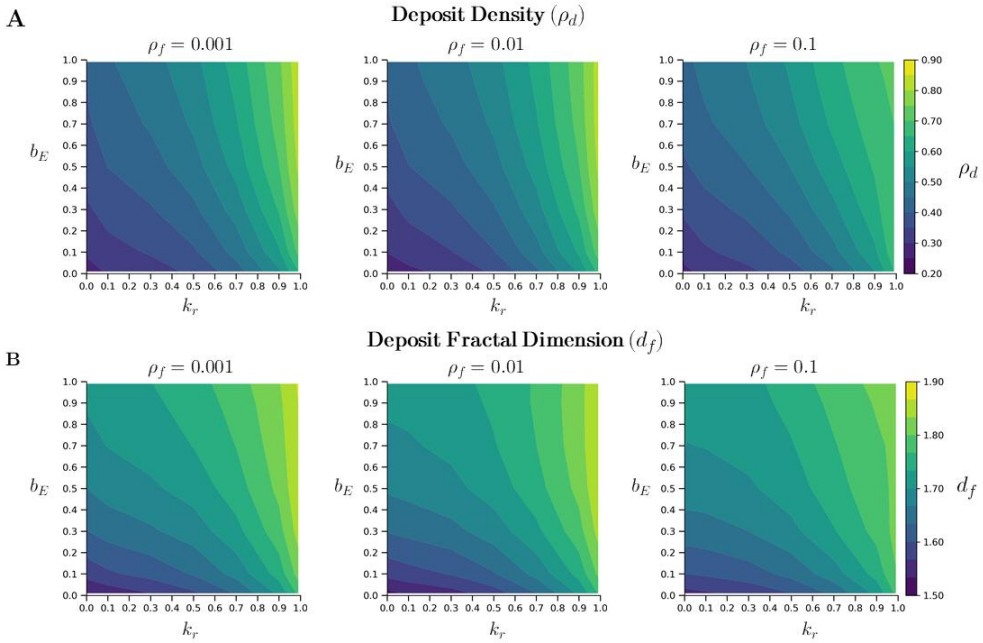


Figure 31: Phase diagrams of deposit characteristics obtained from 2D multi-particle DLA simulations under various model parameters. (A) Deposit density (fraction of area filled below highest deposit, ρ_d) as a function of electric field bias b_E (vertical axis) and reaction propensity k_r (horizontal axis), shown for three initial free ion concentration levels ρ_f = 0.001, 0.01, and 0.1. Warmer colours (green/yellow) indicate more compact, higher-density deposits, while cooler colours (blue/teal) indicate sparse, dendritic deposits. (B) Corresponding fractal dimension d_f of the deposit versus b_E and k_r for the same ρ_f values. The colour maps range from $d_f \approx 1.5$ (highly branched fractal structures) to $d_f \approx 1.9$ (nearly space-filling growth). These phase-space plots map how deposit morphology transitions from dendritic to compact as field and reaction parameters change.

Figure 32 combines quantitative and qualitative information for an intermediate ion supply, $\rho_f = 0.01$. The centre panel is a contour map of the growth time t_{MC} (simulation steps) as a function of the electric-field bias, b_E (vertical axis), and the surface reactivity, k_r (horizontal axis). Dark colours correspond to slow deposition; yellow indicates the fastest films. Four red markers pick out the extreme corners of parameter space, and the surrounding snapshots show the corresponding microstructures. Black pixels are the solid deposit, red dots the remaining free ions.

With a weak driving field and an almost certain sticking event ($b_E = 0.01$, $k_r = 0.01$; bottom-left), ions arrive by random walk and attach immediately. The result is a sparse "forest" of thin, branched dendrites separated by large gaps. Each tree competes only with its nearest neighbours, so lateral screening is minimal and the deposit remains low-density. This morphology mirrors classical diffusion-limited aggregation, and the long growth time on the map (green band) confirms that transport, not reaction, is the bottleneck.

Keeping the same weak field but allowing ions to wander many times before incorporation ($b_E = 0.01$, $k_r = 0.99$; bottom-right) produces short, bushy clusters. Surface diffusion lets particles fill hollows, so each nucleus becomes a rounded "shrub"

rather than a needle. The film is noticeably denser than in case 1, yet still heterogeneous because no field guides ions to particular sites. Growth slows further (blue–green region on the map) because both transport and reaction now impede advance.

In the third case ($b_E = 0.99$, $k_r = 0.01$; top-left) a strong electric field steers ions directly toward protrusions. Although sticking is immediate, intense electromigration feeds many tips simultaneously, producing a thicket of upright dendrites that are closer together and taller than in case 1 (bottom-left). The deposit is still ramified, but local space filling is higher and the growth time is shorter (purple band) because drift supplements diffusion.

When both the field and surface mobility are high ($b_E = 0.99$, $k_r = 0.99$; top-right), ions funnel rapidly to the interface and then spread laterally before sticking. The outcome is a compact, nearly continuous layer whose top surface undulates smoothly like a row of overlapping hemispheres. Void space inside the film is minimal, and the central map shows relatively short growth times: mass transport is so efficient that reaction now solely limits the rate.

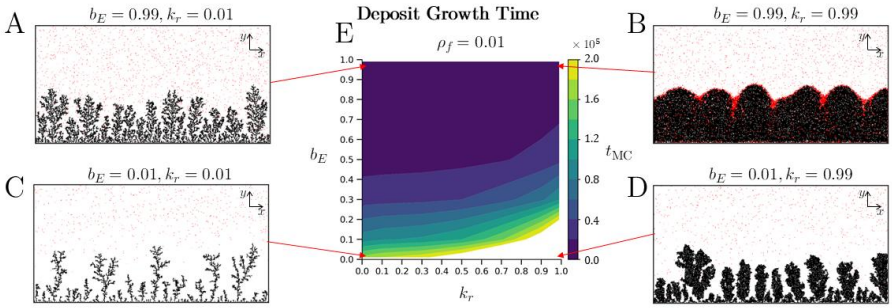


Figure 32: Representative deposit morphologies at phase-diagram extremes, shown for $\rho_f = 0.01$ (moderate ion concentration). The central contour map (E) is the deposit growth time in simulation steps, with four red markers highlighting specific parameter combinations: (A) $b_E = 0.99$, $k_r = 0.01$; (B) $b_E = 0.99$, $k_r = 0.99$; (C) $b_E = 0.01$, $k_r = 0.01$; (D) $b_E = 0.01$, $k_r = 0.99$. Surrounding images show the actual simulated deposit (black) and remaining free ions (red dots) at those points.

Figure 33 depicts the concentration profiles that emerge in the electrolyte after growth and clarifies how both the initial ion inventory and the kinetic parameters govern the thickness of the depleted zone, often termed the diffusion boundary layer. Concentration is normalised to the starting bulk value, so a value of one represents an untouched reservoir and zero denotes total exhaustion of cations. The cathode is located at $y = 0$, while the bulk reservoir is at $y = 256$ lattice units.

The two low-field, low-surface-kinetics cases (blue and cyan curves, $b_E = 0.01$ and $k_r = 0.01$) illustrate the textbook diffusion-limited scenario. With the smaller initial supply (blue, $\rho_f = 0.01$) the surface concentration collapses essentially to zero and remains negligible until roughly $y \approx 100$. Even with ten times more starting ions (cyan, $\rho_f = 0.1$), only about 5–10 % of the bulk concentration survives at the interface, and the profile stays below 10% of bulk for several tens of lattice units. These deep, nearly flat plateaux reveal that ion consumption by the advancing dendrites far outstrips resupply by diffusion when no electric field assists transport. The behaviour closely mirrors Sand's classical depletion, in which the current demand exceeds the diffusion-limited current and a space-charge layer devoid of ions forms adjacent to the electrode.

Introducing a moderate electric field and comparable surface reaction resistance ($b_E = 0.5$, $k_r = 0.5$; red and orange curves) transforms the profiles. After deposition with the same low starting concentration (red, $\rho_f = 0.01$), about 40 % of the bulk value still remains at $y = 0$, and the concentration reaches $80 - 90$ % of bulk by $y \approx 100$. When more ions are available initially (orange, $\rho_f = 0.1$) the surface fraction drops to 15 %, yet in absolute terms the interfacial concentration exceeds that of the red case. The larger inventory allows a higher current, which in turn draws down a greater fraction of the supply, but electromigration continually drags ions toward the electrode, preventing total depletion. The resulting diffusion layer is much thinner and the gradient relaxes to bulk conditions well within the simulation cell.

Comparing blue to red highlights the mitigating role of electromigration: with identical initial concentration, adding a field raises the residual surface concentration from zero to 40 % and shrinks the depletion depth by more than half. The contrast between cyan and orange shows how a larger ion reservoir can drive steeper relative gradients, because higher currents are supportable before transport becomes limiting. In every case, the model reproduces the expected coupling of growth kinetics and mass transport. Severe depletion correlates with the ramified, diffusion-limited morphologies reported in Figure 32, whereas partial depletion corresponds to more compact films. The presence of a fully exhausted region in the low-field simulations is the discrete analogue of the space-charge layer predicted by Chazalviel for ramified growth, while the persistence of a finite interfacial concentration under higher field indicates operation below the Sand limit [14].

Thus, Figure 33 confirms that the simulation captures both extremes of electrochemical deposition: a transport-limited regime where dendrites outrun ion supply and a kinetically limited regime where electromigration and reaction resistance balance, leaving a modest concentration gradient and producing more uniform deposits.

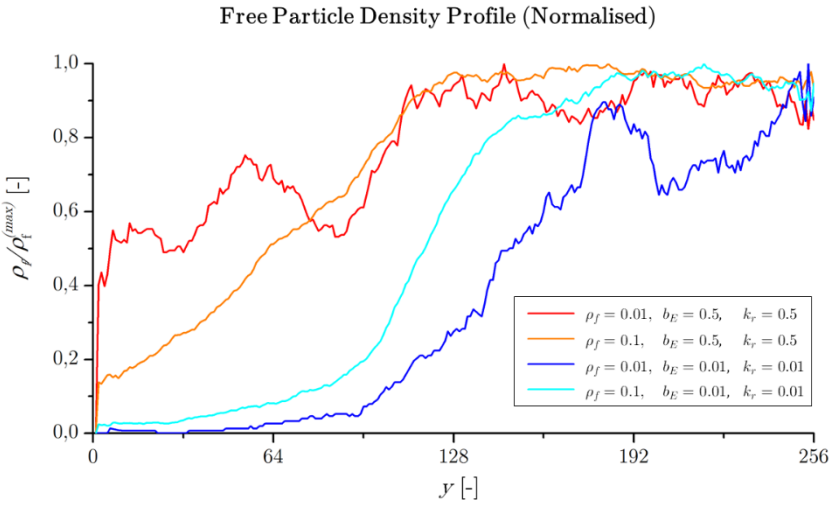


Figure 33: Profiles of the free-ion concentration (normalized) in the electrolyte at the end of simulations for different conditions. The vertical axis is the local free ion density ρ_f normalized by the maximum value $\rho_f^{(max)}$ (so 1.0 represents the reservoir concentration), and the horizontal axis y is the distance from the electrode (with $y = 0$ at the deposition surface and $y = 256$ the top boundary). Four curves compare the effect of initial concentration and field/kinetic parameters. All profiles start near 0 at the electrode (complete or near-complete depletion) and rise to 1 at the far boundary (bulk concentration), but the depth and severity of the depletion layer differ markedly. The oscillations on the red and blue curves are a consequence of low particle availability (ρ_f).

Figure 34 demonstrates how varying the electric-field bias b_E shapes deposit morphology, while holding the reaction resistivity ($k_r = 0.5$) and ion supply ($\rho_f = 0.01$) constant. At very low fields ($b_E = 0.01$), the growth closely resembles classical diffusion-limited aggregation (DLA): thin, highly branched dendrites are distributed along the electrode, each tip growing independently due to random ion arrival. The resulting structures are fine, filamentous fractals, with multiple dendritic arms competing but none strongly dominant. Free ions (red dots) remain uniformly scattered above the deposit, consistent with isotropic diffusion. The fractal dimension here would be low (around 1.5–1.6), reflecting sparse, diffusion-dominated growth.

Increasing the electric field moderately ($b_E = 0.1$) subtly alters this morphology. While dendritic, the branches are thicker and slightly more clustered, some merging at their bases. The enhanced field induces a more directed ion flux toward the electrode, causing tips to interact and merge rather than remain isolated. This reduces stochasticity, resulting in fewer prominent dendrites but increased density. A mild depletion zone above the deposit indicates emerging concentration polarization, though ions still remain broadly distributed. The fractal dimension rises slightly due to increased local cooperation and denser packing.

At high fields ($b_E \geq 0.9$), a significant shift occurs. The deposit becomes much denser and nearly continuous, forming broader columns rather than isolated dendrites. Individual branches still exist but are shorter, thicker, and closely spaced, producing a more uniform front. Ion trajectories become strongly directional, causing growth sites to evenly share ions rather than compete individually. Consequently, the depletion layer above the deposit is uniform, reflecting planar-like diffusion conditions. The fractal dimension increases to about 1.8, indicative of dense branching morphology, as the field-driven migration efficiently supplies ions directly toward growth fronts.

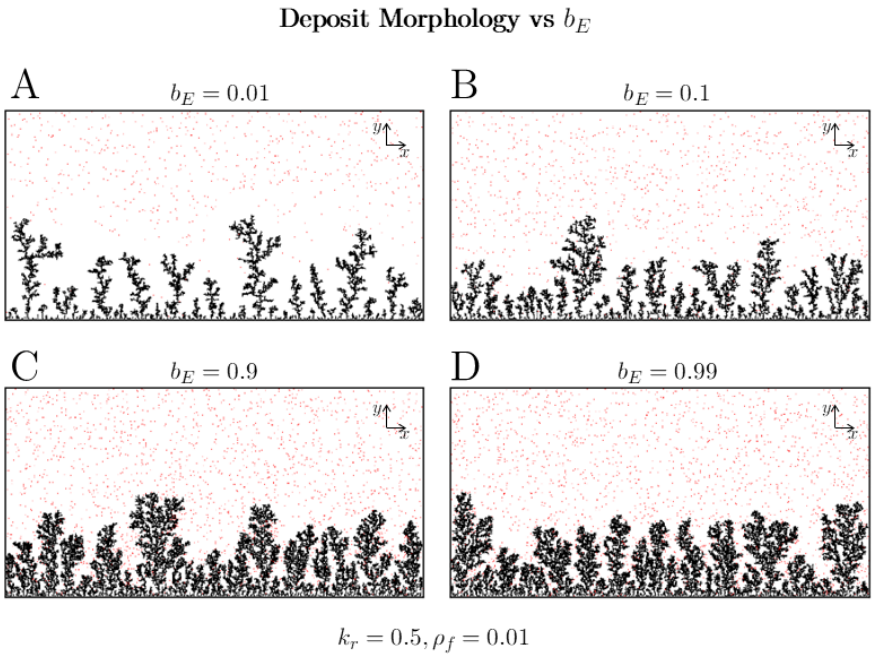


Figure 34: Effect of electric field bias b_E on deposit morphology (with other parameters fixed at $k_r = 0.5, \rho_f = 0.01$). Four simulations are shown with increasing b_E: $b_E = 0.01$ (A), $b_E = 0.1$ (B), $b_E = 0.9$ (C), $b_E = 0.99$ (D). Black regions are the deposit (electrodeposited metal), and red dots are remaining free ions. All deposits grew until reaching the same height criterion. As the field bias increases, the deposit transitions from

a sparse, highly branched form to a denser, more uniform structure. Higher b_E produces greater branching, resulting in thicker, shorter dendrites.

Figure 35 explores how varying the surface reaction kinetics, represented by k_r, independently shapes deposit morphology at constant electric field bias ($b_E = 0.5$) and moderate ion supply ($\rho_f = 0.01$). At the extremely low reaction limit ($k_r = 0.01$), ions essentially stick immediately upon contact (99% sticking probability), resulting in thin, highly dendritic structures resembling classic diffusion-limited aggregation (DLA). These needle-like branches are numerous and finely spaced, generating a rough, sparse interface. The presence of a moderate electric field slightly aligns and clusters these dendrites, creating a coral-like growth front rather than fully random branching, but overall, the morphology remains fractal with low density and a low fractal dimension (~1.5–1.6). Increasing k_r to 0.1 introduces occasional surface mobility, although in the low ranges, k_r does not significantly affect the morphology.

At high k_r (0.9), ions predominantly move or rearrange along the deposit surface before incorporating, significantly altering the morphology to a mossy or granular form. Branches largely disappear, replaced by rounded, overlapping clusters forming a nearly continuous coating with minor indentations. The deposit density markedly increases, reflecting effective lateral growth and pore-filling facilitated by substantial ion mobility. The fractal dimension rises toward ~1.8, indicative of a transition to compact, volumetric growth. The concentration gradient above the deposit is broad and uniform, characteristic of a planar-like diffusion layer.

At the extreme reaction-limited condition ($k_r = 0.99$), ions rarely stick immediately, extensively diffusing before incorporation. The resulting morphology is very compact, essentially forming a smooth, contiguous film with gently undulating surface features rather than dendrites. This condition approaches ideal planar growth, as ions redistribute to occupy energetically favourable positions, smoothing out protrusions. Deposit density peaks near its maximum, with a fractal dimension approaching ~1.9, resembling conditions in experimental electrodeposition where kinetics or additives promote dense, uniform plating.

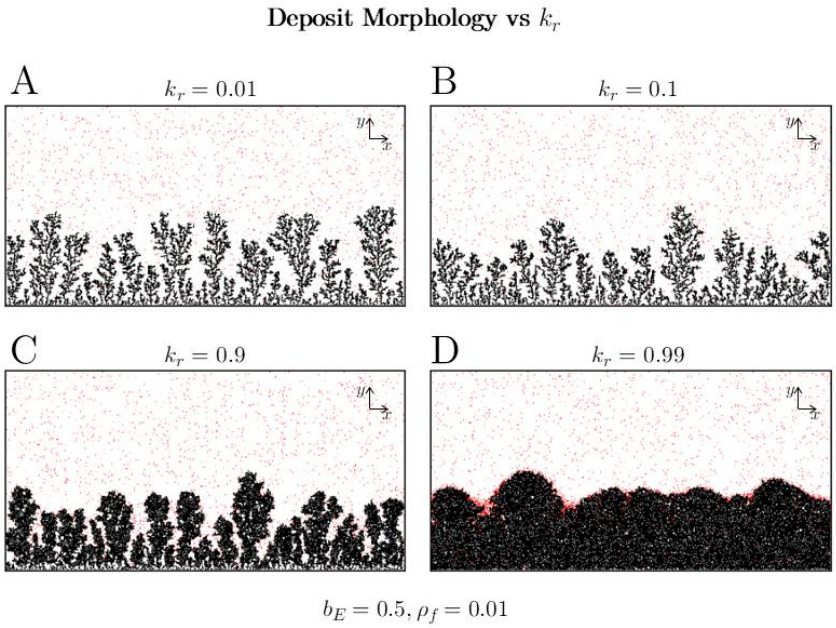


Figure 35: Effect of reaction rate parameter k_r on deposit morphology (with $b_E = 0.5$, $\rho_f = 0.01$ fixed). Four simulations are shown: $k_r = 0.01$ (A), $k_r = 0.1$ (B), $k_r = 0.9$ (C), $k_r = 0.99$ (D). Low k_r corresponds to immediate sticking (diffusion-limited behavior), while high k_r allows extensive surface diffusion before sticking (reaction-limited behavior). The progression from $k_r = 0.01$ to 0.99 shows dendritic structures giving way to a nearly continuous deposit layer. Higher k_r yields thicker, less branched deposits and a smoother deposition front.

4.3.3 Discussion

In this section, we interpret the simulation findings in the context of known electrochemical growth phenomena and literature, highlighting how the model reproduces key physical mechanisms of electrodeposition. The results demonstrate that the morphology of electrodeposited films – ranging from ramified dendrites to compact deposits – is governed by the interplay between diffusion, electromigration, surface reaction kinetics, and ion concentration. We discuss each aspect in turn, relate our observations to prior studies, and underline the scientific significance and novelty of our Laplace-field-enhanced DLA model.

The simulations clearly span two classic electrodeposition regimes: a diffusion-limited dendritic regime and a reaction-limited mossy/compact regime. At low field strength (b_E) and low surface diffusion rate (low k_r), growth is controlled by ion arrival rather than surface kinetics. The deposits form sharp, tree-like dendrites with low density and fractal dimension $d_f \approx 1.5 - 1.6$, mirroring the Diffusion-Limited Aggregation (DLA) model of Witten and Sander [13]. Here, ion concentration gradients develop near the cathode (Figure 33, blue and cyan), depleting cations at the interface. Protruding tips access fresh electrolyte, fuelling runaway growth; a hallmark of tip-driven, space-charge-enhanced dendrites [14]. At high k_r with a relatively strong field bias (b_E), surface attachment becomes rate-limiting and growth is uniform. Deposits are dense and sponge-like, with $d_f \to 1.9$, reflecting a near–space-filling morphology. This behaviour matches observations of lithium plating at low overpotentials or in the presence of additives [121]. Bai et al. (2016) visualized a transition from base-growing mossy clusters to tip-growing dendrites as current exceeded the Sand's capacity [121]; in our model, high k_r yields even nucleation

along the electrode (Figure 35, bottom), whereas low k_r confines growth to a few dominant tips. The critical switch occurs when ion consumption outpaces diffusion. In our parameter space, increasing b_E or lowering k_r forces diffusion limitation (dendrites), while raising k_r maintains reaction control (moss). Thus, by balancing transport and surface kinetics, our stochastic particle model reproduces the full spectrum of experimentally observed morphologies, from fractal dendrites to compact, high-surface-area deposits [121].

A novelty of this DLA-based electrodeposition model is the inclusion of the Laplace field, as previous models included simple field biasing, assuming a uniform field [54], [58], [132]. Iteratively updating the electric field during the simulation should better capture the effects of electrostatic shielding and tip competition. Our results do indeed display higher non-uniformity of growth, corresponding to the shielding and tip competition effects, compared to models with a static, uniform field [54]. A protrusion under strong field draws disproportionate ionic current, but field redistribution ("wrapping around" a tip) also supplies neighbours. The result is a dense array of parallel growths rather than a single, skinny dendrite. Chazalviel's 2D analysis linked filament spacing to applied field and space-charge parameters [14]: higher fields yield closer filaments and denser deposits. In our high-field runs ($b_E = 0.9 - 0.99$), dendrites pack tightly into an almost continuous front.

The electric field introduces electromigration, a key driver of real electrodeposition under bias (b_E). As b_E increases, deposits become denser and less branched, shifting morphology toward compact forms (Figure 31). Note, that higher b_E represents the ratio of the magnitude of electromigration and diffusion kinetics, which means, that a higher b_E can also represent an electrolyte with a lower ion diffusivity. Although experiments show, that one might expect higher voltage to amplify dendrites [55], [121], in our model a strong field instead pulls ions uniformly toward the electrode, mitigating concentration gradients and feeding recessed areas. This flux suppresses local diffusion limitations and smooths growth. In a real-world scenario, the current density rises exponentially with respect to voltage, so ions are consumed far faster than transport can replace them (2.6). For our model, this would mean, that b_E and k_r should be coupled, and with increasing b_E, k_r should decrease. On our phase diagram, this would mean that moving from the bottom-right corner, to the top-left corner would be equal to increasing current density, which is the main factor dictating the dendrite growth regime. Although not accounting for the number of deposited particles, the growth time phase diagram (Figure 32) is one way of representing current density (shorter time equals higher current density). The bottom-right and top-left corners of the phase diagram correspond to mossy and dendritic growth, respectively, therefore moving from the bottom-right to the top-left corner is analogous to increasing current density. Our model therefore confirms that to delay the onset of dendritic growth with increasing current density, one would have to increase ion-transport kinetics. This aligns well with current knowledge, as additives, that aim to do exactly that are being vigorously studied [83], [133].

Lowering the bulk ion concentration (ρ_f) accelerates depletion at the electrode (Figure 33, blue/cyan), triggering sparse, fractal growth. This mirrors real cells, where dilute electrolytes exhaust cations faster and favour dendrites, whereas highly concentrated solutions delay exhaustion and suppress branching by raising the limiting current [121]. In our simulations, the higher-ρ_f run (orange) shows a steeper drop in relative concentration only because it sustained a faster deposition rate, consuming more ions overall; given equal deposition or time, it would deplete more slowly. Thus, increasing ρ_f raises Sand's capacity, permitting uniform growth up to higher coverage [134]. Phase diagrams (Figure 31) confirm that at $\rho_f = 0.1$, even low-b_E, low-k_r conditions yield denser deposits and higher d_f than at $\rho_f = 0.001$. However, once diffusion limitation inevitably sets in, dendrites form

regardless of ρ_f. In practice, boosting electrolyte concentration trades off dendrite suppression against higher viscosity and altered conductivity.

Traditional diffusion-limited aggregation models of electrodeposition often either ignored the homogeneous ion concentration field (injecting one particle at a time from infinity) or ignored the electric field (pure random walk) [135]. Our Laplace-field-enhanced, multi-particle approach merges DLA with elements of continuum transport modelling. Prior continuum models like that of Chazalviel (1990) solved Poisson's equation and diffusion in one dimension to predict dendrite conditions [14], but did not produce the actual 2D morphology. On the other hand, Monte Carlo and phase-field models have been used to simulate 2D or 3D dendrite growth with some success, but often with either an imposed concentration gradient or simplified rules for branching [37], [66]. Our model uniquely captures fractal growth, ionic diffusion/migration, and surface kinetics in one framework. The resulting phase diagrams (Figure 31) are, to our knowledge, a novel visualization of how these parameters interact.

Literature has drawn parallels between dendrite formation and phase transitions (e.g., diffusion-limited aggregation as a critical phenomenon [13]). Our results contribute to that narrative by showing a smooth yet pronounced shift in morphology metrics. Notably, our simulations suggest that there isn't a single simple threshold but rather a continuous transition; however, the extremes are so different that in practice it behaves like an on/off (either you have dendrites or you don't). This mirrors the experimental reality: there's often a "critical current density" for dendrite onset, but one can still get some irregular growth below it, just not runaway dendrites [55].

While the current model successfully reproduces many qualitative and semi-quantitative aspects of electrodeposition, it does have limitations:

- While our 2D simulations capture branching and diffusion, real electrodeposition is inherently three-dimensional, and branching patterns and space-charge zones are inherently different. Extending the Laplace solver and stochastic growth to 3D would test whether the same trends in morphology hold, and enable realistic tracking of interfacial surface-area evolution.
- We treat attachment via a fixed probability k_r, interpolating between instantaneous and delayed sticking, but omit true Butler–Volmer kinetics. A more self-consistent model would compute a local deposition rate where the overpotential (η) combines applied voltage, Laplace-field solution potential, and concentration overpotential. This would tie k_r to ion concentration and overpotential directly (at the cost of introducing activation-energy parameters that must be calibrated against experiment).
- Our present model aims to somewhat emulate the presence of SEI via k_r, but ignores nuances such as stress-driven fractures, critical in Li metal batteries. A stiff SEI can block or crack under dendrites, whereas a soft SEI deforms, altering local ion flux [22], [105]. Incorporating an advanced SEI model would capture barrier effects, crack propagation, and stress-induced branching.
- So far b_E, k_r, and ρ_f are dimensionless proxies. To predict real-cell behaviour, one must relate b_E to a Péclet number (drift vs diffusion), k_r to a Damköhler number or nondimensional exchange current, and ρ_f to a molar concentration ratio. Dimensional analysis and calibration would enable quantitative predictions of dendrite density and growth rates.

Together, these enhancements would transform our qualitative model into a predictive tool for electrodeposition in batteries.

The insights gathered from our results reinforce the concept that dendrite formation is a transport-controlled instability – when ionic transport (by diffusion/migration) cannot keep up with deposition, the system finds relief by forming high-surface-area protrusions

(dendrites) that extend into fresh electrolyte [14]. This is essentially a Mullins–Sekerka instability in electrochemical guise, where the faster growth of protrusions further depletes nearby ions and starves the growth of less protruding regions, amplifying the non-uniformity [33]. Our model demonstrates this instability in action (one branch dominating, etc.). Secondly, the results highlight strategies for mitigating dendrites: increase k_r (e.g., by using additives that encourage surface diffusion or deposition on existing surfaces) and/or increase b_E in a controlled way (which could be achieved by improving ionic conductivity or employing pulse currents – pulsing effectively gives ions time to diffuse in, raising effective b_E relative to diffusion in the off-cycle). In fact, pulse plating is known to reduce dendrite formation [65], [90]. Although we did not explicitly simulate pulsing, one can infer from our profiles that a rest period would refill the depletion zone (raising local ρ_f) and thus move conditions from diffusion-limited back toward reaction-limited intermittently.

Finally, comparing our findings to other modelling approaches: Phase-field models (e.g., Chen *et al.*, 2017) can also produce dendritic vs mossy morphologies by tuning exchange current and diffusivity [136] Those models solve continuous field equations for concentration and potential and an order parameter for the metal. They are very powerful but computationally intensive and require many parameters. Our lattice model, while coarser, captures the essentials with fewer parameters (essentially just b_E, k_r, and initial ρ_f). It provides a more intuitive picture of particle arrival and sticking.

In conclusion, the simulation results confirm that electrodeposition morphologies emerge from the competition between ion transport and surface processes. Dendritic growth arises when diffusion (and migration) cannot replenish ions fast enough at the growth interface, leading to concentration gradients and an instability favouring filamentary deposits. Conversely, when surface kinetics are the slow step or ion transport is plentiful, deposition is more uniform and compact. The Laplace-field MBDLA model introduced here is novel in its ability to capture these phenomena within a single framework, producing realistic dendrite patterns while also providing quantitative measures (fractal dimension, density, concentration profiles) that connect to theory and experiment. This modelling approach advances our understanding by offering a unified view of previously disparate descriptions – unifying DLA fractal growth theory [13] with electrochemical transport theory [14]. By comparing the simulation "phase diagram" with experimental regimes, we gain confidence in extrapolating model predictions to real systems.

4.4 Conclusion

The modelling exercise undertaken in Chapter 4 validates, and quantitatively extends the experimental findings of Chapter 3. The geometry-aware 3-D prediction scheme reproduces the preferential deposition zones observed by MRI, confirming that spatial variations in ohmic drop alone are sufficient to affect the deposit growth, something we have seen in series- and parallel-connected compartments (Chapter 3, cell configuration study).

The second model showcases the different morphologies that emerge when tuning the MBDLA simulations. Three main regimes crystallise from the parameter sweep. In the *diffusion-limited corner* (low b_E, low k_r) dendrites propagate as sparse, self-similar trees with a fractal dimension of ~1.7 and a density below 0.2, mirroring the ramified structures seen in the diffusion-limited regime of lithium deposition studies [121]. Raising the electric bias while keeping kinetics fast suppresses long, tenuous tips and converts the growth into compact shrubs; deposit density doubles and roughness initially rises because field focusing accelerates a few dominant branches. When the surface-kinetic parameter k_r is increased instead, ions tend to travel across the interface before reduction. The resulting deposits are

thick, smooth layers, fractal dimensions approaching 2. Across all regimes, the evolution of morphologies coincides with the trends observed in the literature where dendrite growth was successfully mitigated by effectively increasing surface diffusion [137], increasing ion concentration [138] or reducing overpotential [139], lending support to Hypotheses 4 and 5 that a minimal DLA-based model, once dressed with electric-field bias and finite reaction probability, can reproduce macroscale trends.

Some of the shortcomings of this model are as follows: the simulation cannot capture more complex phenomena such as SEI formation and cracking, mechanical stress evolution or electrolyte convection, as well as the 2D-lattice-associated tip sharpening. These limitations are explicit, guiding future work toward three-dimensional, chemo-mechanically coupled extensions. Nevertheless, the current models already deliver actionable insight.

By quantifying how geometry, transport and kinetics work together to dictate deposit morphology, Chapter 4 converts qualitative guidelines (“keep current low”, “make SEI uniform”) into predictive design maps. Together with the imaging benchmarks established earlier, these numerical tools form a robust platform that will offer new pathways towards high-energy rechargeable lithium-metal batteries.

Chapter 5

Conclusions

This thesis set out to get a clearer picture of how lithium metal builds up on anodes. We did that by using two tools side by side: indirect 3D MRI that lets us monitor dendrites form in real time, and two computer models, namely a quick field-enhanced 3D DLA simulation to map deposition likelihood and secondly, a more detailed 2D simulation, that is able to recreate most morphologies observed during electrodeposition. Putting these together lets us see dendrite growth as it happens and also predict how changes in design or operating conditions alter that growth. The rest of this chapter sums up what we learned, why it matters for real batteries, where the study still falls short, and promising directions for future investigation.

5.1 Experimental and Modelling Results

The core of this work is showcasing operando electrodeposition imaging using indirect-MRI. A purpose-built symmetric cell, free of magnetic materials and optimised for RF homogeneity, enabled clear imaging of dendrite formation at ~100 μm resolution. MRI showed us exactly where and when the dendrites appeared, providing 3D volume growth data. Because conventional ex-situ techniques capture structures only after cell disassembly, which often prevents further analysis, MRI fills a critical observational gap and establishes new ways for validating theories of electrodeposition.

The cell configuration study showed a dependence of dendrite behaviour on current distribution defined by cell architecture. In a parallelly-compartmentalized cell, one compartment rapidly became the dominant sink for lithium, accelerating its own growth through a positive-feedback loop. In contrast, compartments wired in series, and therefore forced to carry the same current, grew at nearly identical rates, producing uniform, planar deposits. This proves that uneven current paths, even inside one cell, can cause dendrites to grow rapidly in a single spot. In practical battery packs, where cells are often wired in parallel, this is a warning sign: if the currents aren't balanced, one cell could fail long before the overall pack shows any trouble.

MRI also allowed direct observation of what happens when the current is reversed. The experiment confirmed that after current reversal, most of the "older" dendritic structures likely become passivated by the SEI, forming the so called "dead lithium", leaving only a small amount of active material for oxidation, mainly from the very early, dense deposits. This "dead lithium" represents irreversible capacity loss and a potential safety risk if fragments migrate or short. The finding emphasises that preventing dendrite formation is more effective than trying to heal the damage once it is done. The same study also touches on the ion-transport kinetics, confirming that an established reverse concentration gradient slightly delays the onset of dendrites in the second phase of plating.

To relate these measurements with simulation, two numerical frameworks were developed. The first, a fast 3-D diffusion-bias deposition predictor, extends classic diffusion-limited aggregation by solving a steady-state Laplace equation over a voxelised replica of the MRI cell. It sacrifices electrochemical detail in favour of computational speed: each time step completes in seconds, yet the model accurately forecast where dendrites would extend between consecutive MRI scans. It shows that tuning the only model variable (electric field bias b_E), significantly effects the prediction-success rate of the model. This shows that fairly simple physics, namely migration of Li^+ under ohmic potential drop, already captures the "where" of plating in a practical scenario. As a design tool, it enables rapid iteration on separator thickness, electrode shape, or electrolyte conductivity to screen geometries before moving to costly prototyping.

The second framework, the two-dimensional multi-body DLA simulation (MBDLA), tackled the question of how deposit morphology changes with operating parameters. By tracking an ensemble of ions performing biased random walks and by tuning dimensionless controls for electric-field bias, surface sticking probability, and bulk ion concentration, the model produced a morphological phase diagram. Three regimes emerged. At low bias and slow surface diffusivity, the classic diffusion-limited regime produced sparsely branched dendrites with fractal dimension ≈ 1.7. Increasing migration bias at fixed kinetics caused tip competition and self-shielding, giving denser, bushier structures. Finally, making surface attachment harder or allowing extensive surface diffusion yielded smooth, film-like deposits with fractal dimension approaching the Euclidean limit of two. Due to the dimensionless nature of the model, these observations only qualitatively demonstrated the changes in morphologies (growth regime) when operating conditions change; It has long been known that increased current density results in an earlier onset of ion depletion and therefore dendritic growth, which the model implicitly shows [121]. The model also validates the effects of changes in electrolyte concentration, surface diffusivity and overpotential on dendrite morphology, which have all been extensively studied for dendrite-mitigation purposes.

5.2 Implications for Battery Design and Operation

The combined findings suggest some principles: first, uniform current density is crucial. Whether it is achieved via cell geometry design, pack design, intelligent charging protocols, even current distribution limit hotspots that lead to dendrite formation. Second, electrolyte conductivity and ion availability matter as much as surface chemistry. Both determine when a cell will enter the diffusion-limited regime, which occurs in a high-current, low salt concentration and poor electrolyte diffusivity case. To stay away from this regime, ample ion supply is advisable, as well as moderate current densities. Lastly, surface mobility of lithium, controlled by SEI composition, additives, or artificial interlayers, plays a decisive role in smoothing out protrusions. Additives that enhance surface diffusion should be used alongside methods to improve bulk ion transport.

From a safety standpoint, occurrence of dead lithium highlights the need for early-warning diagnostics. If affordable hardware could detect the presence of dead lithium, the battery management unit could adjust the operating conditions or retire the cell. The demonstration that MRI can visualise these processes suggests that indirect sensing methods may be calibrated against MRI benchmarks during development.

5.3 Limitations

The presented studies base on some simplifications. The MRI experiments used a symmetric lithium–lithium cell with a simple electrolyte, thereby diverging from real battery architectures. While the imaging resolution is high for a non-destructive method, it does not capture sub-micrometre whiskers or certain transient events. The fast 3D predictor model is extremely simplified, therefore has very limited use. The 2D morphology model omits mechanical stress, solvent convection, and three-dimensional crystallization angles, all of which influence real dendrites. The chosen level of simplification allowed clear identification of dominant mechanisms, as well as allowed for a broad parameter sweep. Future work can now include additional physics onto the established core.

5.4 Future Directions

Looking ahead, there are clear steps to take regarding experimental and modelling work. Experimentally, we can try to use MRI to obtain finer images faster with, so that we can study fast events and observe finer structures. Pairing MRI with other analytical tools would certainly give a fuller picture of what's changing electrically, mechanically, and chemically. It would also be interesting to try operando imaging in real cells with a lithium metal anode and a commonly used cathode.

On the modelling side, our 2D random-walk code could be expanded into three dimensions, incorporating a dynamic SEI layer, and coupling it to bulk ion transport solvers would bridge the gap between the present 2D approach and full phase-field continuum models. Another interesting avenue is the implementation of machine learning. Such systems, trained on high-fidelity model-output data could offer fast yet accurate predictors that scale to complex geometries. Integrating these predictors into battery design workflows would allow for quick feedback for the engineers. Finally, developing control algorithms that use model-based prediction to adjust charging profiles on-the-fly could keep cells away from dangerous parameter regions identified by the model.

5.5 Final Thoughts

This thesis shows that when advanced imaging is tightly coupled with thoughtfully simplified simulations, new understanding emerges that neither approach could achieve alone. Operando MRI made dendrite growth visible in four dimensions (three spatial and one temporal); rapid DLA-based mapping explained where deposits form; and stochastic morphology simulations quantified how operating parameters steer dendritic texture. Together they confirm that dendrite formation is a coupled transport–kinetics instability, sensitive to current distribution, ion supply, and surface mobility. The insights gained lead directly to design principles—uniform current paths, high conductivity electrolytes, and mobile interphases—that can be implemented in next-generation lithium metal batteries. While challenges remain, the combination of diagnostic clarity and predictive modelling presented here moves the field closer to batteries that unlock lithium metal's full energy potential without compromising safety or life. In that sense, the thesis not only answers questions posed at the outset but also provides a roadmap for the continued quest to tame dendrites and realise safer, higher-energy electrochemical storage.

This work proves that combining 3D imaging with straightforward simulations can provide new understanding that neither method could show on its own. To conclude all the work presented with one statement: electrodeposition is an extremely unpredictable,

highly complex, multi-faceted phenomenon, with a few distinct growth regimes, that are mainly determined by ion kinetics and interface reactions. While this knowledge is not new *per se*, the presented work rather showcases new ways to look at the problem. Being an intensely researched field, significant steps towards safe rechargeable lithium metal batteries have already been made, yet the road to commercialization still seems long.

References

[1] J.-M. Tarascon and M. Armand, "Issues and challenges facing rechargeable lithium batteries," *Nature*, vol. 414, no. 6861, pp. 359–367, Nov. 2001, doi: 10.1038/35104644.

[2] M. Li, J. Lu, Z. Chen, and K. Amine, "30 Years of Lithium-Ion Batteries," *Advanced Materials*, vol. 30, no. 33, Aug. 2018, doi: 10.1002/adma.201800561.

[3] L. Kong, Y. Xing, and M. G. Pecht, "In-Situ Observations of Lithium Dendrite Growth," *IEEE Access*, vol. 6, pp. 8387–8393, Feb. 2018, doi: 10.1109/ACCESS.2018.2805281.

[4] M. S. Park, S. B. Ma, D. J. Lee, D. Im, S.-G. Doo, and O. Yamamoto, "A Highly Reversible Lithium Metal Anode," *Sci Rep*, vol. 4, no. 1, p. 3815, Jan. 2014, doi: 10.1038/srep03815.

[5] C. Monroe and J. Newman, "The Impact of Elastic Deformation on Deposition Kinetics at Lithium/Polymer Interfaces," *J Electrochem Soc*, vol. 152, no. 2, p. A396, 2005, doi: 10.1149/1.1850854.

[6] S. Pal, X. Zhang, B. Babu, X. Lin, J. Wang, and A. Vlad, "Materials, electrodes and electrolytes advances for next-generation lithium-based anode-free batteries," *Oxford Open Materials Science*, vol. 2, no. 1, Feb. 2022, doi: 10.1093/oxfmat/itac005.

[7] P. Barai, K. Higa, and V. Srinivasan, "Lithium dendrite growth mechanisms in polymer electrolytes and prevention strategies," *Physical Chemistry Chemical Physics*, vol. 19, no. 31, pp. 20493–20505, Aug. 2017, doi: 10.1039/C7CP03304D.

[8] O. Pecher, J. Carretero-González, K. J. Griffith, and C. P. Grey, "Materials' Methods: NMR in Battery Research," *Chemistry of Materials*, vol. 29, no. 1, pp. 213–242, Jan. 2017, doi: 10.1021/acs.chemmater.6b03183.

[9] Q. Li *et al.*, "In-situ visualization of lithium plating in all-solid-state lithium-metal battery," *Nano Energy*, vol. 63, p. 103895, Sep. 2019, doi: 10.1016/j.nanoen.2019.103895.

[10] A. J. Ilott, M. Mohammadi, H. J. Chang, C. P. Grey, and A. Jerschow, "Real-time 3D imaging of microstructure growth in battery cells using indirect MRI," *Proc Natl Acad Sci U S A*, vol. 113, no. 39, pp. 10779–10784, Sep. 2016, doi: 10.1073/pnas.1607903113.

[11] H. J. Chang, A. J. Ilott, N. M. Trease, M. Mohammadi, A. Jerschow, and C. P. Grey, "Correlating Microstructural Lithium Metal Growth with Electrolyte Salt Depletion in Lithium Batteries Using 7Li MRI," *J Am Chem Soc*, vol. 137, no. 48, 2015, doi: 10.1021/jacs.5b09385.

[12] H. J. Chang *et al.*, "Investigating Li Microstructure Formation on Li Anodes for Lithium Batteries by in Situ 6Li/7Li NMR and SEM," *Journal of Physical Chemistry C*, vol. 119, no. 29, pp. 16443–16451, Jul. 2015, doi: 10.1021/acs.jpcc.5b03396.

[13] T. A. Witten and L. M. Sander, "Diffusion-Limited Aggregation, a Kinetic Critical Phenomenon," *Phys Rev Lett*, vol. 47, no. 19, pp. 1400–1403, Nov. 1981, doi: 10.1103/PhysRevLett.47.1400.

[14] J.-N. Chazalviel, "Electrochemical aspects of the generation of ramified metallic electrodeposits," *Phys Rev A (Coll Park)*, vol. 42, no. 12, pp. 7355–7367, Dec. 1990, doi: 10.1103/PhysRevA.42.7355.

[15] E. Peled, "The Electrochemical Behavior of Alkali and Alkaline Earth Metals in Nonaqueous Battery Systems—The Solid Electrolyte Interphase Model," *J Electrochem Soc*, vol. 126, no. 12, pp. 2047–2051, Dec. 1979, doi: 10.1149/1.2128859.

[16] C. Monroe and J. Newman, "Dendrite Growth in Lithium/Polymer Systems," *J Electrochem Soc*, vol. 150, no. 10, p. A1377, 2003, doi: 10.1149/1.1606686.

[17] S. Chandrashekar, N. M. Trease, H. J. Chang, L. S. Du, C. P. Grey, and A. Jerschow, "7Li MRI of Li batteries reveals location of microstructural lithium," *Nat Mater*, vol. 11, no. 4, 2012, doi: 10.1038/nmat3246.

[18] L. He, Q. Sun, L. Lu, and S. Adams, "Understanding and Preventing Dendrite Growth in Lithium Metal Batteries," *ACS Appl Mater Interfaces*, vol. 13, no. 29, 2021, doi: 10.1021/acsami.1c08268.

[19] J. N. Chazalviel, "Electrochemical aspects of the generation of ramified metallic electrodeposits," *Phys. Rev. A*, vol. 42, no. 12, pp. 7355–7367, 1990.

[20] D. Aurbach, "Lithium metal batteries: problems and possible solutions," *Solid State Ion*, vol. 148, no. 3–4, pp. 405–416, 2000.

[21] K. N. Wood, O. Noked, and N. P. Dasgupta, "Lithium metal anodes: toward an improved understanding of coupled morphological, electrochemical, and mechanical behavior," *ACS Energy Lett*, vol. 2, no. 3, pp. 664–672, 2017.

[22] G. Bieker, M. Winter, and P. Bieker, "Electrochemical in situ investigations of SEI and dendrite formation on the lithium metal anode," *Physical Chemistry Chemical Physics*, vol. 17, no. 14, pp. 8670–8679, 2015, doi: 10.1039/C4CP05865H.

[23] P. Barai and V. Srinivasan, "Stress induced diffuse-interface theory of Li dendrite growth," *J Electrochem Soc*, vol. 164, no. 2, pp. A180–A189, 2017.

[24] A. F. Bower, P. R. Guduru, and V. A. Sethuraman, "A finite strain model of stress, diffusion, plastic flow, and electrochemical reactions in a lithium-ion half-cell," *Journal of Mechanics and Physics of Solids*, vol. 59, no. 4, pp. 804–828, 2011.

[25] H. Yan *et al.*, "How Does the Creep Stress Regulate Void Formation at the Lithium-Solid Electrolyte Interface during Stripping?," *Adv Energy Mater*, vol. 12, no. 2, Jan. 2022, doi: 10.1002/aenm.202102283.

[26] A. J. Bard and L. R. Faulkner, *Electrochemical Methods: Fundamentals and Applications*, Second Edition. John Wiley & Sons.

[27] J. Newman and K. E. Thomas-Alyea, *Electrochemical Systems*. John Wiley & Sons, 2004.

[28] K. Oura, M. Katayama, A. V. Zotov, V. G. Lifshits, and A. A. Saranin, "Surface Science," 2003, doi: 10.1007/978-3-662-05179-5.

[29] Z. Hong and V. Viswanathan, "Prospect of Thermal Shock Induced Healing of Lithium Dendrite," *ACS Energy Lett*, vol. 4, no. 5, pp. 1012–1019, May 2019, doi: 10.1021/acsenergylett.9b00433.

[30] K. Xu, "Nonaqueous Liquid Electrolytes for Lithium-Based Rechargeable Batteries," *Chem Rev*, vol. 104, no. 10, pp. 4303–4418, Oct. 2004, doi: 10.1021/cr030203g.

[31] Z. Liu, Y. Qi, Y. X. Lin, L. Chen, P. Lu, and L. Q. Chen, "Interfacial Study on Solid Electrolyte Interphase at Li Metal Anode: Implication for Li Dendrite Growth," *J Electrochem Soc*, vol. 163, no. 3, pp. A592–A598, Jan. 2016, doi: 10.1149/2.0151605jes.

[32] X. Wang *et al.*, "Stress-driven lithium dendrite growth mechanism and dendrite mitigation by electroplating on soft substrates," *Nat Energy*, vol. 3, no. 3, pp. 227–235, Mar. 2018, doi: 10.1038/s41560-018-0104-5.

[33] W. W. Mullins and R. F. Sekerka, "Morphological Stability of a Particle Growing by Diffusion or Heat Flow," *J Appl Phys*, vol. 34, no. 2, pp. 323–329, Feb. 1963, doi: 10.1063/1.1702607.

[34] K. R. Elder, M. Grant, N. Provatas, and J. M. Kosterlitz, "Sharp interface limits of phase-field models," *Phys Rev E*, vol. 64, no. 2, p. 021604, Jul. 2001, doi: 10.1103/PhysRevE.64.021604.

[35] W. J. Boettinger, J. A. Warren, C. Beckermann, and A. Karma, "Phase-Field Simulation of Solidification," *Annu Rev Mater Res*, vol. 32, no. 1, pp. 163–194, Aug. 2002, doi: 10.1146/annurev.matsci.32.101901.155803.

[36] N. Provatas and K. Elder, *Phase-Field Methods in Materials Science and Engineering*. Wiley, 2010. doi: 10.1002/9783527631520.

[37] L.-Q. Chen, "Phase-Field Models for Microstructure Evolution," *Annu Rev Mater Res*, vol. 32, no. 1, pp. 113–140, Aug. 2002, doi: 10.1146/annurev.matsci.32.112001.132041.

[38] L. Chen *et al.*, "Modulation of dendritic patterns during electrodeposition: A nonlinear phase-field model," *J Power Sources*, vol. 300, pp. 376–385, Dec. 2015, doi: 10.1016/J.JPOWSOUR.2015.09.055.

[39] D. Marx and J. Hutter, *Ab Initio Molecular Dynamics*. Cambridge University Press, 2009. doi: 10.1017/CBO9780511609633.

[40] L. A. Selis and J. M. Seminario, "Dendrite formation in Li-metal anodes: an atomistic molecular dynamics study," *RSC Adv*, vol. 9, no. 48, pp. 27835–27848, Sep. 2019, doi: 10.1039/C9RA05067A.

[41] M. S. Daw, S. M. Foiles, and M. I. Baskes, "The embedded-atom method: a review of theory and applications," *Materials Science Reports*, vol. 9, no. 7–8, pp. 251–310, Mar. 1993, doi: 10.1016/0920-2307(93)90001-U.

[42] B. J. Lee, W. S. Ko, H. K. Kim, and E. H. Kim, "The modified embedded-atom method interatomic potentials and recent progress in atomistic simulations," *Calphad*, vol. 34, no. 4, pp. 510–522, Dec. 2010, doi: 10.1016/J.CALPHAD.2010.10.007.

[43] S. A. Tawfik, L. La, T. M. Nguyen, T. Tran, S. Gupta, and S. Venkatesh, "Scale matters: simulation of nanoscopic dendrite initiation in lithium solid electrolyte interphases using a machine learning potential," *J Mater Chem A Mater*, 2025, doi: 10.1039/D4TA08189G.

[44] L. Yu, X. Chen, N. Yao, Y. C. Gao, and Q. Zhang, "Constant-potential molecular dynamics simulation and its application in rechargeable batteries," *J Mater Chem A Mater*, vol. 11, no. 21, pp. 11078–11088, May 2023, doi: 10.1039/D3TA01411H.

[45] M. Kitta and H. Sano, "Real-Time Observation of Li Deposition on a Li Electrode with Operand Atomic Force Microscopy and Surface Mechanical Imaging," *Langmuir*, vol. 33, no. 8, pp. 1861–1866, Feb. 2017, doi: 10.1021/ACS.LANGMUIR.6B04651/ASSET/IMAGES/LARGE/LA-2016-04651Y_0006.JPEG.

[46] H. G. Lee, S. Y. Kim, and J. S. Lee, "Dynamic observation of dendrite growth on lithium metal anode during battery charging/discharging cycles," *npj Computational Materials 2022 8:1*, vol. 8, no. 1, pp. 1–13, May 2022, doi: 10.1038/s41524-022-00788-6.

[47] G. Xu, F. Hao, J. Hong, and D. Fang, "Atomic-scale simulations for lithium dendrite growth driven by strain gradient," *Applied Mathematics and Mechanics (English Edition)*, vol. 41, no. 4, pp. 533–542, Apr. 2020, doi: 10.1007/S10483-020-2596-5/METRICS.

[48] J. Jiao *et al.*, "Self-Healing Mechanism of Lithium in Lithium Metal," *Advanced Science*, vol. 9, no. 12, p. 2105574, Apr. 2022, doi: 10.1002/ADVS.202105574.

[49] K. A. Fichthorn and W. H. Weinberg, "Theoretical foundations of dynamical Monte Carlo simulations," *J Chem Phys*, vol. 95, no. 2, pp. 1090–1096, Jul. 1991, doi: 10.1063/1.461138.

[50] A. F. Voter, "Introduction to the kinetic Monte Carlo method," *Radiation Effects in Solids*, pp. 1–23, May 2007, doi: 10.1007/978-1-4020-5295-8_1.

[51] B. Chopard and M. Droz, *Cellular Automata Modeling of Physical Systems*. Cambridge University Press, 1998. doi: 10.1017/CBO9780511549755.

[52] S. Wolfram, "Universality and complexity in cellular automata," *Physica D*, vol. 10, no. 1–2, pp. 1–35, Jan. 1984, doi: 10.1016/0167-2789(84)90245-8.

[53] T. Vicsek, "Fractal Growth Phenomena," *Fractal Growth Phenomena*, Jun. 1992, doi: 10.1142/1407.

[54] M. Castro, R. Cuerno, A. Sánchez, and F. Domínguez-Adame, "Multiparticle biased diffusion-limited aggregation with surface diffusion: A comprehensive model of electrodeposition," *Phys Rev E*, vol. 62, no. 1, pp. 161–173, Jul. 2000, doi: 10.1103/PhysRevE.62.161.

[55] A. Jana, S. I. Woo, K. S. N. Vikrant, and R. E. García, "Electrochemomechanics of lithium dendrite growth," *Energy Environ Sci*, vol. 12, no. 12, pp. 3595–3607, Dec. 2019, doi: 10.1039/c9ee01864f.

[56] L. M. Sander, Z. M. Cheng, and R. Richter, "Diffusion-limited aggregation in three dimensions," *Phys Rev B*, vol. 28, no. 11, pp. 6394–6396, Dec. 1983, doi: 10.1103/PhysRevB.28.6394.

[57] R. F. Voss and M. Tomkiewicz, "Computer Simulation of Dendritic Electrodeposition," *J Electrochem Soc*, vol. 132, no. 2, pp. 371–375, Feb. 1985, doi: 10.1149/1.2113841.

[58] T. Ozbey and M. Bayirli, "A numerical study for the relationship between natural manganese dendrites and DLA patterns," *Zeitschrift fur Naturforschung - Section A Journal of Physical Sciences*, vol. 71, no. 3, pp. 225–234, 2016, doi: 10.1515/zna-2015-0406.

[59] Z. Hou *et al.*, "Three-dimensional mineral dendrites reveal a nonclassical crystallization pathway," *Geology*, vol. 51, no. 7, pp. 626–630, Jul. 2023, doi: 10.1130/G51127.1.

[60] C. Kharbachi, T. Tzedakis, and F. Chauvet, "Crossover between Re-Nucleation and Dendritic Growth in Electrodeposition without Supporting Electrolyte," *J Electrochem Soc*, vol. 168, no. 7, p. 072507, Jul. 2021, doi: 10.1149/1945-7111/AC15BB.

[61] A. Sánchez, M. J. Bernal, and J. M. Riveiro, "Multiparticle aggregation model for dendritic growth applied to experiments on amorphous Co-P alloys," *Phys Rev E*, vol. 50, no. 4, pp. R2427–R2430, Oct. 1994, doi: 10.1103/PhysRevE.50.R2427.

[62] R. Failla, M. Bologna, and B. Tellini, "Dendrite growth model in battery cell combining electrode edge effects and stochastic forces into a Diffusion Limited Aggregation scheme," *J Power Sources*, vol. 433, p. 126675, Sep. 2019, doi: 10.1016/J.JPOWSOUR.2019.05.081.

[63] J. Elezgaray, C. Léger, and F. Argoul, "Linear Stability Analysis of Unsteady Galvanostatic Electrodeposition in the Two-Dimensional Diffusion-Limited Regime," *J Electrochem Soc*, vol. 145, no. 6, pp. 2016–2024, Jun. 1998, doi: 10.1149/1.1838592/XML.

[64] G. J. Ackland and E. S. Tweedie, "Microscopic model of diffusion limited aggregation and electrodeposition in the presence of leveling molecules," *Phys Rev E Stat Nonlin Soft Matter Phys*, vol. 73, no. 1, p. 011606, Jan. 2006, doi: 10.1103/PHYSREVE.73.011606/FIGURES/4/MEDIUM.

[65] A. Aryanfar, D. Brooks, B. V. Merinov, W. A. Goddard, A. J. Colussi, and M. R. Hoffmann, "Dynamics of Lithium Dendrite Growth and Inhibition: Pulse Charging Experiments and Monte Carlo Calculations," *J Phys Chem Lett*, vol. 5, no. 10, pp. 1721–1726, May 2014, doi: 10.1021/jz500207a.

[66] T. Treeratanaphitak, M. D. Pritzker, and N. M. Abukhdeir, "Kinetic monte carlo simulation of electrodeposition using the embedded-atom method," *Electrochim Acta*, vol. 121, pp. 407–414, Mar. 2014, doi: 10.1016/j.electacta.2013.12.166.

[67] O. Okutani, H. Shitamoto, and T. Nagatani, "Monte Carlo simulation of coverage in two-dimensional thin-layer electrodeposition," *Heat Transfer - Japanese Research*, vol. 27, no. 5, pp. 365–375, 1998, doi: 10.1002/(SICI)1520-6556(1998)27:5<365::AID-HTJ4>3.0.CO;2-T.

[68] Y. Dang, J. Dai, H. Du, J. Ai, C. Zhai, and W. Sun, "A two-dimensional cellular automaton-finite difference (CA-FD) model for lithium dendrite simulation," *J Energy Storage*, vol. 98, p. 113163, Sep. 2024, doi: 10.1016/J.EST.2024.113163.

[69] P. T. Callaghan, *Principles of Nuclear Magnetic Resonance Microscopy*. New York: Oxford University Press, 1993.

[70] E. Fukushima and S. B. W. Roeder, *Experimental Pulse NMR*. CRC Press, 2018. doi: 10.1201/9780429493867.

[71] R. R. Ernst, G. Bodenhausen, and A. Wokaun, *Principles of Nuclear Magnetic Resonance in One and Two Dimensions*. Oxford University PressOxford, 1990. doi: 10.1093/oso/9780198556473.001.0001.

[72] K. F. Morris and C. S. Johnson, "Diffusion-ordered two-dimensional nuclear magnetic resonance spectroscopy," *J Am Chem Soc*, vol. 114, no. 8, pp. 3139–3141, Apr. 1992, doi: 10.1021/ja00034a071.

[73] J. H. Ardenkjær-Larsen *et al.*, "Increase in signal-to-noise ratio of > 10,000 times in liquid-state NMR," *Proceedings of the National Academy of Sciences*, vol. 100, no. 18, pp. 10158–10163, Sep. 2003, doi: 10.1073/pnas.1733835100.

[74] R. Bhattacharyya, B. Key, H. Chen, A. S. Best, A. F. Hollenkamp, and C. P. Grey, "In situ NMR observation of the formation of metallic lithium microstructures in lithium batteries," *Nat Mater*, vol. 9, no. 6, pp. 504–510, Jun. 2010, doi: 10.1038/nmat2764.

[75] A. B. Gunnarsdóttir, C. V. Amanchukwu, S. Menkin, and C. P. Grey, "Noninvasive in Situ NMR Study of 'dead Lithium' Formation and Lithium Corrosion in Full-Cell Lithium Metal Batteries," *J Am Chem Soc*, vol. 142, no. 49, 2020, doi: 10.1021/jacs.0c10258.

[76] M. A. Hope *et al.*, "Selective NMR observation of the SEI–metal interface by dynamic nuclear polarisation from lithium metal," *Nature Communications 2020 11:1*, vol. 11, no. 1, pp. 1–8, May 2020, doi: 10.1038/s41467-020-16114-x.

[77] A. K. Sethurajan *et al.*, "Incorporating Dendrite Growth into Continuum Models of Electrolytes: Insights from NMR Measurements and Inverse Modeling," *J Electrochem Soc*, vol. 166, no. 8, pp. A1591–A1602, May 2019, doi: 10.1149/2.0921908jes.

[78] S. A. Krachkovskiy, A. D. Pauric, I. C. Halalay, and G. R. Goward, "'Slice-selective NMR diffusion measurements: a robust and reliable tool for in situ characterization of ion-transport properties in lithium-ion battery electrolytes,'" *J Phys Chem Lett*, vol. 4, no. 22, p. 3940, Nov. 2013, doi: 10.1021/jz402103f.

[79] R. W. Brown, Y. N. Cheng, E. M. Haacke, M. R. Thompson, and R. Venkatesan, *Magnetic Resonance Imaging*. Wiley, 2014. doi: 10.1002/9781118633953.

[80] A. J. Ilott *et al.*, "Visualizing skin effects in conductors with MRI: 7Li MRI experiments and calculations," *Journal of Magnetic Resonance*, vol. 245, pp. 143–149, Aug. 2014, doi: 10.1016/j.jmr.2014.06.013.

[81] A. J. Ilott, M. Mohammadi, C. M. Schauerman, M. J. Ganter, and A. Jerschow, "Rechargeable lithium-ion cell state of charge and defect detection by in-situ inside-out magnetic resonance imaging," *Nature Communications 2018 9:1*, vol. 9, no. 1, pp. 1–7, May 2018, doi: 10.1038/s41467-018-04192-x.

[82] M. Mohammadi, E. V. Silletta, A. J. Ilott, and A. Jerschow, "Diagnosing current distributions in batteries with magnetic resonance imaging," *Journal of Magnetic Resonance*, vol. 309, p. 106601, Dec. 2019, doi: 10.1016/j.jmr.2019.106601.

[83] H. Zhang, G. G. Eshetu, X. Judez, C. Li, L. M. Rodriguez-Martínez, and M. Armand, "Electrolyte Additives for Lithium Metal Anodes and Rechargeable Lithium Metal Batteries: Progress and Perspectives," 2018. doi: 10.1002/anie.201712702.

[84] S. Yamazaki, R. Tatara, H. Mizuta, K. Kawano, S. Yasuno, and S. Komaba, "Consumption of Fluoroethylene Carbonate Electrolyte-Additive at the Si–Graphite Negative Electrode in Li and Li-Ion Cells," *The Journal of Physical Chemistry C*, vol. 127, no. 29, pp. 14030–14040, Jul. 2023, doi: 10.1021/acs.jpcc.3c00843.

[85] F. Ding *et al.*, "Dendrite-free lithium deposition via self-healing electrostatic shield mechanism," *J Am Chem Soc*, vol. 135, no. 11, pp. 4450–4456, Mar. 2013, doi: 10.1021/JA312241Y/SUPPL_FILE/JA312241Y_SI_006.MOV.

[86] S. Zhang, "Suppressing Li Dendrites via Electrolyte Engineering by Crown Ethers for Lithium Metal Batteries," *Nanomicro Lett*, vol. 12, no. 1, Aug. 2020, doi: 10.1007/s40820-020-00501-6.

[87] Z. Ahmad, Z. Hong, and V. Viswanathan, "Design rules for liquid crystalline electrolytes for enabling dendrite-free lithium metal batteries," *Proceedings of the National Academy of Sciences*, vol. 117, no. 43, pp. 26672–26680, Oct. 2020, doi: 10.1073/pnas.2008841117.

[88] L. Suo, Y. S. Hu, H. Li, M. Armand, and L. Chen, "A new class of Solvent-in-Salt electrolyte for high-energy rechargeable metallic lithium batteries," *Nature Communications 2013 4:1*, vol. 4, no. 1, pp. 1–9, Feb. 2013, doi: 10.1038/ncomms2513.

[89] Y. Maeyoshi, K. Yoshii, and H. Sakaebe, "Stable Lithium Metal Plating/Stripping in a Localized High-Concentration Cyclic Carbonate-Based Electrolyte," *Electrochemistry*, vol. 90, no. 4, pp. 047001–047001, Apr. 2022, doi: 10.5796/ELECTROCHEMISTRY.22-00014.

[90] M. Z. Mayers, J. W. Kaminski, and T. F. Miller, "Suppression of dendrite formation via pulse charging in rechargeable lithium metal batteries," *Journal of Physical Chemistry C*, vol. 116, no. 50, pp. 26214–26221, Dec. 2012, doi: 10.1021/jp309321w.

[91] Y. Lu, M. Tikekar, R. Mohanty, K. Hendrickson, L. Ma, and L. A. Archer, "Stable Cycling of Lithium Metal Batteries Using High Transference Number Electrolytes," *Adv Energy Mater*, vol. 5, no. 9, May 2015, doi: 10.1002/aenm.201402073.

[92] M. H. Ryou, Y. M. Lee, Y. Lee, M. Winter, and P. Bieker, "Mechanical surface modification of lithium metal: Towards improved Li metal anode performance by directed Li plating," *Adv Funct Mater*, vol. 25, no. 6, 2015, doi: 10.1002/adfm.201402953.

[93] L. Shen *et al.*, "Progress on Lithium Dendrite Suppression Strategies from the Interior to Exterior by Hierarchical Structure Designs," 2020. doi: 10.1002/smll.202000699.

[94] J. Park, J. Jeong, Y. Lee, M. Oh, M. H. Ryou, and Y. M. Lee, "Micro-Patterned Lithium Metal Anodes with Suppressed Dendrite Formation for Post Lithium-Ion Batteries," *Adv Mater Interfaces*, vol. 3, no. 11, 2016, doi: 10.1002/admi.201600140.

[95] J. Park *et al.*, "Size effects of micro-pattern on lithium metal surface on the electrochemical performance of lithium metal secondary batteries," *J Power Sources*, 2018, doi: 10.1016/j.jpowsour.2018.09.061.

[96] Y. Li, J. Jiao, J. Bi, X. Wang, Z. Wang, and L. Chen, "Controlled deposition of Li metal," *Nano Energy*, vol. 32, 2017, doi: 10.1016/j.nanoen.2016.12.030.

[97] Q. Li *et al.*, "Electro-plating and stripping behavior on lithium metal electrode with ordered three-dimensional structure," *Nano Energy*, vol. 45, pp. 463–470, Mar. 2018, doi: 10.1016/j.nanoen.2018.01.019.

[98] J. Xie *et al.*, "Engineering stable interfaces for three-dimensional lithium metal anodes," *Sci Adv*, vol. 4, no. 7, Jul. 2018, doi: 10.1126/sciadv.aat5168.

[99] Y. Liu, D. Lin, Z. Liang, J. Zhao, K. Yan, and Y. Cui, "Lithium-coated polymeric matrix as a minimum volume-change and dendrite-free lithium metal anode," *Nat Commun*, vol. 7, Mar. 2016, doi: 10.1038/NCOMMS10992.

[100] Q. Zhao, S. Stalin, and L. A. Archer, "Stabilizing metal battery anodes through the design of solid electrolyte interphases," *Joule*, vol. 5, no. 5, pp. 1119–1142, May 2021, doi: 10.1016/j.joule.2021.03.024.

[101] Y. Zhu *et al.*, "Design principles for self-forming interfaces enabling stable lithium-metal anodes," *Proc Natl Acad Sci U S A*, vol. 117, no. 44, pp. 27195–27203, Nov. 2020, doi: 10.1073/PNAS.2001923117/SUPPL_FILE/PNAS.2001923117.SD01.XLSX.

[102] X. B. Cheng and Q. Zhang, "Dendrite-free lithium metal anodes: stable solid electrolyte interphases for high-efficiency batteries," *J Mater Chem A Mater*, vol. 3, no. 14, pp. 7207–7209, Mar. 2015, doi: 10.1039/C5TA00689A.

[103] Z. Ju *et al.*, "A self-healing Li-crosslinked elastomer promotes a highly robust and conductive solid–electrolyte interphase," *Energy Environ Sci*, vol. 17, no. 13, pp. 4703–4713, Jul. 2024, doi: 10.1039/D4EE01359J.

[104] Y. Sun, J. Li, S. Xu, H. Zhou, and S. Guo, "Molecular Engineering toward Robust Solid Electrolyte Interphase for Lithium Metal Batteries," *Advanced Materials*, vol. 36, no. 14, p. 2311687, Apr. 2024, doi: 10.1002/ADMA.202311687.

[105] W. Liu, P. Liu, and D. Mitlin, "Review of Emerging Concepts in SEI Analysis and Artificial SEI Membranes for Lithium, Sodium, and Potassium Metal Battery Anodes," *Adv Energy Mater*, vol. 10, no. 43, p. 2002297, Nov. 2020, doi: 10.1002/AENM.202002297.

[106] A. Ramasubramanian, V. Yurkiv, T. Foroozan, M. Ragone, R. Shahbazian-Yassar, and F. Mashayek, "Stability of solid-electrolyte interphase (SEI) on the lithium metal surface in lithium metal batteries (LMBs)," *ACS Appl Energy Mater*, vol. 3, no. 11, pp. 10560–10567, Nov. 2020, doi: 10.1021/acsaem.0c01605.

[107] Y. Ma *et al.*, "Reversing the dendrite growth direction and eliminating the concentration polarization via an internal electric field for stable lithium metal anodes," *Chem Sci*, vol. 13, no. 32, 2022, doi: 10.1039/d2sc03313e.

[108] X. Zhang *et al.*, "Rethinking How External Pressure Can Suppress Dendrites in Lithium Metal Batteries," *J Electrochem Soc*, vol. 166, no. 15, pp. A3639–A3652, 2019, doi: 10.1149/2.0701914jes.

[109] Z. Hao *et al.*, "Functional separators towards the suppression of lithium dendrites for rechargeable high-energy batteries," *Mater Horiz*, vol. 8, no. 1, pp. 12–32, Jan. 2021, doi: 10.1039/D0MH01167C.

[110] Y. Gao *et al.*, "Regulating electrodeposition behavior through enhanced mass transfer for stable lithium metal anodes," *Journal of Energy Chemistry*, vol. 55, pp. 580–587, Apr. 2021, doi: 10.1016/J.JECHEM.2020.07.019.

[111] I. Serša and U. Mikac, "A study of MR signal reception from a model for a battery cell," *Journal of Magnetic Resonance*, vol. 294, pp. 7–15, Sep. 2018, doi: 10.1016/j.jmr.2018.06.013.

[112] M. M. Britton, "Magnetic Resonance Imaging of Electrochemical Cells Containing Bulk Metal," *ChemPhysChem*, vol. 15, no. 9, pp. 1731–1736, Jun. 2014, doi: 10.1002/cphc.201400083.

[113] G. B. Chavhan, P. S. Babyn, B. Thomas, M. M. Shroff, and E. Mark Haacke, "Principles, techniques, and applications of T2*-based MR imaging and its special applications," *Radiographics*, vol. 29, no. 5, pp. 1433–1449, Sep. 2009, doi: 10.1148/RG.295095034,.

[114] G. W. Richardson, J. M. Foster, R. Ranom, C. P. Please, and A. M. Ramos, "Charge transport modelling of Lithium-ion batteries," *Eur J Appl Math*, vol. 33, no. 6, pp. 983–1031, 2022, doi: 10.1017/S0956792521000292.

[115] M. Titirici, P. Johansson, M. Crespo Ribadeneyra, al -, S. Drvari Talian, and J. Moškon, "Highly Sensitive Operando Pressure Measurements of Li-ion Battery Materials with a Simply Modified Swagelok Cell," *J Electrochem Soc*, vol. 167, no. 11, p. 110511, Jul. 2020, doi: 10.1149/1945-7111/AB9E81.

[116] S. Ko *et al.*, "Rapid safety screening realized by accelerating rate calorimetry with lab-scale small batteries," *Nature Energy 2025*, pp. 1–8, Apr. 2025, doi: 10.1038/s41560-025-01751-7.

[117] S. Baazouzi, N. Feistel, J. Wanner, I. Landwehr, A. Fill, and K. P. Birke, "Design, Properties, and Manufacturing of Cylindrical Li-Ion Battery Cells—A Generic Overview," *Batteries 2023, Vol. 9, Page 309*, vol. 9, no. 6, p. 309, Jun. 2023, doi: 10.3390/BATTERIES9060309.

[118] F. Mugele and J. Heikenfeld, "Principles of Modern Electrowetting," *Electrowetting*, pp. 133–157, Feb. 2018, doi: 10.1002/9783527412396.CH5.

[119] Z. Liu, B. Huang, C. Li, H. Zhu, and G. Liu, "Review of Progress in the Application of Polytetrafluoroethylene-Based Battery Separators," *ACS Appl Mater Interfaces*, vol. 16, p. 63128, Nov. 2024, doi: 10.1021/ACSAMI.4C12380.

[120] X. Wen *et al.*, "A hydrophobic membrane to enable lithium-air batteries to operate in ambient air with a long cycle life," *Electrochim Acta*, vol. 421, p. 140517, Jul. 2022, doi: 10.1016/J.ELECTACTA.2022.140517.

[121] P. Bai, J. Li, F. R. Brushett, and M. Z. Bazant, "Transition of lithium growth mechanisms in liquid electrolytes," *Energy Environ Sci*, vol. 9, no. 10, pp. 3221–3229, Oct. 2016, doi: 10.1039/c6ee01674j.

[122] T. Foroozan, S. Sharifi-Asl, and R. Shahbazian-Yassar, "Mechanistic understanding of Li dendrites growth by in- situ/operando imaging techniques," *J Power Sources*, vol. 461, 2020, doi: 10.1016/j.jpowsour.2020.228135.

[123] M. Pigłowska *et al.*, "Challenges for Safe Electrolytes Applied in Lithium-Ion Cells—A Review," *Materials*, vol. 14, no. 22, p. 6783, Nov. 2021, doi: 10.3390/ma14226783.

[124] Y. P. Yang *et al.*, "Thermal stability analysis of lithium-ion battery electrolytes based on lithium bis(Trifluoromethanesulfonyl)imide-lithium difluoro(oxalato)borate dual-salt," *Polymers (Basel)*, vol. 13, no. 5, 2021, doi: 10.3390/polym13050707.

[125] W. Dachraoui, R.-S. Kühnel, Dr. C. Battaglia, and R. Erni, "Nucleation, Growth and Dissolution of Li Metal Dendrites and the Formation of Dead Li in Li-Ion Batteries Investigated by Operando Electrochemical Liquid Cell Scanning Transmission Electron Microscopy," 2024, doi: 10.2139/SSRN.4866676.

[126] Y. S. Cohen, Y. Cohen, and D. Aurbach, "Micromorphological Studies of Lithium Electrodes in Alkyl Carbonate Solutions Using in Situ Atomic Force Microscopy," *Journal of Physical Chemistry B*, vol. 104, no. 51, pp. 12282–12291, Dec. 2000, doi: 10.1021/JP002526B.

[127] K. N. Wood *et al.*, "Dendrites and pits: Untangling the complex behavior of lithium metal anodes through operando video microscopy," *ACS Cent Sci*, vol. 2, no. 11, pp. 790–801, Nov. 2016, doi: 10.1021/ACSCENTSCI.6B00260/SUPPL_FILE/OC6B00260_SI_001.MOV.

[128] W. Zhang *et al.*, "Recovery of isolated lithium through discharged state calendar ageing," *Nature 2024 626:7998*, vol. 626, no. 7998, pp. 306–312, Feb. 2024, doi: 10.1038/s41586-023-06992-8.

[129] D. Aurbach, "Review of selected electrode–solution interactions which determine the performance of Li and Li ion batteries," *J Power Sources*, vol. 89, no. 2, pp. 206–218, Aug. 2000, doi: 10.1016/S0378-7753(00)00431-6.

[130] T. A. Witten and L. M. Sander, "Diffusion-limited aggregation," *Phys Rev B*, vol. 27, no. 9, pp. 5686–5697, May 1983, doi: 10.1103/PhysRevB.27.5686.

[131] M. Jäckle and A. Groß, "Microscopic properties of lithium, sodium, and magnesium battery anode materials related to possible dendrite growth," *Journal of Chemical Physics*, vol. 141, no. 17, Nov. 2014, doi: 10.1063/1.4901055/313588.

[132] M. Matsushita, M. Sano, Y. Hayakawa, H. Honjo, and Y. Sawada, "Fractal Structures of Zinc Metal Leaves Grown by Electrodeposition," *Phys Rev Lett*, vol. 53, no. 3, p. 286, Jul. 1984, doi: 10.1103/PhysRevLett.53.286.

[133] S. S. Zhang, "A review on electrolyte additives for lithium-ion batteries," *J Power Sources*, vol. 162, no. 2, pp. 1379–1394, Nov. 2006, doi: 10.1016/j.jpowsour.2006.07.074.

[134] Z. Li, J. Huang, B. Yann Liaw, V. Metzler, and J. Zhang, "A review of lithium deposition in lithium-ion and lithium metal secondary batteries," *J Power Sources*, vol. 254, pp. 168–182, May 2014, doi: 10.1016/j.jpowsour.2013.12.099.

[135] T. C. Halsey and M. Leibig, "Electrodeposition and diffusion-limited aggregation," *J Chem Phys*, vol. 92, no. 6, pp. 3756–3767, 1990, doi: 10.1063/1.457834.

[136] C. H. Chen and C. W. Pao, "Phase-field study of dendritic morphology in lithium metal batteries," *J Power Sources*, vol. 484, p. 229203, Feb. 2021, doi: 10.1016/J.JPOWSOUR.2020.229203.

[137] A. A. Rulev, Y. O. Kondratyeva, L. V. Yashina, and D. M. Itkis, "Lithium Planar Deposition vs Whisker Growth: Crucial Role of Surface Diffusion," *Journal of Physical Chemistry Letters*, vol. 11, no. 24, pp. 10511–10518, Dec. 2020, doi: 10.1021/ACS.JPCLETT.0C02674/SUPPL_FILE/JZ0C02674_SI_002.MP4.

[138] S. K. Jeong *et al.*, "Suppression of dendritic lithium formation by using concentrated electrolyte solutions," *Electrochem commun*, vol. 10, no. 4, pp. 635–638, Apr. 2008, doi: 10.1016/J.ELECOM.2008.02.006.

[139] Z. Yang, Q. Ruan, Y. Xiong, and X. Gu, "Highly Stable Lithium Metal Anode Constructed by Three-Dimensional Lithiophilic Materials," *Batteries 2023, Vol. 9, Page 30*, vol. 9, no. 1, p. 30, Dec. 2022, doi: 10.3390/BATTERIES9010030.

Bibliography

Publications Related to the Thesis

Journal Articles

R. Peklar, U. Mikac, and I. Serša, 'The effect of battery configuration on dendritic growth: A magnetic resonance microscopy study on symmetric lithium cells', *Batteries*, vol. 10, no. 165, pp. 13, 2024.

R. Peklar, U. Mikac, in I. Serša, 'Simulation of dendrite growth with a diffusion-limited aggregation model validated by MRI of a lithium symmetric cell during charging', *Batteries*, vol. 10, no. 10, pp. 1–15, 2024.

R. Peklar, U. Mikac, in I. Serša, 'Observation of Electroplating in a Lithium-Metal Battery Model Using Magnetic Resonance Microscopy', *Molecules*, vol. 30, no. 13, pp. 2733, 2025.

Biography

The author of this thesis completed both his Bachelor's and Master's degrees in Physics at the Faculty of Natural Sciences and Mathematics (FNM), University of Maribor. His Master's thesis, titled *"Numerical Analysis of Exhaust Gas Flow and Thermal Analysis of an Exhaust Manifold,"* focused on computational fluid dynamics (CFD) modelling and finite volume analysis. He completed his Master's degree under the supervision of Doc. Dr. Milan Ambrožič, with Mag. Andrej Poredoš serving as co-supervisor.

In 2019, he began his doctoral studies at the Jožef Stefan International Postgraduate School (IPS), in the Nanosciences and Nanotechnologies programme. His research was conducted at the Department of Condensed Matter Physics (F5) at the Jožef Stefan Institute. The doctoral thesis, titled "Investigating Dendritic Growth in Symmetrical Lithium Cells through MRI and Simulation," explores the mechanisms of dendritic lithium growth using magnetic resonance imaging (MRI) and computational modelling techniques.

During his PhD, he received training in magnetic imaging and microscopy techniques, with a particular focus on non-invasive operando characterization of electrochemical systems. He presented his research at international conferences, including the 17th ICMRM in Singapore and multiple editions of the AMPERE NMR Workshop.